

Pattern Formation by Lateral Inhibition in  
Physiological and Tumour Angiogenesis

Holly Smith MMath

April 4, 2020

# Acknowledgements

I want to thank the University of Nottingham and the School of Mathematical Sciences for supporting my research, and I want to thank my viva examiners Reuben O’Dea and Nick Monk for making my viva a pleasant experience with many interesting discussions.

I would like to thank my supervisors: Paul Matthews, for your patience, expertise, and for helping me through the tough months; Kris Van der Zee, for your help with the numerical computation and for going out to lunch with me and the other PhD students for a much needed break; and Markus Owen, for your support with the mathematical biology and for always keeping me up-to-date on the latest research. I was very lucky to have three dedicated, knowledgeable, and supportive supervisors who each helped me greatly, and all I can do to repay you is to say thank you!

I want to thank my friends for always being there for me for whatever I needed. I want to thank my whole family, especially my amazing parents Maggie and Nigel whose unwavering support for everything I choose to do in my life gave me motivation and has always made me want to make them proud. Finally, thank you to my partner Stuart, who supported and encouraged me through everything, and without whom I wouldn’t have achieved this.

# Abstract

The sprouting of new blood vessels from existing blood vessels, called angiogenesis, plays a vital role in many biological processes, including tumour growth. Angiogenesis is initiated by angiogenic signals sent to the endothelial cells of an existing blood vessel. However, to prevent migration of all the cells along the blood vessel wall, a type of cell signalling called Notch signalling causes so-called lateral inhibition between neighbouring cells, where cells activated for migration inhibit their neighbour cells from adopting the same fate. Lateral inhibition has been represented in previous models of angiogenesis using discrete agents, which have limitations such as presuming a fixed cell size for all endothelial cells and forcing selected cells to migrate immediately.

This thesis aims to develop a continuous model of lateral inhibition that is not limited with respect to cell sizes and locations, and to couple this new continuous model to a model of angiogenesis. This is achieved by developing continuous models of lateral inhibition from existing discrete models, where the lateral inhibition is represented with a nonlocal term. The continuous model can be thought of as an average representation of variables from an irregular distribution of cells. The results of the model were comparable to those of the previous discrete models. The model is then extended to a surface to allow the model to be able to simulate the cell signalling along a capillary surface.

The surface continuous model of lateral inhibition is then combined with a model of angiogenesis to obtain an almost fully continuous coupled lateral inhibition-angiogenesis model. Numerical simulations show results which closely resemble blood vessel formation in angiogenesis, where cell migration is not forced. Results are presented that are relevant to both physiological and tumour angiogenesis. The coupled model could be used in the future to investigate further implications of angiogenesis, such as the effect it has on tumour growth and tumour drug delivery, and even the effect of antiangiogenic therapies on the growth of a tumour.

# Contents

<b>Abbreviations and notation</b>	<b>8</b>
<b>1 Introduction</b>	<b>10</b>
<b>2 Biological background</b>	<b>14</b>
2.1 Introduction . . . . .	14
2.2 Cancer and therapies . . . . .	15
2.3 The Six Hallmarks of Cancer . . . . .	18
2.4 Angiogenesis . . . . .	24
2.5 Conclusion . . . . .	29
<b>3 History of mathematical models</b>	<b>31</b>
3.1 Introduction . . . . .	31
3.2 Cell signalling models . . . . .	32
3.3 Models of Angiogenesis . . . . .	33
3.3.1 Current methods of tip cell selection . . . . .	34
3.3.2 Differences between discrete and continuous models . . . . .	35
3.4 Phase field modelling . . . . .	38
3.5 Mathematical modelling of cancer . . . . .	41
3.5.1 Early models of carcinogenesis and avascular tumour growth	42

3.5.2	Models of vascular tumour growth: introducing a blood supply . . . . .	45
3.5.3	Discoveries of tumour growth models . . . . .	46
3.6	Conclusion . . . . .	48
<b>4</b>	<b>A model of lateral inhibition</b>	<b>50</b>
4.1	Introduction . . . . .	50
4.2	Continuous modelling of a discrete mechanism . . . . .	53
4.3	A Delta-Notch model . . . . .	55
4.3.1	An existing discrete model . . . . .	55
4.3.2	The average neighbour function . . . . .	56
4.4	Implementation of the continuous version of the model and stability analysis . . . . .	69
4.5	Simulation of the lateral inhibition model . . . . .	73
4.6	Conclusion . . . . .	82
<b>5</b>	<b>An extended model of lateral inhibition</b>	<b>87</b>
5.1	Introduction . . . . .	87
5.2	The extended model . . . . .	88
5.2.1	Nondimensionalisation . . . . .	90
5.2.2	Reduction of the extended model to the first model . . . . .	91
5.3	Stability analysis . . . . .	93
5.3.1	Solutions stable to homogeneous spatial perturbations . . . . .	95
5.3.2	Solutions unstable to inhomogeneous spatial perturbations . . . . .	96
5.3.3	Bifurcation analysis . . . . .	102
5.4	Simulation of the extended lateral inhibition model . . . . .	103
5.4.1	Parameter values . . . . .	103
5.4.2	Numerical Simulation . . . . .	105

5.5	Conclusion . . . . .	111
<b>6</b>	<b>Modelling lateral inhibition on a surface</b>	<b>116</b>
6.1	Introduction . . . . .	116
6.2	Phase field modelling . . . . .	118
6.3	The phase field approximation method . . . . .	119
6.3.1	Reaction-diffusion equations . . . . .	120
6.3.2	The lateral inhibition model . . . . .	126
6.4	Simulation of the surface lateral inhibition model . . . . .	130
6.4.1	Results with a stationary interface . . . . .	131
6.4.2	Results with a moving interface . . . . .	133
6.5	Conclusion . . . . .	134
<b>7</b>	<b>A phase field model of angiogenesis</b>	<b>137</b>
7.1	Introduction . . . . .	137
7.2	Derivation of the Allen-Cahn and Cahn-Hilliard models . . . . .	138
7.2.1	The Allen-Cahn Equation . . . . .	141
7.2.2	The Cahn-Hilliard Equation . . . . .	141
7.3	A phase field model for angiogenesis . . . . .	142
7.3.1	The discrete component . . . . .	144
7.3.2	Biological interpretation of the phase field model . . . . .	149
7.4	Simulation of the angiogenesis model . . . . .	153
7.4.1	Convex splitting . . . . .	153
7.4.2	Results . . . . .	156
7.5	Conclusion . . . . .	164
<b>8</b>	<b>A coupled lateral inhibition-angiogenesis model</b>	<b>168</b>
8.1	Introduction . . . . .	168

8.2	The lateral inhibition driven angiogenesis model . . . . .	170
8.2.1	The angiogenesis equations . . . . .	170
8.2.2	The DLL4-Notch equations . . . . .	172
8.3	Simulating the coupled model . . . . .	173
8.3.1	Parameter values . . . . .	175
8.3.2	Results . . . . .	176
8.4	Conclusion . . . . .	183
<b>9</b>	<b>Conclusion</b>	<b>187</b>
9.1	Potential for Future Work . . . . .	194
9.1.1	Application to a tumour growth model . . . . .	196
9.2	Final thoughts . . . . .	198
	<b>Appendix</b>	<b>199</b>
	<b>Bibliography</b>	<b>202</b>

# Abbreviations

DLL4	Delta-Like Ligand 4
EC	Endothelial Cell
ECM	Extra-Cellular Matrix
EGF-R	Epidermal Growth Factor Receptor
HC	Hypoxic Cell
$\mu m$	Micrometres
PDE	Partial Differential Equation
SEC	Stalk Endothelial Cell
TAF	Tumour Angiogenesis Factor
TEC	Tip Endothelial Cell
TGF $\alpha$	Tumour Growth Factor $\alpha$
VEGF	Vascular Endothelial Growth Factor
VEGF-R	Vascular Endothelial Growth Factor Receptor

# Notation

The derivatives used in this thesis are sometimes denoted as

$$\frac{\partial f}{\partial x} = \partial_x f.$$

For ease a model from a paper by several researchers will sometimes be referred to as the first author's model. For example, a model by Jones et al. may sometimes be referred to as Jones' model, or the Jones model.

# Chapter 1

## Introduction

The biological process known as angiogenesis has a vital role in many living beings. Angiogenesis is the growth of new blood vessels from an existing vessel. This occurs when delivery of oxygen or some other nutrient is required in areas where such nutrient levels are low. It is needed during wound healing in particular, where the cells need higher amounts of nutrient than average while mending the wound [50]. It is also prominent in cancerous, or “malignant” tumours, where the tumour tissue needs access to nutrient to continue growing and become invasive [63].

An important stage of angiogenesis is the selection of the locations along the original blood vessel where the new blood vessels will emerge from. This is achieved through cell signalling between the endothelial cells of the blood vessels, where cells activated for new blood vessel formation inhibit nearby cells from also activating. This is called lateral inhibition and is controlled in angiogenesis by a signalling mechanism known as the Notch signalling pathway [84].

Previous mathematical models of angiogenesis have limitations in their representation of lateral inhibition, which is currently implemented using restrictive assumptions. Such models are hybrid models and simulate lateral inhibition by setting an inhibited radius around any activated cells using a discrete part in the model, but the main dynamics of the model are dictated by continuous equations (see [139, 1]). This causes the model to need to define the locations and layout of the cells, and it can also make the simulation more time-consuming than a fully continuous model [143].

The aim of this work is to create a mathematical model of cell signalling that can be easily coupled with a model for angiogenesis, and to show the benefits of this new cell signalling representation. The thesis will hopefully motivate further research in this area where this new idea of cell signalling can be used for not only extensions to an angiogenesis model but also to model other process which involve similar cell signalling. The aim is supported by the following thesis objectives:

1. To develop a continuous model for lateral inhibition cell signalling by redefining the way the lateral inhibition is implemented in existing cell signalling models
2. To extend the continuous lateral inhibition model to include extra biological features
3. To simulate the cell signalling model on a surface using a surface approximation method
4. To study a hybrid model for angiogenesis that uses discrete cell signalling components

5. To successfully couple the continuous cell signalling model to the angiogenesis model and use the coupled model to simulate the activation of angiogenesis in both healthy conditions and cases where a tumour is present.

The thesis will first detail the biological background of this research. Chapter 2 will discuss the destructive nature of cancer and the hallmarks cancerous tumours have, including angiogenesis. The stages of angiogenesis will then be discussed, in particular the initiation stage when the lateral inhibition signalling occurs.

Chapter 3 gives a literature review of mathematical models related to this work, which includes cell signalling models and angiogenesis models. It also discusses the relatively new technique of phase field modelling which is a type of model that shall be implemented in this work. This chapter also comments on the different models of tumour growth that currently exist.

After examining the existing mathematical models, the mathematical content of this work will commence. The first stage is to develop a mathematical model on the cell signalling that determines new capillary locations. Chapter 4 defines a continuous variant of a cell-signalling model by Collier et al. [45] and presents simulations of this new model. This chapter discusses the differences between the discrete model and the continuous version. Chapter 5 introduces another continuous model of cell signalling based on an extension of the Collier model by Owen and Sherratt [117].

As the cell signalling in angiogenesis only occurs in the endothelial tissue in the blood vessel wall, the Delta-Notch model will need to be defined only

on the interface between the endothelial tissue and extracellular matrix before being coupled to an angiogenesis model, and therefore will need to be solved on a surface. This shall be accomplished in Chapter 6, using an approximation method which defines a function that only exists on this interface. The capability of the surface model shall be tested on stationary and moving surfaces.

A continuous model of angiogenesis by Travasso [139] will be introduced in Chapter 7 and then coupled to the surface lateral inhibition model in Chapter 8. The angiogenesis model will make use of the phase field theory mentioned earlier. A comparison between physiological and pathological angiogenesis will also be given through simulations of the angiogenesis models.

Chapter 9 will then conclude the thesis with a summary of this work and the research carried out, and will also include a discussion on the potential for future research in this area, such as the application of the coupled angiogenesis model to a tumour growth model. The benefits of the introduction of the continuous cell signalling model are given, but the disadvantages are also acknowledged, and further improvements to the model which were not covered in this work are suggested.

# Chapter 2

## Biological background

### 2.1 Introduction

Cancer is a disease that every person at sometime in their life will be affected by, either by being diagnosed themselves or by knowing someone who has been diagnosed. There are many types of cancer which develop and behave differently, and depending on the type and the stage at diagnosis, it is often fatal. The unpredictability and high mortality rates of particular types has motivated a great deal of research by both biologists and mathematicians trying to understand what cancer is and how to cure it. Despite this, cancer is still poorly understood to this day, and treatment for it has varying results [121].

Cancer does not usually emerge suddenly, as much as it appears to; it develops over time in stages due to its acquiring of so-called Hallmarks of Cancer, as stated by Hanahan and Weinberg [80]. One stage of tumour growth vital to its development into cancer is angiogenesis, during which the tumour promotes the growth of new blood vessels from pre-existing vessels to acquire

its own vascular network and therefore its own nutrient source. Angiogenesis itself has multiple stages, each of which act differently in physiological and pathological angiogenesis. A tumour vascular network is often uncontrolled and poorly functioning as a result of overexpression of some growth factors and underexpression of other proteins [24].

This chapter starts by examining cancer and what is currently known in more detail; mainly how and why a tumour develops and describing existing treatments for cancer. This is discussed in Section 2.2, and then the hallmarks of cancer are outlined in Section 2.3. An explanation of each stage of angiogenesis is given in Section 2.4, with particular focus on the onset stage of angiogenesis, which is when the Notch cell signalling takes place. The chapter is concluded in Section 2.5. By the end of this chapter there will be a general understanding of angiogenesis and the role it plays in cancer development.

## 2.2 Cancer and therapies

Cancer develops when normal cells are somehow able to multiply out of control. The body is unable to regulate this multiplication and the cells manage to invade local healthy tissue. As discussed by Hanahan and Weinberg [80] and later in Section 2.3, for such abnormal and uncontrollable behaviour to arise a mutation must occur in the cells that allows them to overcome certain regulatory conditions that normal cells obey. Normally, cells grow and form new cells when needed. When a cell becomes damaged it is either repaired by certain mechanisms or signalled to die if the damage is beyond repair. However, if a damaged cell is able to multiply before these repairing mechanisms reach it, the damage remains and these mutated cells may form growths, bet-

ter known as tumours.

The way these cancer cells form is through a genetic mutation which affects the functioning of certain cellular processes. As the definition of cancer is so vague, there are many ways it can develop. It can prevail over time as a result of a combination of faults as cells divide, or it can be caused by exposure to carcinogens, such as ultraviolet (UV) rays and tobacco smoke [156, 157]. The variation of the mutations in cancer cells means it can be more relevant to group types of cancer based on mutation type instead of location of the cancer in the body. For example, breast cancer is a type of carcinoma which is a common mutation in epithelial cells [53].

Therapy for cancer varies depending on the type, stage, and location. According to Pratt et al. [121], the three most commonly used therapies are chemotherapy, radiotherapy and surgery. Chemotherapy is the use of drugs to treat cancerous cells. Many chemotherapy drugs are inhibitory factors and stop cells from proliferating. The drawback to this is that the drug is often not cancer cell specific and affects the patient's healthy cells as well. This results in many side effects, particularly those linked to growth suppression, such as nausea, hair loss, higher risk of infection, and anaemia. However, chemotherapy may still be the best course of action if the cancer has spread to multiple areas of the body.

A relatively new category of chemotherapy is called targeted therapy, where proteins that are present in cancer cells or which play a vital part in cancer development are targeted by the drug. For example, one of the first targeted drugs was Trastuzumab, which targeted the Human Epidermal growth fac-

tor Receptor 2 (HER2) protein responsible for tumour growth in some breast cancers [146]. Other therapies have targeted the capillary growth activator Vascular Endothelial Growth Factor (VEGF), thus inhibiting angiogenesis [57].

Radiotherapy uses high-energy waves to destroy cancer cells. There is external radiotherapy which aims radiation beams, normally x-rays, directly at the tumour, and internal radiotherapy, which can take the form of a radioactive liquid or implant [127]. Radiotherapy is used if the cancer is located in one area of the body, or for killing any remaining cancer cells after chemotherapy or surgery. Surgery is also best when the cancer is in one area and has not spread far, as treatment involves attempted removal of a solid tumour. The surgeon will remove the tumour and normal cells around it to attempt to remove all cancer cells. Often a Computed Tomography (CT) or Magnetic Resonance Imaging (MRI) scan will determine the likely tumour boundary pre-surgery, along with the vascular network of blood vessels of the tumour. Sometimes surgery is used to only temporarily prolong life and, as stated by Eyüpoglu et al. during their research of the highly invasive brain tumour Glioblastoma Multiforme, should be used alongside another treatment [59].

As explained by Bednarz et al. [13] and depicted in Figure 2.1, there are other changes in cell proliferation which are not cancerous as they do not invade healthy tissue. Some of these changes are not even abnormal, such as when a high number of healthy cells appear in the event of an injury. However, other changes are abnormal and can develop into cancer if not treated. Carcinoma in-situ in particular is often classified as a cancer due to the amount of damaged cell proliferation, but it is technically not, as these damaged cells

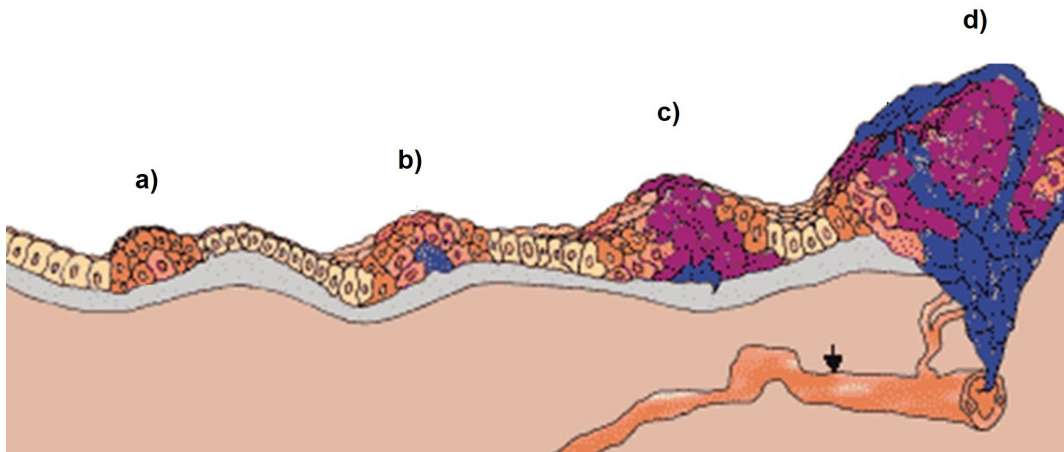


**Figure 2.1:** Different types of changes in cells. (a) Hyperplasia, occurs when cells within a tissue proliferate faster than normal, (b) Dysplasia, a pathological buildup of mutated cells where the tissue structure may change, such as in a mole, (c) Carcinoma in-situ, a developed case of dysplasia, often called cancer despite the lack of spread to normal tissue, often solved through surgical removal, (d) Cancer, where the cells have started to invade the nearby healthy tissue. Picture from Bednarz et al. [13].

have not invaded healthy tissue.

## 2.3 The Six Hallmarks of Cancer

Cancer cells have the ability to proliferate uncontrollably and invade normal cells, which are more restricted and obey physiological control signals. Cancer cells are unlike normal cells in that they no longer obey any specific function and are able to continue to multiply endlessly. There has been a large amount of research into how exactly cancer cells are able to do this. Given the previously mentioned changes in cell behaviour which are not cancerous, there has also been much debate on how to define cancer. It has been a mystery for some time and many experiments have attempted to demystify cancer (see [66, 21]).

A paper which is now widely used to define cancer was published in 2000 by Douglas Hanahan and Robert A. Weinberg, and was called “The Hallmarks of Cancer” [80]. Six hallmarks of cancer were suggested in this paper; that is, characteristics believed to be found in all cancers, where the presence of all six confirms the presence of cancer. This groundbreaking paper suggested that preventing any one of these hallmarks from emerging would prevent a tumour from developing into cancer. There was some debate as to whether more hallmarks should be considered, and an update was published by the authors of the original paper in 2011 [81], detailing the developments made in cancer research since 2000. The hallmarks from the original paper are now described.

### **Self production of growth signals**

One ability of cancer that makes it so dangerous is that the cells become self-sufficient; after a while they no longer rely on the host to grow. The production of their own growth signals is one of the ways in which these tumour cells become self-sufficient.

Normal cells require external growth factors in order to enter a mitogenic (proliferative) state, because normal cells release growth factors that activate cells of a different type, which is called heterotypic signalling. Cancer cells are able to copy their own growth factors and signal themselves, also called autocrine signalling, causing a positive signalling loop. Examples of growth factors created by cells in this way are Tumour Growth Factor  $\alpha$  (TGF $\alpha$ ) [41] and Platelet-Derived Growth Factor (PDGF) [91]. Alternatively cancer cells will sometimes signal normal cells to release their growth factors; epithelial cell growth factors released from fibroblasts have been found by both

Bhowmick et al. [20] and Cheng et al. [42] to play more of an active role in tumour growth than previously thought. The growth factor receptors in cancer cells are often overexpressed, allowing much more growth signalling than allowed in normal cells. All of these characteristics contribute to uncontrolled proliferation of tumour cells.

### **Evasion of growth suppressors**

Once the need for growth signals is met, the tumour cells must then avoid growth suppressors that are activated when too much proliferation has occurred. A normal cell will only proliferate when it is signalled by growth promoters, but also when it is not signalled by growth suppressors. Cancer cells are able to avoid this suppressive signalling to free themselves from this restraint on proliferation.

Growth suppressors stop proliferation by controlling the movement of the cell through its cell cycle. A cell decides if it will proliferate when in the  $G_1$  phase of the cycle; the transcription factor E2F plays an important role during this phase. If E2F is unaffected the cell moves into the S phase, where the DNA is synthesized, and then the cell prepares in the  $G_2$  phase to divide in the mitotic M phase [47]. Alternatively the tumour suppressor protein pRb (retinoblastoma) is released and binds to E2F which causes cells to either temporarily or permanently move from  $G_1$  straight into the quiescent  $G_0$  phase [29]. Cancer cells avoid this with some disruption to pRb, which allows E2F to play its role unaffected. pRb disruption can involve deactivation of the protein through a process called phosphorylation, or mutation of its gene, both of which prevent pRb from binding to E2F.

### **Evasion of apoptosis (cell death)**

When abnormalities are detected in the body, apoptotic effectors produce death factor receptors in these abnormal cells, which are then destroyed and absorbed by nearby cells. The p53 gene codes a p53 tumour suppressor protein, which is the main apoptotic sensor used to identify DNA damage. According to Juntila and Evan [90], most cancers must lose their p53 gene during mutation due to its severity on mutated cells, which is why they are able to evade apoptosis.

The gene is lost through deletion of DNA sections or mutation, which sometimes results in the release of tumour activators [85]. The gene can also undergo alternative splicing, which is when the mRNA transcribed from the DNA is rearranged before translation into amino acid chains, and produces an isoform of the original protein [112]. The restoration of the p53 gene from the mutation is now a popular idea in targeted cancer therapy, and some of these therapies have even reached the clinical trial stage and have started to show encouraging results, such as results shown by Nemunaitis et al. [108] and Duffy et al. [55].

### **Limitless replicative potential**

Even after a tumour possesses all of the above hallmarks, it still needs to overcome the limit on cell replication. Normal cells have limited replicative potential independent of the restrictions related to cell signalling; a cell can only multiply a certain number of times before it becomes permanently quiescent. Cancer cells seem to have no such limitation. When a normal cell multiplies, it loses DNA to the new cell from the ends of its chromosomes. These ends, called telomeres, protect the regular DNA from damage, and

get shorter and shorter as the cell continues to multiply, until eventually the telomeres are completely lost and the cell cannot multiply anymore, which is referred to as senescence. Cancer cells are able to maintain their telomeres so that the chromosome strands always stay above the critical length required. They achieve this by increasing production of the enzyme telomerase, which replicates the DNA in the telomeres to extend them [28]. The cancer cells will never cease to multiply, which is why this hallmark is also often called replicative immortality.

### **Sustained angiogenesis**

Angiogenesis is a biological process where new blood vessels grow from existing vessels to transport required nutrients to areas that need them. It is important in normal growth and development, and in the healing of wounds [50]. However, tumour angiogenesis is also vital to a tumour's continued growth. A tumour uses angiogenesis to acquire its own network of blood vessels, which is also called tumour vascularisation. Cancer cells are able to signal nearby blood vessels and induce the formation of new vessels that supply the tumour with oxygen and nutrients.

During normal processes such as wound healing a controlled amount of angiogenic factor such as Vascular Endothelial Growth Factor, or VEGF, is sent to nearby capillaries, along with angiogenic inhibitors such as thrombospondin 1, or TSP1, which results in an organised and efficient vascular system [24]. In tumour angiogenesis, there is little to no regulation of these proteins, allowing a large amount of angiogenic factor to be created and angiogenic inhibitor production is limited. This results in a less organised vascular system (see Figure 2.2).

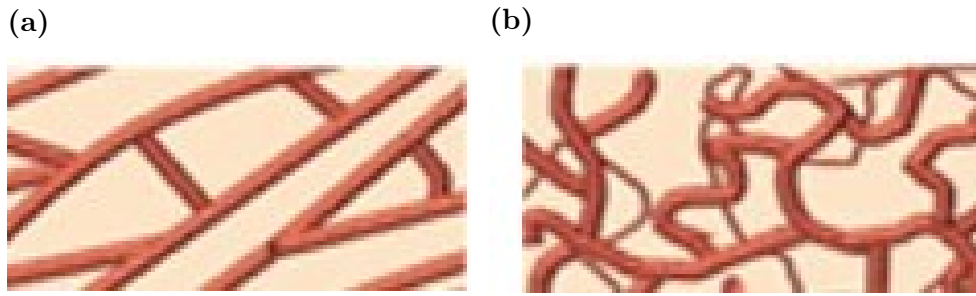


**Figure 2.2:** Illustrations of a vascular network created by angiogenesis, taking place during (a) physiological processes, such as wound healing, and (b) pathological processes such as tumour vascularisation. Notice the vast difference in number and thickness of capillaries. Pictures taken from Ledet and Mandal [97].

The earliest stages of tumour development involve direct diffusion of nutrient to and from the host tissue. Experiments on in-vitro or in-vivo isolated tumours show that growth of a tumour by diffusion alone eventually leads to a dormant steady state [62, 64]. In most cases it is not until after angiogenesis that a tumour is able to invade the nearby healthy tissue. Antiangiogenic therapies have become more popular, as the importance of angiogenesis in cancer has become more evident [161].

### **Invasion of healthy tissue and metastasis**

Cancer is defined by the invasion of healthy tissue by mutated cells [149], so it is understandable that invasion is a hallmark. Cancer cells proliferate outside their main tumour boundary into healthy tissue and destroy cells in this tissue. Proteins responsible for keeping cells within their own tissue include cell-cell adhesion molecules (CAMs) and cell-extracellular matrix adhesion molecules called integrins. Their genes are mutated in cancer cells, affecting the adhesiveness of the resulting protein and allowing cells to escape their original boundary.

After angiogenesis has taken place, there is less restriction on nutrients and tumour cells are able to grow a lot faster. This allows tumours to spread to other organs in a process known as metastasis. Cancer cells use the vascular system created through angiogenesis to form metastatic tumours in other parts of the body. Metastatic tumours cause severe damage to how the body functions and, according to Jones, most cancer deaths (90%) are caused by metastatic cancer, as once a tumour starts to spread it becomes increasingly difficult to treat. The primary goal of metastatic cancer treatment is usually to control its growth or to relieve symptoms caused by it [89].

The hallmarks are not necessarily acquired in the above order, although the order given is highly probable, especially considering the link between angiogenesis, invasion and metastasis. Since the publication of the “Hallmarks of Cancer” paper, attempts have been made to prove these hallmarks are indeed required for cancer, and mathematical models of each of these hallmarks have been developed which simulate them and look at possible ways each can be combated by therapy. See for example the model on tumour cell adaptation by Quaranta et al. [122], and the model by Spencer et al. [132] that predicted the times at which each of the hallmarks emerge during a tumour’s growth. More detail on some existing tumour growth models can be found in Chapter 3.

## 2.4 Angiogenesis

One of the hallmarks mentioned in Section 2.3, angiogenesis, has been studied in both biological and mathematical fields. Its vital role in not only the

vascularisation of a tumour but also in normal physiological processes such as embryonic growth and wound healing has made it a prominent area of study. The fact that angiogenesis is present in a normal healthy body means that antiangiogenic therapies for cancer may have dangerous consequences, and therefore must be targeted carefully. Although a link between angiogenesis and cancer was speculated previously, Folkman first proposed the necessity of angiogenesis for invasive growth in 1971 [62].

According to Bussolino et al. [31], there are multiple stages of angiogenesis. They are each important to the formation of an efficient vascular network. These stages are briefly described here.

### **Initiation**

Initiation is the onset of angiogenesis, where the endothelial cells in a blood vessel begin to change shape and have increased permeability. Angiogenic factors such as Vascular Endothelial Growth Factor (VEGF) are released and bind to the corresponding receptors on the surfaces of the endothelial cells. During this onset stage, some cells are chosen to migrate and form the vessel tips and others are chosen to remain as part of the original vessel wall and proliferate to create the walls of the new blood vessels.

This selective activation occurs through a type of cell-cell signalling where active cells inhibit their neighbour cells from sharing the same fate. This Delta-Notch signalling, named after the participating ligand Delta and its receptor Notch discovered by John S. Dexter in 1914 after noticing notches on the wings of the fruit fly *Drosophila melanogaster* [147], is an example of juxtacrine signalling, where the ligand remains anchored to its original cell so

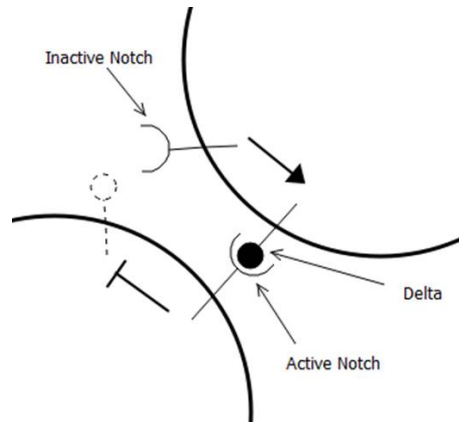


**Figure 2.3:** A simple depiction of Delta-Notch juxtacrine signalling between two cells. Delta activates neighbouring Notch receptors which inhibit Delta production in their own cell. This leads to inactive Notch receptors in the original cell and more Delta is produced as a result.

that only receptors in adjacent cells are activated [7]. The ligand Delta in a cell binds to the Notch receptors in adjacent cells, which inhibits Delta production in their own cell. Notch receptors in cells adjacent to this cell remain inactivated, which allows for further production of Delta in those cells. Cells with high Delta activity become surrounded by cells with low Delta activity and this signalling causes a pattern to emerge. Figure 2.3 portrays this Delta-Notch signalling between two cells.

Hellström et al. [84] discovered that Notch signalling occurs during angiogenesis with so-called Delta-Like Ligand 4 (DLL4); the activation of Notch receptors by DLL4 causes a down-regulation of VEGF receptors such as VEGFR2 [155] and thus only cells with higher DLL4 levels will migrate. This same Notch signalling is observed in many important biological mechanisms such as wing development in the fruit fly and proper functionality of the nervous system [23].

In tumour angiogenesis the Notch signalling is different; high levels of DLL4 in all endothelial cells cause the breakdown of effective Notch signalling and uncontrolled blood vessel growth [75]. It was believed that this increase of DLL4 production was simply due to an increase of Tumour Angiogenic Factor, or TAF production in the tumour cells; however, experimentation has proved that tumour vasculature has higher DLL4 levels than usual even in the absence of TAF [101].

### **Progression**

Progression is the stage after the endothelial cells have been activated by VEGF; the tip cells chosen in the earlier onset stage start migrating and the other cells proliferate behind the tip cells to start the formation of a new blood vessel. The extracellular matrix (ECM) is degraded by Matrix Metalloproteinases (MMPs) to release proteins important to angiogenesis such as pericytes and growth factors [27].

The structure of the vascular network forms during this stage, where the tip cells move towards the angiogenic factor source via chemotaxis, which causes migration in the direction of increasing factor gradient. Branching blood vessels is common in angiogenesis as a faster way to reach the factor source. Overexpression of VEGF in tumour angiogenesis causes a large amount of branching to occur to provide the tumour with a vascular supply as soon as possible. However, the cells have not yet formed blood vessels at this stage; the cells have not rearranged into the shape of a vessel with a hollow passage.

## **Differentiation and maturation**

Now the cells have started to migrate and proliferate, they need to form a new blood vessel with a lumen (passage where the blood flows). The new blood vessels are currently immature; with only endothelial cells present and no muscle cells, these vessels cannot function as they should. The muscles and pericytes, which regulate blood flow and stabilize the vessels, are needed for the blood vessels to function properly and are acquired during the maturation stage. The surrounding ECM is also reformed during this stage, where proteins that were destroyed in the progression phase are replaced.

In tumour vasculature, there is a lack of mature vessels, and so these poorly constructed vessels are often permeable, allowing blood to leak out. Sometimes there is even blood flow in both directions within the same vessel [107]. The absence of important adhesion proteins in the ECM causes the vessels to collapse easily. This provides difficulty in treatment; a treatment which relies on the vascular network to travel to affected areas will not be able to reach all tumour cells due to this vascular collapse.

## **Remodelling**

The reorganising of the blood vessel structure is sometimes carried out during the progression stage, but once the vascular network has developed and is fully functional, there may be an excess of blood vessels that are no longer required. During remodelling, the structure of the whole vasculature is reorganised into the most efficient arrangement by pruning any unnecessary blood vessels.

Vascular corrosion casting has previously been used to demonstrate remod-

elling in angiogenesis, where a solidifying liquid is poured into drained vasculature, allowed to solidify, and then the capillary walls are corroded away leaving a 3D cast [51]. This remodelling stage seems to be neglected in tumour angiogenesis, as there is little to no control in how the vascular system is structured (refer back to Figure 2.2).

Each stage listed above has been observed in physiological angiogenesis, but not always in tumour angiogenesis, in particular the maturation and remodelling stages. The defective nature of tumour angiogenesis can alone cause problems. Many biologists have been working on antiangiogenic therapy in cancer by preventing the onset of angiogenesis in the first instance, either by downregulating the angiogenic factor receptors or causing less angiogenic factor to be released from the tumour [141]. Such therapies do not work in all cases and sometimes cause issues by preventing angiogenesis required for normal function as well. Perhaps future antiangiogenic therapies could focus on the differences between physiological and pathological angiogenesis, or even on the Notch cell signalling to see if Notch receptor behaviour can be used against tumour growth.

## 2.5 Conclusion

This chapter presented a biological background of cancer and the mechanisms that drive it, including a brief explanation of each of Hanahan and Weinberg's hallmarks of cancer, and the stages in angiogenesis. Scientists have made a lot of discoveries regarding cancer development and treatment; there are now many ways to treat cancer and new treatments are continually being tested. However, it is still astounding how little is known about cancer as a whole

even after decades of dedicated research.

The Notch signalling in the onset of angiogenesis was described in Section 2.4. The importance of effective Notch signalling in the later stages of angiogenesis such as maturation and quiescence, as stated by Ehling et al. [56], explains the common absence of these stages in tumour angiogenesis, as Notch signalling is inadequate in tumour angiogenesis and therefore tumour vasculature is disorganised and defective. However, Notch signalling is still present and has been seen to have a positive effect on tumour growth. Research has found that blocking Notch signalling completely results in a decrease in tumour growth, but an increase in (non-functional) capillary formation [124]. Therefore one important aspect of tumour angiogenesis seems to be Notch signalling in earlier stages that is suppressed later. This realisation has inspired recent research into therapies that inhibit Notch signalling in angiogenesis (see for example [137, 160]). The coupling of a mathematical model of lateral inhibition to a model for angiogenesis could be used to investigate such therapies.

# Chapter 3

## History of mathematical models

### 3.1 Introduction

Mathematical models can investigate aspects of research that other methods cannot. Particularly within the field of medicine, where clinical trials and testing carries risk, mathematical models can fill in gaps in research and answer many questions. With appropriate parameter selection using experimental data, mathematical models have been shown to be highly accurate. Angiogenesis models by Balding and McElwain [11] and Levine et al. [99] very accurately recreated the behaviour of angiogenesis observed during in vivo experiments by Muthukkaruppan et al. [106], and a model of tumour growth by Byrne and Chaplain [33] even accurately simulated the growth of a tumour with a necrotic core independent of experimental data, and was confirmed to be accurate from research by Groebe and Mueller-Kliese [76].

Mathematical models are not just used to imitate systems in the real world; they can also be used to predict behaviour of systems in certain events. As just a small example, they can be used to simulate cancer therapies that

haven't yet been trialled, or to find weaknesses in tumour growth that can be exploited by therapy. Mathematical modelling has the benefit of being able to research any aspect of tumour growth without life-threatening consequences.

This chapter will examine more existing mathematical models in the areas of mathematical biology relevant to this work. An introduction to cell signalling models is given in Section 3.2, followed by a detailed review of angiogenesis models in Section 3.3. The history of phase field modelling, a useful modelling technique for moving boundary problems, is investigated in Section 3.4. Finally, in Section 3.5, there is a brief summary of the vast history of cancer models, and then the conclusion in Section 3.6 discusses the existing models and the research gaps in these areas.

## 3.2 Cell signalling models

This section covers models of cell signalling, in particular juxtacrine signalling, as named by Anklesaria et al. [7]. As mentioned in Chapter 2, juxtacrine signalling is defined as the signalling of cell receptors from ligands that remain anchored to the cell membrane. Therefore it is only neighbouring cells that partake in juxtacrine signalling. The first mathematical modelling of this neighbour signalling was studied by Othmer and Scriven in 1971 [116].

There has been research on modelling the Delta-Notch signalling mentioned in Chapter 2, Section 2.4. For example Collier et al. [45] analysed the pattern formation of this lateral inhibition-type juxtacrine signalling. Monk [105] suggested a further model of Delta-Notch signalling, which considered the inclusion of a third variable related to cell compliance to receptor activity.

Owen and Sherratt suggested a more complex version of the Collier model [117] which assumed much less, and therefore was a more general model. The model included decay of the ligand and receptors and internalisation of activated receptors. A later paper by Owen et al. mentioned potentially making the model continuous as a further step [118]. There have been continuous models to model cell interactions published by Gerisch and Chaplain [69] and Sherratt et al. [131], where cell-cell and cell-ECM adhesion in cancer were modelled using nonlocal integrals.

More recently, a model of Delta-Notch signalling by Shaya et al. [130] made a few biological conclusions about the predicted behaviour of the cell signalling, such as the properties of cells that are more likely to produce signals. Another model by Cohen et al. [44] used a lateral inhibition mechanism to simulate the pattern formation of hair cells in the mammalian ear.

### 3.3 Models of Angiogenesis

The importance of angiogenesis in tumour growth was first discussed in the 1970s, after Folkman made the “angiogenic switch hypothesis”, which suggested a strong link between angiogenesis and cancer development [62]. Although experimental research into angiogenesis began not long after Folkman proposed this hypothesis, mathematical models of angiogenesis emerged later in the 1980s and 1990s. An early model of angiogenesis by Deakin included an angiogenesis factor released by a tumour that activate receptors in the endothelial cells and initiates new capillary growth towards the tumour [49]. The results obtained were shown to be similar to results of laboratory experiments. Another presented in a paper by Balding and McElwain [11] modelled

capillary wall density and tip cell density separately. The migration of the tip cells depends on random motion and chemotaxis towards the source of angiogenic factor. Most other spatial models use this basic idea of modelling the reaction between capillary endothelial cells and tumour angiogenesis factors, and many take into account other biological mechanisms and chemical concentrations as well. Anderson and Chaplain, for example, introduced fibronectin into their model, a protein present in the extracellular matrix (ECM) which causes cell-ECM adhesion and has an important role in angiogenesis [4, 3].

### 3.3.1 Current methods of tip cell selection

As covered in Section 2.4, endothelial cells either become tip cells and migrate towards the source of VEGF, or they become stalk cells and proliferate to create a new blood vessel. The selection of tip cells is determined through juxtacrine signalling between cells. There are multiple approaches mathematicians have adopted to replicate this tip cell selection in models of angiogenesis.

Recall that Balding and McElwain treated the tips and walls of capillaries as separate entities [11], so that the different behaviour of tip cells and stalk cells can be modelled easier. Another idea is used in a discrete model by Travasso et al. [139] where some endothelial cells are assigned the migratory “tip” property and others the proliferative “stalk” property. An endothelial stalk cell can then only become a tip if none of its neighbours are tip endothelial cells.

Other methods of tip cell selection have been implemented, for example a model by Orme and Chaplain included the density of endothelial cells within the original capillary, and a cell in an area with high cell density would be

assigned the tip cell phenotype [113]. Orme and Chaplain later extended this model to two dimensions [114]. Levine et al. [98] developed a model that assigned tip cells based on cell-level processes such as the creation of sprout-forming enzymes. A model by Addison-Smith et al. [1] considered the presence of antiangiogenic factors that regulate sprouting.

The tip cell selection processes that take cell-level lateral inhibition into account have meant angiogenesis models including these have needed to be discrete or a hybrid discrete-continuous multiscale model. This has computational drawbacks when analysis of further aspects of angiogenesis such as the later stages (maturation, remodelling, etc.) is required. Although some hybrid models have been shown to work on a tissue level, the discrete aspect of the model can cause complexity in its coupling to the continuous component such as the possible locations of the discrete components not aligning with the continuous mesh, as discussed by Vilanova [143].

### **3.3.2 Differences between discrete and continuous models**

There is an abundance of both discrete and continuous models of angiogenesis; both have benefits and drawbacks which will now be discussed. Discrete models are able to model individual cell dynamics which is particularly useful when considering cell signalling. There are different types of discrete models depending on the purpose of the model; agent-based models allow for more detail and focus on individual “agents”, but are harder to compute, whereas cellular automata models often assume a uniform distribution of elements using a grid, and is one of most widely used computational methods, but can lack detail. Stokes and Lauffenburger used an agent-based stochastic model to

simulate branching [135, 134]; the probability of a new branch would increase the larger the distance from the vertex of an existing branch. The agents of this model are defined as each branch. An agent-based model of lateral inhibition in angiogenesis has been produced; Bentley et al. investigated the tip selection by Notch signalling in endothelial cells and how this relates to angiogenesis [14, 15]. The model focuses mostly on the cells in the original capillary; it is limited regarding the bigger picture of angiogenesis.

Anderson and Chaplain discretised a continuous model of theirs [3] into a cellular automata model which used probabilities dependent on TAF and fibronectin. They later extended this model in many subsequent papers to account for other features of angiogenesis [5, 6, 40]. A different type of discrete model called the Cellular Potts Model, while introduced by Graner and Glazier in 1992 [72], was not applied to angiogenesis until later [12, 136]. Many of the discrete models used cause predictability in the structure of the vasculature formed, mainly from the setting of the cell locations and sizes.

When the aim is to produce more general, larger-scale simulations of angiogenesis and therefore a computationally efficient method is required, or if an average representation of irregular cell distributions is required, a discrete model may not be suitable. This is when continuous models are useful. Continuous models of angiogenesis normally use a reaction-diffusion type equation to model the spatial change in blood vessel density. Angiogenesis is a complex process and continuous models are able to incorporate a number of the mechanisms involved; there have been models which consider ECM degradation [99] and even antiangiogenic therapies [4], and very recently the effect angiogenesis has on metastases [67]. Some models of angiogenesis onset mentioned

earlier, such as those by Orme and Chaplain [113, 114] and Levine et al. [98], are fully continuous. A continuous model by Anderson et al. [5] studied the role of angiogenesis in the suppression of a secondary tumour by the primary tumour, which results in the apparent sudden emergence of the previously undetected secondary tumour when the primary tumour is surgically removed.

A drawback of continuous models is that they cannot focus on individual discrete events easily; a multiscale model is required for this. A discrete multiscale model by Bauer et al. modelled angiogenic factor diffusion and endothelial cell behaviour on separate scales [12]. Multiscale models can also be continuous, such as Chaplain and Anderson's model with extracellular fibronectin interactions [39]. A more detailed review of multiscale models was written by Qutub et al. [123]. A multiscale model by O'Dea and King [111] investigated the effect Delta-Notch signalling has on macroscopic scales by deriving a continuous model based on the discrete Collier model using a so-called homogenisation technique where the microscale is assumed to be so small compared to the macroscale that its behaviour is considered to be homogeneous on the macroscale [115].

Multiscale models are often also hybrid models, where cellular scales are represented by discrete components and tissue scales use continuous equations. Hybrid models attempt to overcome the drawbacks of both discrete and continuous models by combining ideas behind each type. Travasso et al. models tumour angiogenesis using a continuous model but with a discrete representation of the tip endothelial cells [139]. Most hybrid models take the same form; Harrington et al. simulated angiogenic inhibitors as well a factors using continuous equations [82] and Das et al. used probabilities of cell state

transition in the discrete parts of their model [48]. A model by Carrier et al. consisted of three scales; an intracellular scale which modelled the cell signalling, a cell scale for the capillary formation, and a tissue scale modelling bone regeneration which requires angiogenesis [38].

### 3.4 Phase field modelling

A moving boundary problem describes a domain with two (or more) phases separated by a boundary. The movement of the boundary is determined by a set of evolution equations and boundary conditions. A moving boundary problem that uses phase change to model the moving boundary is called a Stefan problem, named for the physicist who first introduced these problems by modelling the solidification of water [133]. These moving boundary problems with different phases can also be used to model a variety of other multiphase systems, such as concentration or density levels of some description (such as concentration of tumour cells in a tumour growth model or endothelial cells in an angiogenesis model), or even different materials altogether (such as metals present in an alloy [96]).

The model equations for a moving boundary problem normally consider the boundary as a discontinuous change in phase, and thus are normally called sharp interface models. These sharp interface models are sometimes difficult to define due to this discontinuity at the interface. This means that suitable interface conditions are required, which can be challenging to find. Sharp interface models are also difficult to numerically simulate for several reasons, one being boundary-boundary interaction in the model, for example when boundaries collide and are supposed to merge [71].

Consider instead a problem with a boundary of a certain thickness, so that the phase smoothly changes across the boundary. These types of model introduce a new spatial variable that defines the phase. This so-called “order parameter”, or “phase field variable”, will give one value for one phase, another value for the other, and vary between these two values over the boundary. The idea behind these diffuse interface or phase field models is that they will behave like their sharp interface equivalent if the boundary thickness is sufficiently small. An example of a graph of such a phase field parameter  $\phi$  for both the sharp and smooth interface cases is shown in Figure 3.1

Phase field models have been developed for a variety of moving boundary problems; the first were solidification models such as for dendrite formation on snowflakes, for example. These first phase field models of solidification were derived by Fix in 1982 [61], Collins and Levine in 1985 [46], and Langer in 1986 [95]. Many phase field models of solidification followed these, along with models for various other multiphase systems, such as the tumour growth model by Hawkins-Daarud et al. [83] with not only tumour and healthy tissue phases but also nutrient-rich and nutrient-poor extracellular matrix phases, and Kobayashi’s model of the formation of crystal dendrites from metal casting [94].

Phase field models have been used for various purposes, but each of them use the original thermodynamic phase field theory derived by Cahn and Hilliard [36], and Allen and Cahn [2]. There are two types of phase motion; those where the mass in each phase is conserved, called phase separation, and those where the mass is not conserved, called phase transition. The Cahn-Hilliard

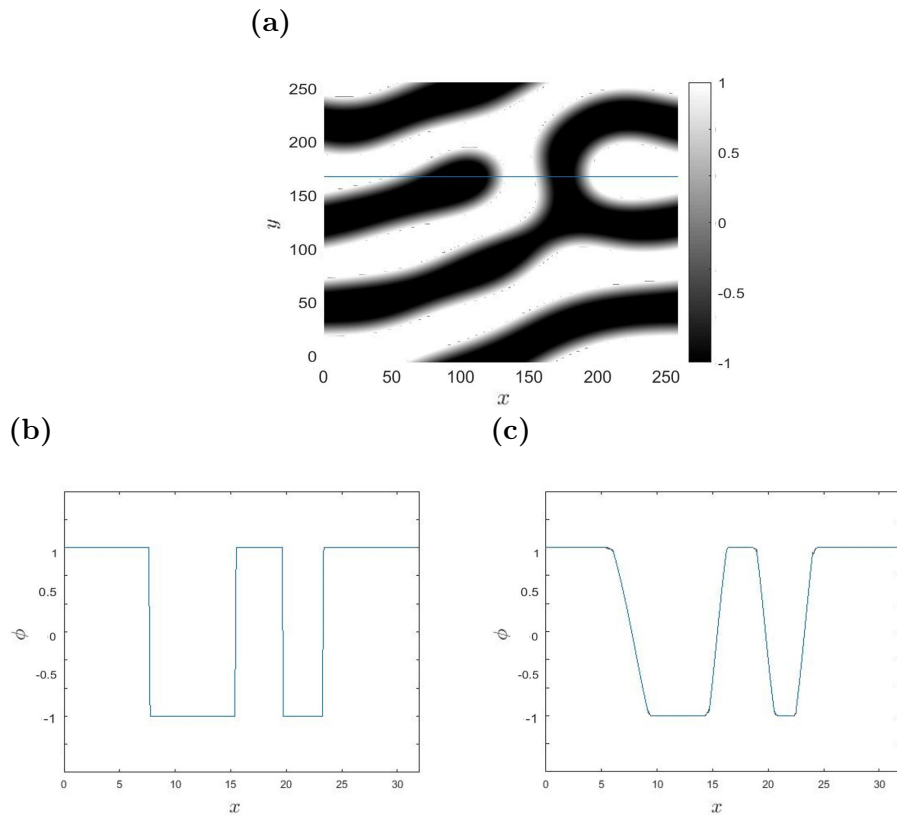


**Figure 3.1:** An example of how a phase field parameter is defined for a system with two phases. Shown is the values of  $\phi$  **(a)** over the whole two-dimensional domain **(b)** Along the line shown in **(a)** where there are sharp interfaces between the phases **(c)** Along the line shown in **(a)** where there are smooth interfaces. The phase field parameter  $\phi$  gives the value  $\phi = -1$  for the dark phase,  $\phi = 1$  for the light phase, and  $-1 < \phi < 1$  indicates a phase transition.

equation is derived from a mass balance law for conservation of mass and the Allen-Cahn equation from a law for non-conservation. Other models have been built using these two equations, such as the Navier-Stokes-Cahn-Hilliard equations for fluid flow [78], and various models that add extra reaction terms, such as Makki's model which considered the effect of internal microforces on the Allen-Cahn equation [102].

The use of phase field models for angiogenesis is a recent development; a model which was used to simulate angiogenesis in the presence of an angiogenic factor was proposed by Travasso et al. in 2011 [139] and variation of the amount of angiogenic factor produced at the factor source gave results which could be compared to the difference observed in normal and tumour angiogenesis. Vilanova [144] presented a version of this model that accounted for haptotaxis, which is the migration of cells towards active adhesion sites. As stated in Section 3.3 the Travasso model chooses the endothelial cells in the capillary that will become tip cells during angiogenesis by setting rules so that no two neighbouring cells can both be tip cells.

The phase field method shows huge potential for more applications; many more examples of how phase field modelling has been implemented can be found in the Encyclopedia of Computational Mechanics [71].

### **3.5 Mathematical modelling of cancer**

This section reviews models of tumour growth and other aspects of cancer. It is broken down into three parts; Section 3.5.1 reviews some of the first models of cancer, which primarily covered early stages of tumour growth; Section 3.5.2

reviews vascular tumour growth models, and Section 3.5.3 reviews tumour growth models which have made important discoveries and have in some cases motivated medical research.

### **3.5.1 Early models of carcinogenesis and avascular tumour growth**

Many mathematical models of cancer have surfaced over the last seventy years; some model tumour growth in general but there are others that focus on a specific aspect, such as the hallmarks of cancer, or the different stages of cancer development (although as hallmarks often develop at particular stages of development, these two are not entirely independent). One of the most investigated hallmarks, second only to invasion and metastasis, is the promotion of angiogenesis, which was discussed in greater depth earlier in Section 3.3.

Carcinogenesis is defined as the initial stages in cancer formation, which sometimes involves one or more of the hallmarks. A 1954 paper by statistician Armitage and epidemiologist Doll first suggested a model for the stages of carcinogenesis [10]. They considered cancer as the outcome of many previous genetic changes, and therefore mortality rates of cancer should differ with patient age. The model confirmed this theory by showing that the effect of carcinogenic factors differs with time. They also suggested that genetic changes could occur as a result of external factors, such as tobacco, inspired by Doll's earlier discovery that smoking can lead to lung cancer [52]. Another early and prominent model of the initiation of cancer was that of Knudson [93]. The model was of a particular type of retinal cancer that required two types of mutations occurring at specific times to develop. Knudson mentioned that it has been found that most cancers are thought to develop from more

than one type of mutation.

An area of mathematical cancer research that has been studied in depth by many researchers is tumour growth modelling. Early papers in tumour growth modelling were scarce compared to the vast research available now. Most tumour growth papers were written after 1990. There were a few papers released in the 1970s, but many people credit Greenspan for publishing one of the first models on avascular tumour growth in 1972 [73].

Imagine a small prevascular tumour that relies on diffusion only for obtaining nutrient and disposing of waste products. All cells are proliferating and well nourished at first. However, the more the tumour grows, the farther the nutrient has to travel to the centre. The concentration of the nutrient in the centre consequently decreases. The cells in the centre start to proliferate slower and soon become quiescent. Eventually the nutrient concentration falls below some critical value required to keep the cells alive and a necrotic core forms. With a decreasing number of proliferating cells as the tumour gets larger, the growth rate slows asymptotically and becomes essentially dormant. After a necrotic core emerges, there are three layers of different cell states; a thin outer layer of proliferating cells, an inner layer of non-proliferative, quiescent cells, and a necrotic core (see Figure 3.2).

The paper by Greenspan describes a mathematical model that represents this very simple reliance on diffusion only. A subsequent paper by Greenspan builds on this model by considering irregular growth, where the direction of growth is not strictly normal to the tumour surface [74]. This demonstrates a more realistic description of tumour growth which includes cell displacement,

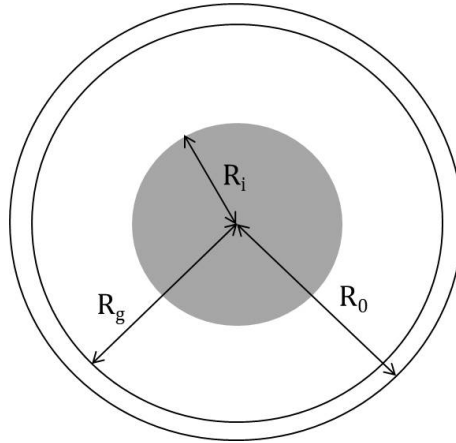


**Figure 3.2:** A diagram of an avascular tumour which relies on diffusion, with three different cell states; the outer proliferative rim  $R_g < r \leq R_0$ , the quiescent layer  $R_i < r \leq R_g$  and the necrotic core  $r \leq R_i$ , for distance  $r$  from the centre.

where cell density is not always constant. To represent such displacements in a model the dynamics which cause these cell movements must be considered. It is generally understood that the internal and external forces counteract each other which keeps the tumour's shape and therefore keeps the system stable, but if the external forces such as surface tension are overcome at some stage then future growth is unstable and the tumour becomes asymmetric, which leads to a further increase in instability. Greenspan performs a linear stability analysis on this model to see under which conditions the tumour loses stability.

There were a few earlier models of avascular tumour growth which Greenspan himself credited with motivating his work; however, Greenspan's work was more fundamental to cancer research and those models are the most referenced in later tumour growth work. The earlier models are similar to Greenspan's first model. One model by Thomlinson and Gray focuses on squamous cell carcinoma and in particular the cylindrical shape the tumours commonly form [138]. Burton also developed a model of spherical tumour growth similar to

Greenspan [30].

These earlier models of avascular tumours rely on diffusion only to transport nutrients and waste products. They will often reach a steady state where the proliferation rate is smaller than the rate of necrosis and tumour growth is paused. These avascular models make it clear that diffusion is no longer enough for further growth and a tumour is unlikely to become invasive without a sufficient blood supply.

### **3.5.2 Models of vascular tumour growth: introducing a blood supply**

Models of vascular tumour growth emerged to support antiangiogenic cancer therapy research motivated by Folkman's angiogenic switch hypothesis [62] linking angiogenesis and invasion. Another reason vascular mathematical models are so important is that experimental techniques by nature are more restricted than for the avascular case, as experiments must be conducted in vivo. Due to the complexity of such models, most did not surface until the 1990s. Among the first vascular models was a model by Hahnfeldt et al. [79] which looked at the effect of angiogenic activators and inhibitors on tumour growth, and suggested a potentially more effective antiangiogenic drug dosing method than the methods that existed at the time. A three-species multi-phase model by Breward et al. with the locations of tumour cells, extracellular matrix and blood vessels [26] was a variation of an earlier avascular model [25] which had a healthy host tissue phase instead of a blood vessel phase. Vascular models use different ways of representing the presence of blood vessels; the Breward et al. model represents blood vessels as a phase allowing for change in the vasculature shape, but some models include some nutrient

source and uptake to make the tumour vascular. The vascular version of the Greenspan model developed by Byrne and Chaplain, for example, altered the nutrient uptake rate by the tumour cells to represent different levels of tissue saturation [32]. A paper by Araujo and McElwain modelled the effect vascular collapse has on a tumour [9]. There have also been models which were coupled with angiogenesis models that already existed, such as a model of tumour growth by Xu et al. [159] which used the angiogenesis model developed by Travasso et al. [139], and a model from Cai et al. [37] that used an angiogenesis model they had developed previously [158].

A few vascular tumour models investigated the growth of tumour cords, which form when tumour cells gather around blood vessels instead of signalling the blood vessels to grow towards them. This time the outer surface is often hypoxic (oxygen-starved) or necrotic. Basic models by Bertuzzi et al. have a similar idea to early avascular models, with a nutrient source in the centre of a cylinder of cells [17]. Additions to the model such as radioresistance of the outer cells and the presence of a chemotherapy drug were later taken into account [18, 19].

### **3.5.3 Discoveries of tumour growth models**

A vast number of models are inspired by experimental findings, or by gaps in research which have led to implementation in experimental studies. For example, tumour encapsulation is a feature of tumours that is often used to determine a patient's prognosis; many benign tumours are encapsulated by a collagenous tissue but experiments failed to determine how these capsules form. There are two main theories on encapsulation; the "Expansive Growth Hypothesis" that states the growth of a tumour compresses the capsule into

the extracellular matrix and so a capsule forms passively when the tumour is not growing, and the “Foreign Body Hypothesis” that proposes an active involvement of the host tissue where the cancerous cells are recognised and the host responds by over-expressing collagen. Mathematical models by Jackson et al. simulate conditions representing the two theories separately and compare them [86, 100]. The models conclude that it is likely both hypotheses are true, as tumour suppression is not strong enough with just one hypothesis in action.

Internalisation of proliferating tumour cells into the central necrotic region of multicellular spheroids was also modelled in an attempt to prove this behaviour is due to passive migration following internal pressure gradients [103]. Results by Netti et al. [109] on the negative effect high blood pressure has on drug delivery were found to match experimental data, and the model has been used in attempts to find a solution to combat the problem [87]. As mentioned in the introduction of this chapter, a model by Byrne and Chaplain [33] successfully supported experimental evidence that a tumour’s size remains fixed once a necrotic core forms.

Models that investigate existing and potential cancer treatments have resulted in major breakthroughs in cancer research. An early model on cancer treatment by Wheldon et al. calculated optimal radiotherapy treatment schedules that result in the highest possible tumour death rate while maintaining a low healthy cell death rate [153, 154]. A model on chemotherapy drug delivery by Jain and Wei had a significant focus on the role of the vasculature [88]. A review paper which describes in further detail the impact mathematics has had on cancer research was written by Byrne et al. in 2006 [34], and Roose

et al. wrote a review on mathematical contributions to research in avascular tumour growth specifically [126].

This literature review is by no means exhaustive, and many other more detailed reviews of specific areas have been written by various authors. Araujo and McElwain for example wrote a review on tumour growth models [8] and Vilanova et al. shared the history of angiogenesis models [145], noting the huge diversity of models with regards to model type, numerical methods, and specific areas of research within angiogenesis. The review of mathematical impact on cancer research by Byrne et al. [34], mentioned above, even discussed the need for further collaboration between the clinical sciences and mathematics, as there is still a lack of use of mathematical research for clinical purposes.

### **3.6 Conclusion**

Detail of the existing mathematical literature on cell signalling, angiogenesis and cancer was covered in this chapter. There are too many types of avascular model in existence to mention all of them here as this was the main area of tumour growth researched before the angiogenic switch hypothesis [62]. There is a lack of mathematical material on cancer compared to the biological material; while this is understandable, as it is biological experimentation that ultimately proves theories, there are many unconfirmed hypotheses in oncology that could be supported or explained using mathematics. For example, therapies which are too risky to test on humans could be simulated to gauge the behaviour and risks of the drug.

A brief explanation and summary of phase field models were also given, which included a short description and the background of these models. A more in-depth mathematical explanation of phase field models is given later in Chapter 6, which will include the derivation of the Cahn-Hilliard and Allen-Cahn models [36, 2].

Most existing angiogenesis models select the migratory or tip endothelial cells in blood vessels by fixing an inhibition radius around every existing tip endothelial cell. This means the inhibition is very artificial in the way it is defined. The use of a model for Notch signalling would be a more accurate description. However, discrete models of Notch signalling require the locations of the endothelial cells to be defined, and coupling a discrete model to a continuous angiogenesis model would be complex.

The drawbacks of both discrete and continuous models were briefly mentioned. Recall that discrete models are computationally expensive on a tissue level, while continuous models are unable to simulate cellular level mechanisms in detail. Hybrid models overcome some of these drawbacks, but the computation is often still limited by the complexity of the coupling. Furthermore, the coupling of the discrete and continuous components could become complex especially if the angiogenesis model needs to be coupled further, such as to a tumour growth model.

A way to simulate lateral inhibition that avoids the above issues is an open problem in angiogenesis research. The work in this thesis aims to fill this research gap by producing a continuous model of lateral inhibition-type cell signalling to be coupled to a model of angiogenesis.

# Chapter 4

## A model of lateral inhibition

### 4.1 Introduction

As mentioned in Chapter 2, one of the six hallmarks of cancer is the ability to induce angiogenesis, the process during which new capillaries sprout from existing ones. Angiogenesis is required by hypoxic tissue to deliver oxygen; it is needed for normal growth and development, and damaged tissue requires oxygen to heal [50]. While it plays an important role in a healthy human body, it is also important for the continued growth and invasiveness of a tumour, providing it with its own source of nutrient [63].

Recall that angiogenesis is initiated through the activation of endothelial cells in the capillary wall by angiogenic factors released by a nearby hypoxic region, and the endothelial cells migrate and proliferate towards the factor source. Notch juxtacrine signalling enables tip cells selected for migration to inhibit their neighbour cells from also being selected [84]. The production of a ligand called Delta-Like Ligand 4 (DLL4) is induced by receptors for the angiogenic factor Vascular Endothelial Growth Factor (VEGF). DLL4 activates Notch

receptors in neighbouring cells, which inhibit the VEGF receptors in their own cell, as well as production of DLL4.

The Notch signalling works differently in pathological angiogenesis, especially in the later stages, given the high levels of DLL4 in all endothelial cells [75]. The particular reason for these elevated levels are still unclear, as removal of VEGF did not show much change in DLL4 production in experiments on tumour growth [101]. The onset of angiogenesis appears to be an important mechanism taken advantage of by cancer.

Chapter 3 discussed how existing models of angiogenesis select the migratory “tip” cells; some allocate them in initial conditions while others set simple conditions on tip cell emergence [139]. There are few models which have applied a lateral inhibition model to a model of angiogenesis, and those that have are discrete models such as the model by Bentley et al. [14].

A number of papers have already developed discrete models of lateral inhibition such as those by Collier et al. [45] and Owen and Sherratt [117], which presented the models that will be used in the next two chapters. Some of these models assume a homogeneous distribution of both cells and Notch receptors per cell, which from a biological point of view is not realistic. Consider a continuous model of lateral inhibition instead, which represents an average of endothelial cell locations and behaviour. A continuous model of receptor and ligand activity across the surface of a capillary could be applied to a continuous angiogenesis model to make the computation more straightforward and to limit unnecessary assumptions. Developing a continuous model to represent a discrete biological mechanism requires care.

The lateral inhibition model used is a model of Delta-Notch signalling, which is equivalent to the lateral inhibition-type signalling in angiogenesis onset except with ligands for different types of cell. The aim of this chapter and the next is to develop a fully continuous model of Notch and Delta activity. The chapters will each explore a different model; this chapter will derive a continuous extension of a model first published by Collier et al. [45] using a nonlocal weight function to represent the neighbour cell signalling, perform a linear stability analysis on the model, and produce simulations to demonstrate the similarities and differences from the discrete model. The aim is to show that the continuous model gives similar results to the discrete case and therefore can be used to represent lateral inhibition between endothelial cells in models of angiogenesis.

The chapter starts by discussing the challenges of modelling a discrete mechanism continuously in Section 4.2. In Section 4.3 the discrete lateral inhibition model which shall be converted is stated, followed by explanations on how the discrete components of the model will be made continuous. The continuous implementation of this model is then carried out in Section 4.4. A stability analysis defines the parameter values which cause unstable solutions for spatial perturbations in the model and therefore produce patterns in the results. These results are given in Section 4.5. Finally Section 4.6 concludes the chapter and discusses the benefits the model will provide to the later work in this thesis.

## 4.2 Continuous modelling of a discrete mechanism

Chapter 3 briefly discussed the differences between discrete and continuous models, and why one type may be chosen over the other. These differences will be discussed in a little more detail here. Discrete models are used when information about individual cells is required, as their treatment of each component in the model separately means they can keep track of cell locations and behaviour. They can look at discrete mechanisms such as interactions between components in more detail than continuous models can. Some models, such as agent-based models, focus on each individual element, which can record individual agent information.

Continuous models of biological systems are normally used when information is required on a larger scale. Because they are not as limited in space or time, continuous models allow for more effective computation. They can therefore provide insight into phenomena that a discrete model could not provide. Hybrid models couple discrete and continuous models to gain the benefits of both types, but the coupling can be highly complex, and even more so when further coupling is to occur.

The benefits of using a continuous model can also be applied to a discrete mechanism such as cell signalling. A discrete model will require cell location information to determine the cell behaviour, often resulting in the assumption that cells are regularly distributed, as depicted in Figure 4.1(a), and can be represented by a geometrical mesh, for example squares or hexagons. Continuous models have the advantage that the locations of the cells do not need to

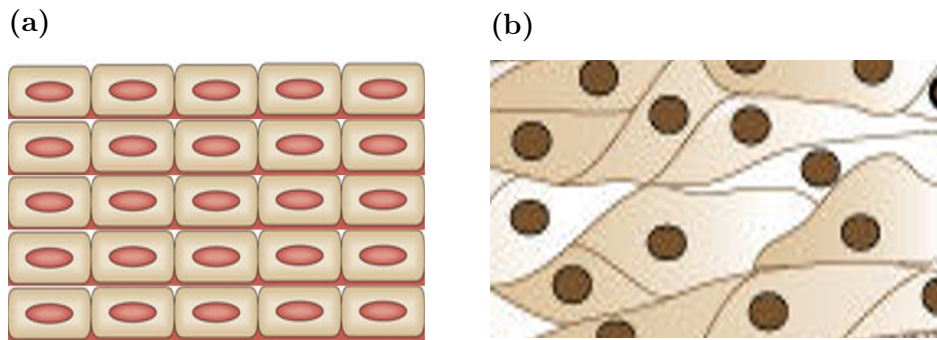


**Figure 4.1:** (a) A regular cell distribution often used in discrete models (b) A more realistic, irregular cell distribution, which can be represented generally by not setting cell locations and using a continuous model.

be known; they can take average data and work out the likely cell signalling behaviour from that information. The predicted ligand and receptor levels can be found for each point, as continuous models are not restricted to a mesh. Continuous models such as this can be used to represent the average behaviour of many types of cell distribution without changing the layout of the model each time. This is also more realistic, as both the cellular distribution in real life biological systems and the cells' shapes themselves are often irregular (see Figure 4.1(b)). A continuous model of cell behaviour can be coupled to other continuous models more easily, such as an angiogenesis model, to make a fully continuous multiscale model.

There are common problems in interpreting a continuous model in a biological setting, especially if it models discrete components. If a continuous model is used, the biological meaning must be preserved. The continuous model will consider endothelial tissue where the average ligand and receptor levels at a point are affected by the surrounding area, and locations at a distance of one average cell length from the point will have the greatest effect.

The spatial dependence of the Delta-Notch model comes in the form of the juxtacrine neighbour interactions. There are a variety of ways these interactions can be represented mathematically; a discrete model may find the ligand and receptor levels for each neighbouring cell and take the average, whereas a continuous model must introduce a spatially dependent weight function. The change in how this juxtacrine signalling is represented mathematically will be the main variation between the discrete and continuous versions of the model.

## 4.3 A Delta-Notch model

### 4.3.1 An existing discrete model

A one-dimensional discrete model of Delta-Notch signalling derived by Collier et al. [45], which will be used in the subsequent analysis, is stated here. The model is based on the signalling relationship between a cell  $j$  and its neighbours  $j_n$  shown in Figure 4.2. The one-dimensional model only considers the behaviour of a line or a ring of cells. The model is given as:

$$\begin{aligned} \frac{\partial n_j}{\partial t} &= f(\bar{d}_j) - n_j, \\ \frac{\partial d_j}{\partial t} &= \nu(g(n_j) - d_j), \\ f(x) &= \frac{A_1 x^p}{a^p + x^p}, \quad g(x) = \frac{A_2 b^q}{b^q + x^q}, \end{aligned} \tag{4.1}$$

with the levels of Notch receptor and Delta ligand activity in the cell  $j$  at time  $t$  denoted as  $n_j(t)$ ,  $d_j(t)$  respectively.  $\nu > 0$  is a ratio of the decay rates of Delta and Notch, which also means it is a ratio of the time scales of Delta and Notch activity, and  $a$ ,  $b$ ,  $p$ ,  $q$ ,  $A_1$  and  $A_2$  are chosen constants.  $\bar{d}_j$  is a spatial function determined by the Delta activity of the neighbours of cell  $j$ , which represents the juxtacrine signalling between Notch receptors

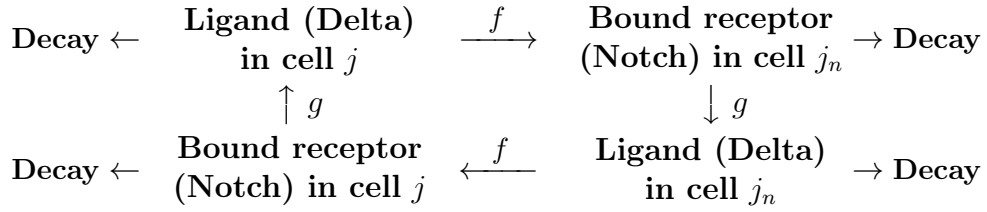


**Figure 4.2:** Relationships of the Delta-Notch model by Collier et al. [45], where  $j_n$  represents a neighbour cell of cell  $j$ . The model (4.1) is based on these relationships.

in cell  $j$  and Delta in neighbouring cells to cell  $j$ . This “average neighbour function” and its discrete and continuous forms will be discussed in detail next in Section 4.3.2. Delta activates Notch in neighbouring cells, which is why the function  $f$  is chosen to be an increasing Hill function. Notch inhibits Delta in its own cell which sets function  $g$  as a decreasing Hill function.

### 4.3.2 The average neighbour function

This section discusses the neighbour function which provides the spatial variation in the model, and considers potential forms this function could take in the continuous case in order to comply with the discrete case. The discrete equations (4.1) use the average neighbour function, which for a variable  $u$  takes the values of  $u$  in the neighbours of a cell  $j$  and finds the average. In one dimension, and therefore for two neighbours  $j - 1, j + 1$ , this is calculated as

$$\bar{u}_j = \frac{u_{j-1} + u_{j+1}}{2}. \quad (4.2)$$

The continuous equivalent  $\bar{u}(x, t)$  to the discrete average  $\bar{u}_j$  was defined by Owen et al. [118] as

$$\bar{u}(x, t) = \int_{-\infty}^{\infty} w(s)u(x - s, t)ds, \quad (4.3)$$

where  $x$  is the current position and  $s$  is the distance from position  $x$ . The weight function  $w(s)$  is a function to be chosen such that  $\int_{-\infty}^{\infty} w(s)ds = 1$ .

The Fourier transform  $\hat{w}(k)$  of the weight function  $w(s)$  will be important in the stability analysis of the continuous model in Section 4.4, where it is found that unstable solutions will require  $\hat{w}(k) < 0$  for some  $k$ . Therefore a potential weight function will have a Fourier transform that is sometimes negative.

This section investigates the potential weight functions that  $w(s)$  in (4.3) could take the form of. Some of the weight functions are derived by averaging other more basic weight functions that are based on different cell sizes and locations. In one-dimension, this could be considered as an average representation of a two-dimensional irregular cell distribution, where the  $x$ -direction locations of neighbour cells for each cell in an irregular distribution, such as the one shown earlier in Figure 4.1(b), are recorded, and the average of these neighbour locations are taken.

### **Averaging using rectangle functions**

There are a number of types of function that  $w(s)$  could be set as; the function selected will depend on the model itself and the desired outcome of the model. The weight function perhaps most analogous to the discrete neighbour

function (4.2) is two rectangle functions with the weighted sections covering the most likely locations of two neighbour cells to a cell in the centre. This weight function is shown in Figure 4.6(a), and the function is written

$$w(s) = \begin{cases} \frac{1}{2} & 0.5 < |s| \leq 1.5, \\ 0 & \text{otherwise,} \end{cases} \quad (4.4)$$

with Fourier transform

$$\hat{w}(k) = \frac{2 \sin(\frac{k}{2}) \cos(k)}{k} = \text{sinc}\left(\frac{k}{2}\right) \cos(k), \quad -0.6651 \leq \hat{w}(k) \leq 1. \quad (4.5)$$

One of the reasons for using a continuous model is to be able to model using average cell locations, because the cells in a biological setting are unlikely to be all the same size and distributed evenly, as shown in Figure 4.1(b). However, the rectangle weight function (4.4) contradicts this and still suggests a regular array of cells. To find a weight function that does not assume a regular array, an average weight function must be found using randomised cell distributions.

To do this, five cells are defined over a space of five times an average cell length by randomising the distribution of each cell edge. A restriction that the cell lengths must fall between 0.5 and 1.5 of the average cell length is applied. Numerically this is achieved by applying a uniform probability distribution to the locations of the cell edges, restricting them to fall within 0.5 of the regular cell edge locations. The leftmost boundary of cell one and the rightmost boundary of cell five are fixed at 0 and 5 respectively, for all randomisations. A weight function similar to the rectangle weight function (4.4) is then calculated at the centre of cell three of each randomisation, and depends on the varying size and location of cells two and four. The average

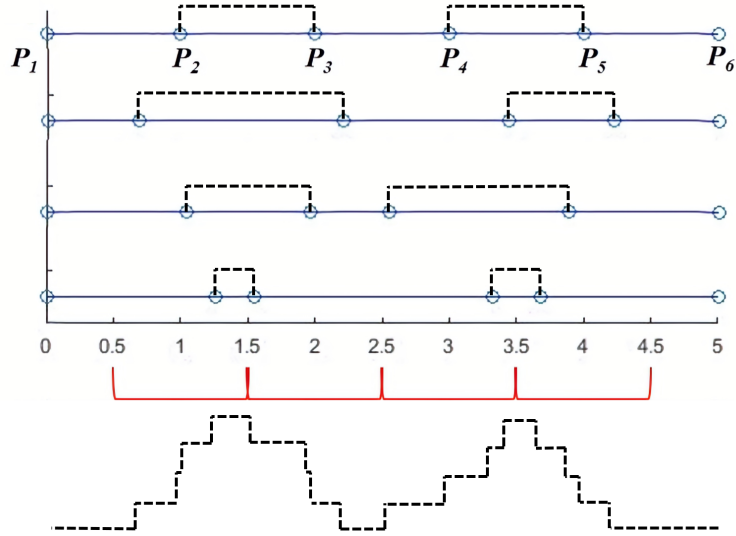


**Figure 4.3:** Possible cell distributions of five cells over five average cell lengths. The points  $P_1$ - $P_6$  shown represent the edges of the cells. The first distribution is a regular cell distribution, with edges at 0, 1, 2, 3, 4, and 5 average cell lengths. Three randomised distributions are then shown. The cell lengths and locations are found using uniform probability distributions by setting  $P_1 = 0$ ,  $P_6 = 5$ , and restricting  $P_2 - P_5$  to the corresponding red area indicated (i.e.  $0.5 < P_2 \leq 1.5$ ,  $1.5 < P_3 \leq 2.5$ , etc.). The shape of the corresponding rectangle functions are shown with dotted lines, and the general shape of the average of these four weight functions is shown at the bottom. Notice that the most weight in the average function is located at the centre of cells 2 and 4 of the regular distribution.

of these weight functions is then taken. This idea is represented visually in Figure 4.3. If enough random cell distributions are used to find an average weight function, they give a graph that looks similar to two triangle functions with a maximum of 0.5 at a distance of 1 and -1 away from the centre point. As expected, locations that are one average cell length away will have the most impact. An average graph produced from 100 cell randomisations is shown in Figure 4.5(a). The triangle weight function that can be used to

estimate this average takes the form

$$w(s) = \begin{cases} \frac{|s|}{2} & |s| \leq 1 \\ \frac{(2-|s|)}{2} & 1 < |s| \leq 2 \\ 0 & \text{otherwise,} \end{cases} \quad (4.6)$$

which has Fourier transform

$$\hat{w}(k) = \frac{2 \cos(k)(1 - \cos(k))}{k^2}, \quad -0.4726 \leq \hat{w}(k) \leq 1. \quad (4.7)$$

The average graph Figure 4.5(a) has curves which are slightly steeper than the straight lines of the corresponding triangle function, shown in Figure 4.6(b), which means the maximum height is at around 0.557 to maintain the total area of one.

The average weight function calculation is strongly affected by the way the cell distributions and sizes are selected; the above selection uses a uniform probability distribution for each cell edge with uniform probability for potential cell edge locations. This gives a triangular shaped probability distribution for the lengths of the cells, ranging from lengths of 0 and 2, and peaking at 1. The cell lengths determine the locations of the rectangles in the weight function; therefore it stands to reason that the average of all these weight functions will take the same shape as the probability distribution for the lengths.

Another way to determine the cell edge locations is to use a normal probability distribution instead, with a mean  $\mu$  equal to the individual locations of the regular cell distribution edges and a standard deviation of the mean of

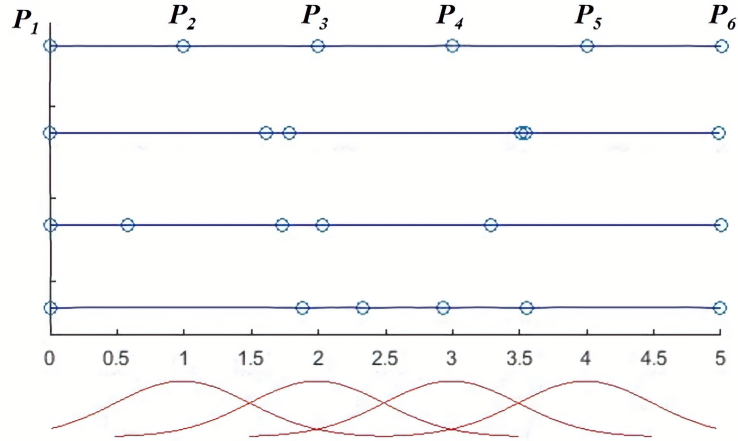


**Figure 4.4:** The regular cell distribution followed by three random cell distributions found using normal probability distributions shown in red. Any crossover of points during selection, for example if  $P_4 < P_3$ , is corrected by relabelling (e.g.  $P_4$  becomes  $P_3$  and vice versa).

$\sigma = 0.5$ , of the form

$$\frac{1}{\sqrt{2\pi\sigma^2}} e^{-\frac{(x-\mu)^2}{2\sigma^2}}. \quad (4.8)$$

The edge locations are no longer restricted to an interval. The normal distribution allows cell edges to cross over, which effectively means cells overlap. To fix this the edges are sorted in space order after selection. This new cell distribution allocation method is demonstrated in Figure 4.4. The corresponding probability distribution for the length is also a normal distribution, with a mean of 1 and a standard deviation of 1.

Because the centre of the domain ( $x = 2.5$  in Figure 4.4) does not necessarily lie in the same cell for each distribution this time, the centre cell will change. The cell which contains the centre of the domain is found and designated the centre cell for each randomisation.

These normal probability distributions result in a similarly shaped weight

function, shown in Figure 4.5(b). It has maxima at distances of 1 and -1 away from the centre, with a value of around 0.3433, and a local minimum of zero at the centre. This can be closely estimated by the product of an absolute value function and a Gaussian function, which has the general form

$$w(s) = l|s|e^{-ms^2}. \quad (4.9)$$

Setting  $m = 0.5$  gives the required maxima at  $s = 1$  and  $s = -1$ . The value of  $l$  then needs to be set so that the integral of the weight function equals one. The integral of  $lse^{-ms^2}$  is  $-\frac{l}{2m}e^{-ms^2}$ , giving the whole integral

$$\int_{-\infty}^{\infty} w(s)ds = \left[-le^{-\frac{s^2}{2}}\right]_0^{\infty} + \left[le^{-\frac{s^2}{2}}\right]_{-\infty}^0 = 2l = 1, \quad (4.10)$$

which sets  $l = 0.5$ . The appropriate weight function, which shall be denoted the Gaussian-derived weight function, is then

$$w(s) = \frac{|s|}{2}e^{-\frac{s^2}{2}}, \quad (4.11)$$

and its graph is shown in Figure 4.6(c). Its Fourier transform is

$$\hat{w}(k) = \int_{-\infty}^{\infty} \frac{|s|}{2}e^{-\frac{s^2}{2}-iks}ds, \quad (4.12)$$

and the minimum value of this is found to be  $\hat{w}_{\min} = -0.2847$ . The graph of this Fourier transform, along with the Fourier transforms of the rectangle and triangle weight functions ((4.5) and (4.7) respectively), can be found in Figure 4.7.

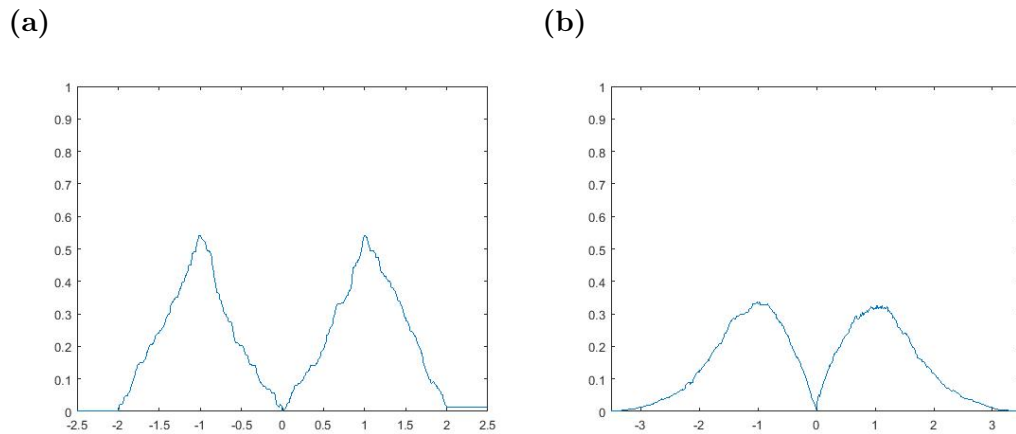


**Figure 4.5:** The weight functions found by averaging different rectangle functions which were calculated from randomised cell distributions. **(a)** A triangle-type weight function found using uniform cell distributions, which can be estimated by equation (4.6), the sum of two triangle functions. **(b)** A smoother weight function found using normal cell distributions, estimated by the product of an absolute value and Gaussian function (4.11).

### Averaging using delta functions

The rectangle weight function (4.4) used to produce the triangle and Gaussian-derived weight functions (4.6) and (4.11) above may not be an accurate choice, although it first appears to be the natural continuous version of the discrete neighbour function. The issues become clear when the biological implications are considered; the contribution made by a cell to its neighbouring cell should not emerge from everywhere in the cell, as the above weight functions suggest. A weight function that shows a contribution from only one small area of the cell may be more accurate. It must not be forgotten that although the model will be continuous, the fact that cell signalling is a discrete process will not change.

A more realistic weight function uses the Dirac delta function (not to be confused with the ligand Delta). The Dirac delta  $\delta(s)$  has a value of zero

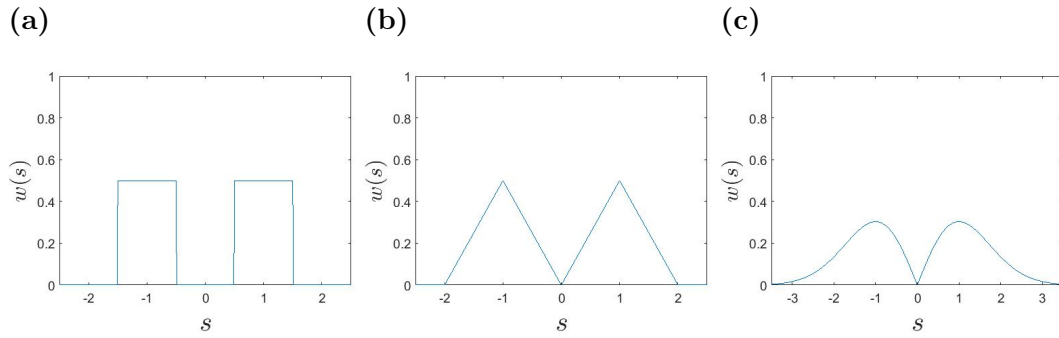


**Figure 4.6:** The weight functions considered; (a) the Rectangle weight function (4.4), (b) the Triangle weight function (4.6), (c) the Gaussian-derived weight function (4.11).

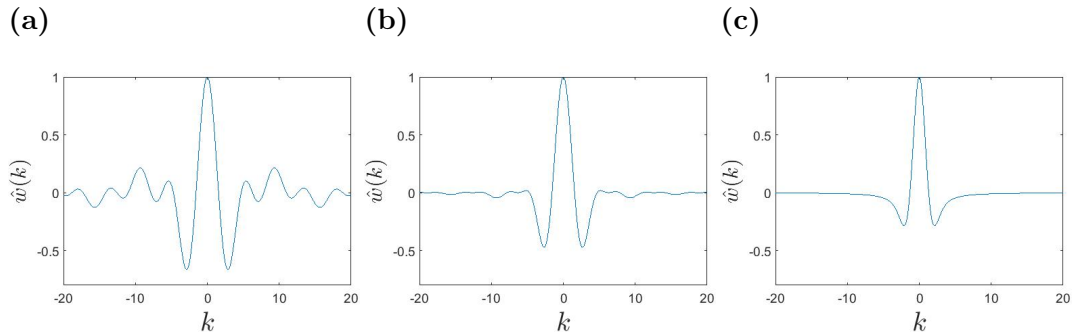


**Figure 4.7:** The Fourier transforms of the (a) Rectangle weight function, (4.5), (b) Triangle weight function, (4.7), (c) Gaussian-derived weight function, (4.12).

everywhere except at  $s = 0$ , at which it is infinite, and it has the property that its integral equals one. Using a weight function where a half-delta function (with area  $1/2$  instead of  $1$ ) is placed at the centre of each neighbouring cell gives a neighbour function which is comparable to the discrete neighbour function (4.2). One possible approximation of a delta function shifted to a location  $x$  with area  $1/2$  takes the form

$$\frac{1}{2l\sqrt{\pi}}e^{-\frac{(s-x)^2}{l^2}}, \quad (4.13)$$

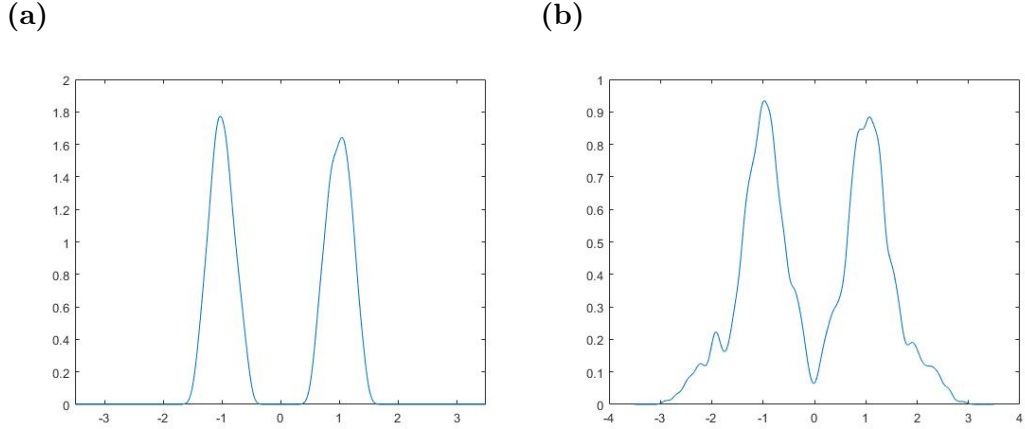


**Figure 4.8:** The weight functions calculated by averaging delta weight functions of 1000 cell realisations; **(a)** using a uniform distribution to randomise the cell edges **(b)** using a normal distribution to randomise the cell edges.

where  $l$  is small and positive. Therefore the delta weight function, with neighbour cell centres at  $x_1$  and  $x_2$ , is

$$w(s) = \frac{1}{2l\sqrt{\pi}} \left( e^{-\frac{(s-x_1)^2}{l^2}} + e^{-\frac{(s-x_2)^2}{l^2}} \right). \quad (4.14)$$

Averaging weight functions based on equation (4.14), corresponding to many random cell realisations for both uniform and normal distributions for the cell edges, gives the graphs shown in Figure 4.8.

Notice that the resulting weight functions from the averaging of the delta functions are fairly similar shapes to the weight functions found when the rectangle functions were used instead. Therefore this suggests that the weight functions (4.6) and (4.11), which estimate these average functions, are still both suitable for use in this continuous model.

## The two-dimensional function

Neighbour cell locations in a two-dimensional model are somewhat more complicated, mainly because of the greater number of options of two-dimensional lattices, and hence the greater variation in the possible number and location of neighbour cells. A new two-dimensional average neighbour function is needed. One example of a two-dimensional average neighbour function for the discrete model, where each cell is considered to have four neighbours, takes the form

$$\bar{u}_{j,k} = \frac{u_{j-1,k} + u_{j,k-1} + u_{j,k+1} + u_{j+1,k}}{4}, \quad (4.15)$$

where  $u_{p,q}$  is the  $u$ -value in the cell in row  $p$ , column  $q$ . The options for neighbour selection are greater in particular for irregular cell distributions, such as the one pictured in Figure 4.1(b). For example, choosing a four-neighbour square lattice and randomising the  $x$  and  $y$  lengths of each element, using the delta function method above, would place delta functions at the centres of each of the four neighbours. Averaging would result in a triangle or absolute-Gaussian function with peaks at each centre, and the same result would be achieved for a hexagonal six-neighbour lattice. However, continuous models do not require a lattice for cells, and maintaining a mean equal to one for the distance between the centres of adjacent cells means a two-dimensional weight function can be derived by rotating the one-dimensional weight function about the  $w$ -axis to give rotational symmetry.

The two-dimensional version of the rectangle weight function for example forms an annulus shape with some value  $h$  to be determined, with outer ra-

dius 1.5, inner radius 0.5, and is defined in cylindrical polar coordinates as

$$w(r, \theta) = \begin{cases} 0 & r \leq 0.5, \\ h & 0.5 < r \leq 1.5, \\ 0 & r > 1.5. \end{cases} \quad (4.16)$$

To satisfy  $\int_0^{2\pi} \int_{0.5}^{1.5} w(r) r dr d\theta = 1$ ,  $h$  is set as  $h = \frac{1}{2\pi}$ .

The Fourier transform  $\hat{f}(\rho, \phi)$  of a two-dimensional function  $f(r, \theta)$  in polar coordinates, where Cartesian wavenumbers  $k_1$  and  $k_2$  can be written in terms of polar wavenumbers  $\rho$  and  $\phi$  as  $k_1 = \rho \cos \phi$ ,  $k_2 = \rho \sin \phi$ , is

$$\begin{aligned} \hat{f}(\rho, \phi) &= \int_0^\infty \int_0^{2\pi} f(r, \theta) e^{-ir\rho(\cos \phi \cos \theta + \sin \phi \sin \theta)} r d\theta dr, \\ &= \int_0^\infty \int_0^{2\pi} r f(r, \theta) e^{-ir\rho \cos(\theta - \phi)} d\theta dr, \end{aligned} \quad (4.17)$$

which for an  $f$  with rotational symmetry can also be written as

$$\hat{f}(\rho, \phi) = \int_0^\infty 2\pi r f(r) J_0(-\rho r) dr, \quad (4.18)$$

where the zero-order Bessel function of the first kind  $J_0$  is defined as

$$J_0(x) = \frac{1}{2\pi} \int_0^{2\pi} e^{ix \cos(\theta - \phi)} d\theta. \quad (4.19)$$

Therefore the Fourier transform for the two-dimensional rectangle function (4.16) is

$$\hat{w}(\rho, \phi) = \int_{0.5}^{1.5} r J_0(-\rho r) dr, \quad -0.2337 \leq \hat{w}(\rho, \phi) \leq 1. \quad (4.20)$$

The weight function (4.16) in one dimension reduces to the one dimensional rectangle weight function (4.4).

The similar two-dimensional version of the triangle weight function is

$$w(r, \theta) = \begin{cases} \frac{r}{2\pi} & r \leq 1, \\ \frac{(2-r)}{2\pi} & 1 < r \leq 2, \\ 0 & r > 2, \end{cases} \quad (4.21)$$

and the two-dimensional Gaussian-derived weight function is of the form

$$w(r, \theta) = hre^{-\frac{r^2}{2}}. \quad (4.22)$$

The required value  $h$  for a total volume of one is found using the known value of the Gaussian integral:

$$\int_{-\infty}^{\infty} e^{-mx^2} dx = \sqrt{\frac{\pi}{m}}. \quad (4.23)$$

Integrating by parts finds

$$\begin{aligned} \int_0^{2\pi} \int_0^{\infty} hre^{-\frac{r^2}{2}} r dr d\theta &= 2\pi h \int_0^{\infty} r \left( re^{-\frac{r^2}{2}} \right) dr, \\ &= 2\pi h \int_0^{\infty} e^{-\frac{r^2}{2}} dr, \\ &= 2\pi h \left( \frac{1}{2} \sqrt{2\pi} \right) = h\pi\sqrt{2\pi} = 1, \end{aligned} \quad (4.24)$$

which sets  $h = 1/\sqrt{2\pi^3}$ . The two-dimensional rectangle, triangle and Gaussian-derived weight functions are shown in Figure 4.9.

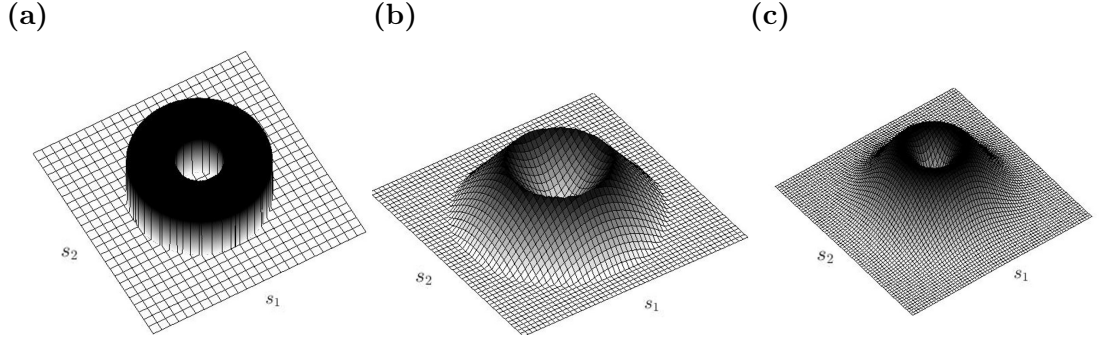


**Figure 4.9:** The two-dimensional continuous weight functions, which are extensions of the one-dimensional (a) Rectangle weight function, (4.16), (b) Triangle weight function, (4.21), (c) Gaussian-derived weight function, (4.22).

The Fourier transforms for the two-dimensional triangle and Gaussian-derived weight functions are

$$\hat{w}(\rho, \phi) = \int_1^2 r(2-r)J_0(-r\rho)dr + \int_0^1 r^2J_0(-r\rho)dr, \quad (4.25)$$

$$-0.1692 \leq \hat{w}(\rho, \phi) \leq 1,$$

and

$$\hat{w}(\rho, \phi) = \int_0^\infty \sqrt{\frac{2}{\pi}} r^2 e^{-\frac{r^2}{2}} J_0(-r\rho) dr, \quad (4.26)$$

$$-0.0826 \leq \hat{w}(\rho, \phi) \leq 1,$$

respectively, and are shown in Figure 4.10.

## 4.4 Implementation of the continuous version of the model and stability analysis

The continuous model replaces  $n_j(t)$ ,  $d_j(t)$  with  $n(x, t)$  and  $d(x, t)$ , the averages of Notch and Delta activity at position  $x$ . Here the endothelium of a

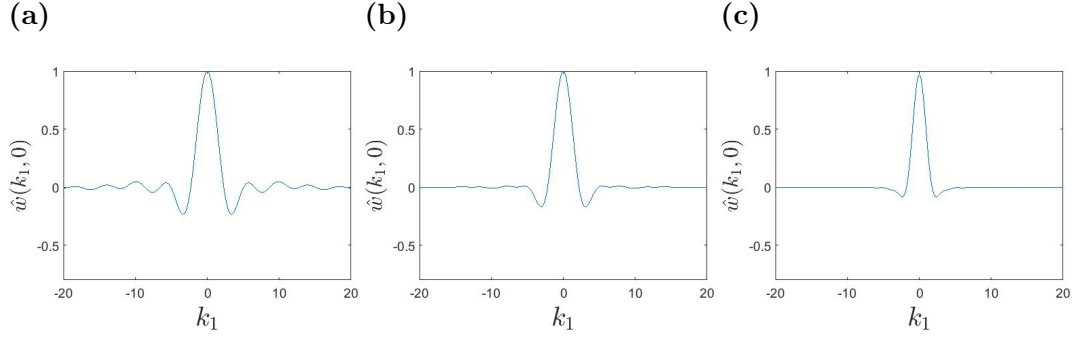


**Figure 4.10:** Fourier transforms for the two-dimensional versions of the (a) Rectangle weight function, (4.20), (b) Triangle weight function, (4.25), (c) Gaussian-derived weight function, (4.26), at  $k_2 = 0$ , for  $-20 \leq k_1 \leq 20$ .

capillary wall is considered, instead of a particular endothelial cell in a system of cells. The continuous model is written as:

$$\begin{aligned} \frac{\partial n}{\partial t} &= f(\bar{d}) - n, \\ \frac{\partial d}{\partial t} &= \nu(g(n) - d), \end{aligned} \quad (4.27)$$

$$f(x) = \frac{A_1 x^p}{a^p + x^p}, \quad g(x) = \frac{A_2 b^q}{b^q + x^q},$$

where the average neighbour function is given in equation (4.3) as

$$\bar{u}(x, t) = \int_{-\infty}^{\infty} w(s)u(x - s, t)ds. \quad (4.28)$$

A linear stability analysis, based on the work of Turing [140], shall now be performed on this model (4.27)-(4.28). For steady state solutions, the activated Notch and Delta values  $n_e$ ,  $d_e$  are the same for all cells. Therefore  $\bar{d}_e = d_e$  and

$$f(d_e) = n_e, \quad g(n_e) = d_e. \quad (4.29)$$

Applying small perturbations  $\tilde{n}(x, t)$ ,  $\tilde{d}(x, t)$  to these steady states of the form

$$\tilde{n}(x, t) = Ne^{\alpha t + ikx}, \quad \tilde{d}(x, t) = De^{\alpha t + ikx}, \quad (4.30)$$

where  $N$  and  $D$  are constants and  $\alpha$  and  $k$  are the growth rate and wavenumber, gives the average Delta as

$$\begin{aligned} \bar{d}(x, t) &= \int_{-\infty}^{\infty} d_e w(s) ds + \int_{-\infty}^{\infty} \tilde{d}(x-s, t) w(s) ds, \\ &= d_e + \int_{-\infty}^{\infty} \tilde{d}(x, t) w(s) e^{-iks} ds, \\ &= d_e + \tilde{d}(x, t) \hat{w}(k), \end{aligned} \quad (4.31)$$

where  $\hat{w}(k)$  is the Fourier Transform of  $w(s)$ . Substituting this in to equations (4.27) and using Taylor expansions, the equations become

$$\begin{aligned} \alpha \tilde{n} &= \mathcal{F} \tilde{d} \hat{w} - \tilde{n}, \\ \alpha \tilde{d} &= \nu (\mathcal{G} \tilde{n} - \tilde{d}), \end{aligned} \quad (4.32)$$

with  $f'(d_e) = \mathcal{F}$ ,  $g'(n_e) = \mathcal{G}$ . Recall function  $f$  is an increasing function and function  $g$  is a decreasing function, which means  $\mathcal{F} > 0$  and  $\mathcal{G} < 0$ . Equations (4.32) can also be written in matrix form:

$$\begin{pmatrix} \alpha + 1 & -\mathcal{F} \hat{w} \\ -\nu \mathcal{G} & \alpha + \nu \end{pmatrix} \begin{pmatrix} \tilde{n} \\ \tilde{d} \end{pmatrix} = 0. \quad (4.33)$$

The characteristic equation for this matrix is

$$\alpha^2 + (1 + \nu)\alpha + \nu - \hat{w} \mathcal{F} \mathcal{G} \nu = 0. \quad (4.34)$$

Solutions  $\tilde{n}(x, t)$ ,  $\tilde{d}(x, t)$  are stable over time for  $\text{Re}(\alpha) < 0$ , so that

$$\tilde{n} = Ne^{\alpha t + ikx} \rightarrow 0, \quad \tilde{d} = De^{\alpha t + ikx} \rightarrow 0,$$

for large  $t$ . Patterning requires stability (both solutions have  $\text{Re}(\alpha) < 0$ ) for homogeneous spatial perturbations (wavenumber  $k = 0$ ) and instability for inhomogeneous spatial perturbations. A little observation finds that stability requires

$$1 + \nu > 0, \quad 1 - \hat{w}(k)\mathcal{F}\mathcal{G} > 0. \quad (4.35)$$

Recall that  $\nu > 0$ , which makes the first condition always true. Therefore the stability of the system depends on the second condition (4.35)<sub>2</sub>, which is true if  $\hat{w}(k) > 0$ , due to the product  $\mathcal{F}\mathcal{G}$  being negative. For homogeneous perturbations,  $\hat{w}(k) = \hat{w}(0) = \int_{-\infty}^{\infty} w(s)ds = 1$ , therefore the system is always stable for homogeneous perturbations.

To achieve unstable solutions for inhomogeneous perturbations, as the first stability condition is true everywhere, the second stability condition must be violated, so that

$$\frac{1}{\mathcal{F}\mathcal{G}} > \hat{w}(k). \quad (4.36)$$

For this to happen,  $\hat{w}(k)$  must be negative for some value of  $k$ . The weight functions proposed earlier in Section 4.3.2 all have Fourier transforms which are negative for some  $k$ , as shown in Figure 4.7.

To find the most unstable solution, the most negative, or smallest value of  $\hat{w}$  must be used, i.e.  $\hat{w}_{\min}$ , to find the most positive, or largest value of  $\alpha$ , i.e.  $\alpha_{\max}$ . For the rectangle weight function (4.4) the minimum value of its trans-

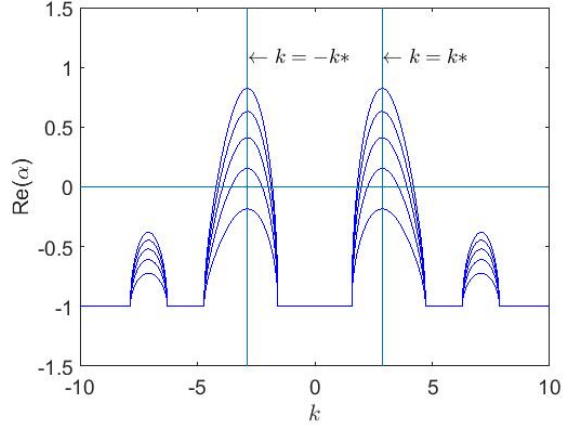


**Figure 4.11:** Dispersion curve  $(k, \alpha)$  for the rectangle weight function (4.4) where the function  $w(s)$  has Fourier transform  $\hat{w}(k) = \text{sinc}(\frac{k}{2}) \cos(k)$ , for  $\mathcal{FG} = -1, -2, -3, -4,$  and  $-5$ . As  $|\mathcal{FG}|$  increases, the value for  $\alpha_{\max}$  increases.  $\mathcal{FG}$  can be changed by changing the parameter values  $a$  and  $b$ .

form is  $\hat{w}_{\min} = -0.6651$ . The wavenumber  $k = k^*$  for which  $\alpha$  is the largest gives  $\hat{w}(k^*) = \hat{w}_{\min}$  and wavelength  $\lambda^* = \frac{2\pi}{k^*}$ . The critical value of  $\mathcal{FG}$  for which the stability of the system changes is  $\mathcal{FG}_{\text{crit}} = 1/\hat{w}_{\min} \approx -1.504$ . Figure 4.11 shows the dispersion curve for the rectangle weight function which shows the highest value for  $\alpha = \alpha_{\max}$  is obtained at wavenumber  $k = k^* \approx 2.8686$  and wavelength  $\lambda \approx 2.1903$ .

## 4.5 Simulation of the lateral inhibition model

Simulations of the model (4.27) were produced for two different types of boundary conditions, which are only required for Delta as Notch does not have a spatial effect. For domain size  $L$  and mesh size  $h$ , the periodic boundary conditions set the Delta concentrations near the edges of the domain to affect those on the other edge ( $d(0, t) = d(L + h, t)$ ), and the fixed Dirichlet conditions set values on the boundary to zero ( $d(0, t) = 0, d(L, t) = 0$ ). The area where the pattern first emerges depends solely on the initial condition for

periodic boundary conditions; however, the fixed boundary conditions generate a perturbation which causes the pattern to very rapidly emerge at the boundaries first, which was also observed in results by Collier et al. [45]. The initial conditions for Notch and Delta provided the required inhomogeneous spatial perturbation to make it possible for patterns to emerge:

$$n(x, 0) = 1 - \mathfrak{r}(x) \quad d(x, 0) = 1, \quad (4.37)$$

where for each  $x$ ,  $\mathfrak{r}(x)$  is a random number between 0 and 0.05. The Delta-Notch model is simulated using a Runge-Kutta fourth-order method. The integral (4.28) is estimated at each mesh point  $x$  using a rectangle method, where the values of  $w(y)d(x - y)$  are calculated for each mesh point  $y$  and are summed together.

Parameters in equations (4.27) were set by Collier et al. as

$$a = 0.1, \quad b = 0.1, \quad p = 2, \quad q = 2, \quad \nu = 1, \quad A_1 = 1, \quad A_2 = 1,$$

to achieve unstable results. These are the parameter values taken for all results in this section, unless specifically stated otherwise. The time scale of the model is proportional to the decay rate of Notch, which for the selected  $\nu$ -value is also equal to the decay rate of Delta. Continuous results with fixed boundary conditions that use the rectangle weight function are given in Figure 4.12 and show similarities to the discrete results found by Collier et al. [45], where the values seem to converge to their steady states before destabilising and forming a pattern, although the continuous results reach their final state at a later timestep; they take about twice the amount of time to develop as the discrete results with the same  $\mathcal{FG}$  value. This is related to the change in the average neighbour function and the minimum value  $\hat{w}_{\min}$ .

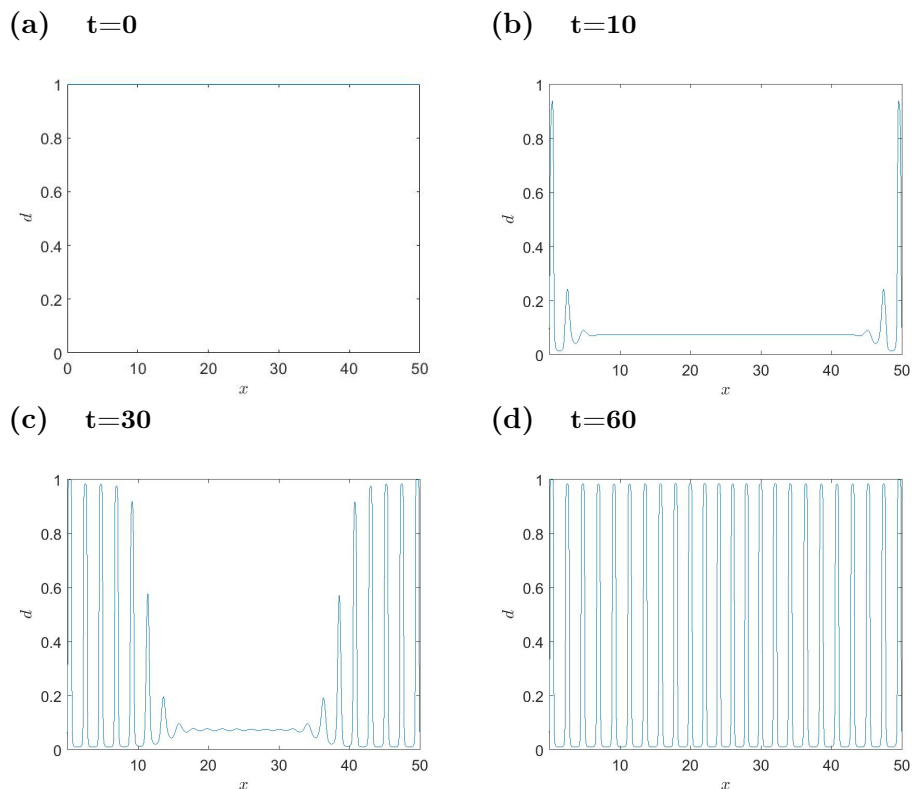
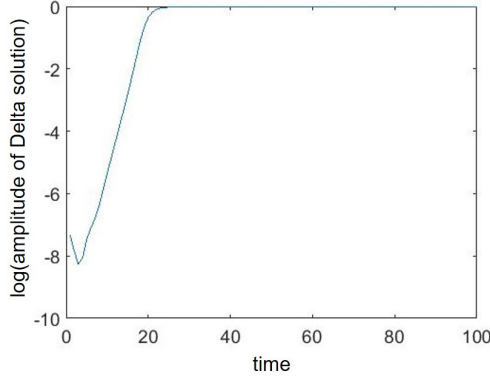


**Figure 4.12:** Continuous results with fixed boundary conditions at (a)  $t = 0$ , (b)  $t = 10$ , (c)  $t = 30$ , and (d)  $t = 60$  for Delta levels over a domain size of 50. The mesh size is  $h = 0.01$ . The weight function used for the average neighbour function in this simulation is the rectangle weight function. The wavelength is  $\lambda^* \approx 2.1903$ , compared to  $\lambda^* = 2$  for the discrete case. The slightly larger wavelength causes fewer peaks to emerge.

The discrete solution has  $\hat{w}(k) = \frac{e^{-ik} + e^{ik}}{2} = \cos(k)$  and its critical value of  $\mathcal{FG}$  is therefore  $\mathcal{FG}_D = 1/\hat{w}_{\min} = -1$ . The critical value of  $\mathcal{FG}$  for the continuous solution using the rectangle weight function was stated earlier as  $\mathcal{FG}_{\text{crit}} \approx -1.504$ , which gives a smaller growth rate  $\alpha$  for the same parameter values and therefore has more stable solutions.

The growth rate  $\alpha$  of the simulation is the change in amplitude of the Delta

(a) Discrete model



(b) Continuous model

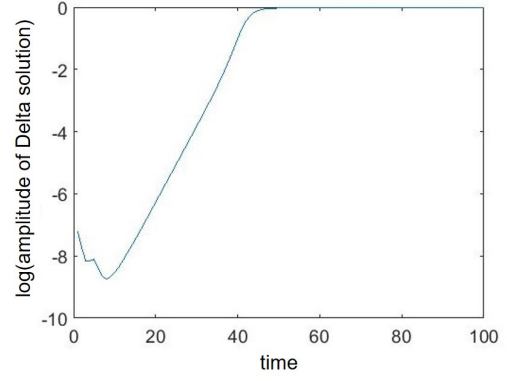


**Figure 4.13:** Graphs  $\log(d_{\text{amp}}(t)) \approx \log(\mathcal{D}) + \alpha t$  of the amplitude  $d_{\text{amp}}(t) = d_{\text{max}}(t) - d_{\text{min}}(t)$  of the Delta solution over time, for **(a)** the discrete model, finding  $\alpha \approx 0.547$ , **(b)** the continuous model, with  $\alpha \approx 0.266$ . The growth rate  $\alpha$  calculated from these graphs can be used to find the wavenumber  $k$  and wavelength  $\lambda$ .

concentration wave solution over time. The amplitude is defined as  $d_{\text{amp}}(t) = d_{\text{max}}(t) - d_{\text{min}}(t)$ , where  $d_{\text{max}}(t) = d(x_l, t)$  and  $d_{\text{min}}(t) = d(x_s, t)$  are the largest and smallest Delta values at time  $t$  respectively. As the fixed boundary conditions cause large waves at the boundaries early on before waves in the middle develop, the amplitudes will be calculated from periodic boundary solutions. Taking the logarithm of the amplitude will nearly give a straight line graph with respect to time  $t$ :

$$\log(d_{\text{amp}}(t)) \approx \log(\mathcal{D}) + \alpha t, \quad (4.38)$$

where  $\mathcal{D}$  is constant. An approximation of  $\alpha$  can be found from the gradient of this graph, which is plotted in Figure 4.13.

The growth rate  $\alpha$  can be used to find  $\hat{w}_{\text{min}}$  and then an approximation of the

dominant wavenumber  $k^*$ , once  $\hat{w}(k)$  is calculated. The wavenumber can be checked by finding the wavelength of the Delta solution from the results and comparing this to  $\lambda^* = 2\pi/k^*$ , which should be similar. The wavenumber for the discrete model is  $k^* = \pi$ , which gives a wavelength of  $\lambda^* = 2$ . This is expected, as there are two cells per wave period. The wavenumber for the continuous case is found from the minimum value of the Fourier transform of the weight function, which for the rectangle function is  $\hat{w}_{\min} \approx -0.6651$  giving a dominant wavenumber of  $k^* \approx 2.8687$ , and a wavelength of  $\lambda^* \approx 2.1903$ . The wavelength is slightly greater in the continuous solutions than for the discrete solution; this has resulted in fewer peaks in total over the given domain.

Stability and formation of a pattern depends on the value of  $\mathcal{FG}$ , which depends on the parameters  $a$  and  $b$ . Figure 4.14(a) shows a bifurcation curve for bifurcation parameter  $a$ , found by setting  $b = 0.1$  and calculating the final amplitude of the solution for different values of  $a$ . The curve identifies for which value of  $a$  the homogeneous steady state becomes unstable, and has the characteristics of a supercritical pitchfork bifurcation where the steady state becomes unstable as it reaches its critical value at  $a \approx 0.02$ . Figure 4.14(b) plots  $a$  against  $\mathcal{FG}$  instead; the critical value  $\mathcal{FG}_{\text{crit}} \approx -1.504$  is reached for the same critical  $a$ -value  $a \approx 0.02$ , but stability is reached again for  $a \approx 1.96$  where  $\mathcal{FG}$  meets  $\mathcal{FG}_{\text{crit}}$  again. The critical values of  $\mathcal{FG}$  are also shown for the triangle and Gaussian-derived weight functions.

Results using the other weight functions suggested in Section 4.3.2 vary from the results using the rectangle function. As shown in Figure 4.14(b), the critical  $\mathcal{FG}$  values  $\mathcal{FG}_{\text{crit}}$  change due to the change in the Fourier transform  $\hat{w}(k)$ , and hence in its minimum value  $\hat{w}_{\min}$ . The triangle function (4.6),

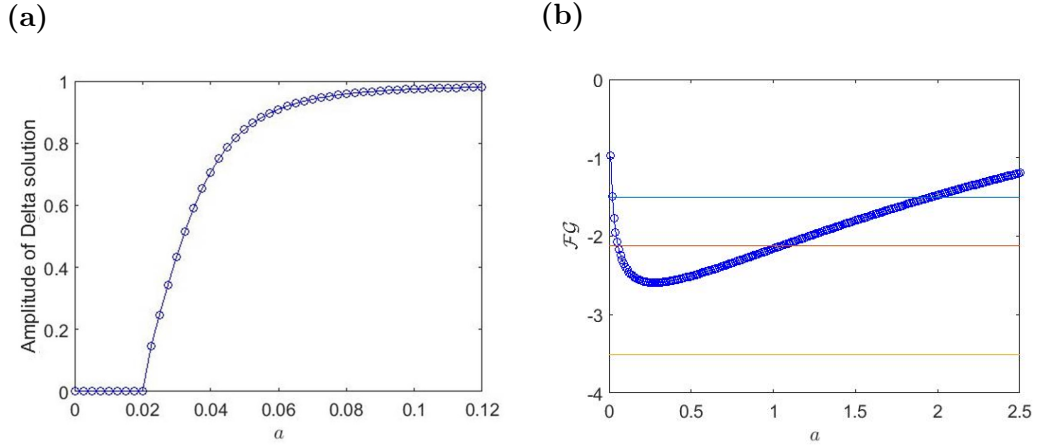
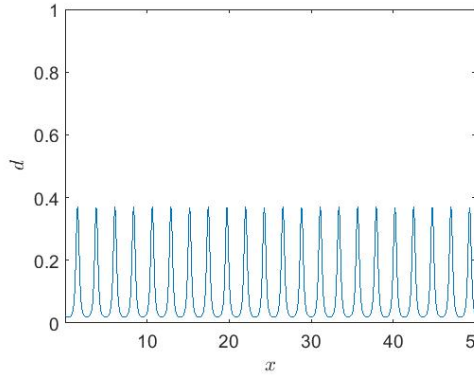


**Figure 4.14:** (a) Bifurcation curve which plots changing  $a$  between 0 and 0.12 against the amplitude of the resulting final solution, with the other parameter values the same as previously stated. (b) A graph of  $a$  between 0 and 2.5 against  $\mathcal{FG}$ , where the critical  $\mathcal{FG}$  values are shown for each of the three weight functions introduced earlier; the rectangle weight function's value in blue, the triangle function's value in red, and the Gaussian-derived function's value in yellow. Note that the critical  $\mathcal{FG}$  value for the discrete model is  $\mathcal{FG}_D = -1$  and so the discrete solutions are unstable for the stated parameter values for  $b, p, q, \nu, A_1, A_2$ , and all values  $0 \leq a \leq 2.5$ .

with  $\hat{w}_{\min} = -0.4726$  and therefore a harder to reach critical  $\mathcal{FG}$  value of  $\mathcal{FG}_{\text{crit}} = -2.1161$ , gives results shown in Figure 4.15(a), which has a smaller amplitude for the same parameter values as the earlier results for the rectangle function in Figure 4.12. The Gaussian-derived function (4.11) has  $\hat{w}_{\min} = -0.2847$ ,  $\mathcal{FG}_{\text{crit}} = -3.5125$ , meaning results with the original parameter values are stable to all perturbations, which can be deduced from the earlier  $a$ - $\mathcal{FG}$  plot Figure 4.14(b). The solution shown in Figure 4.15(b) has values  $a = 0.05$  and  $b = 0.005$  instead, and still only shows a small amplitude. The bifurcation curves for the results of the triangle and Gaussian-derived weight functions are given in Figure 4.16, and shows the critical value of stability at  $a = 0.06$  for the triangle function and critical values of  $a = 0.02$  and  $a = 0.81$  for the Gaussian-derived function.

(a) Triangle WF



(b) Gaussian-derived WF

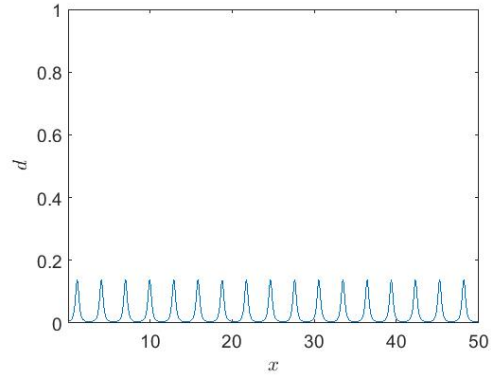
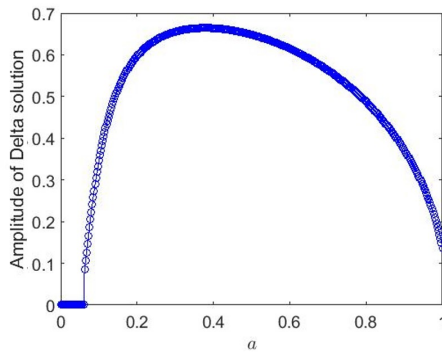


**Figure 4.15:** Periodic solutions which show the final Delta levels over a domain size of 50 average cell lengths using (a) the triangle weight function, where  $a = 0.1$ ,  $b = 0.1$ , and the amplitude of the solution is about 0.39, and (b) the Gaussian-derived weight function, which has  $a = 0.05$  and  $b = 0.005$ , with an amplitude of around 0.14.

(a) Triangle WF



(b) Gaussian-derived WF

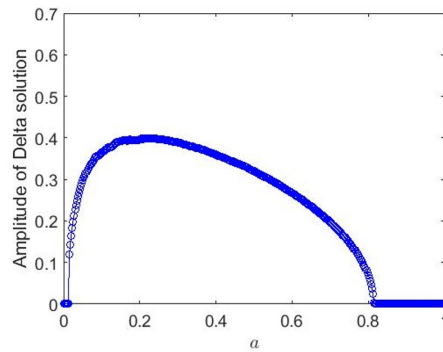


**Figure 4.16:** Bifurcation curves for changing  $a$  from 0 to 1 with original parameter values for all other parameters except  $b$ , where the weight function used is (a) the triangle function with  $b = 0.1$ , showing a maximum amplitude of 0.65 at  $a \approx 0.4$  and critical stability value  $a = 0.06$ , (b) the Gaussian-derived function with  $b = 0.005$ , and a maximum amplitude of about 0.4 at  $a = 0.2$  and two critical stability values at  $a = 0.02$  and  $a = 0.81$ .

In the model as it is, once the pattern emerges it spreads everywhere. However, in angiogenesis, new capillaries only form in areas where the angiogenic factor VEGF is present; the pattern does not continue to spread along the capillary. To adjust the model to take this into account, consider the bifurcation parameters  $a$  and  $b$ . If one of these is made a spatial function dependent on  $x$ , then stability (and patterning) can be varied across the domain. The function  $a(x)$  is set to

$$a(x) = \frac{1}{2}e^{-\frac{(x-x_{\text{VEGF}})^2}{10}}, \quad (4.39)$$

with its most unstable point at  $x = x_{\text{VEGF}}$ ,  $a = 0.5$  and then a decrease in instability on either side. The bifurcation diagram shows that the critical value for  $a$  is around 0.02. Therefore the function is divided by 2 to allow more  $x$ -values to be stable (i.e.  $a(x) < 0.02$ ). In terms of angiogenesis,  $a(x)$  can be considered the VEGF-function, with the point of highest VEGF concentration at  $x = x_{\text{VEGF}}$ . Simulations implementing this function are shown in Figure 4.17, with  $x_{\text{VEGF}} = 10$ . The values of  $a$  and  $b$  affect the steady state solutions, which is why when the values appear to converge to their steady states at the beginning, the steady state levels approached vary in space (see 4.17(b)).

A two-dimensional version of the Delta-Notch model is not as similar to one-dimension as perhaps first assumed, especially given the similarities between the one and two-dimensional discrete models as shown by Collier et al. [45]. However, the two-dimensional weight functions considered in Section 4.3.2 make some of the differences between the one and two-dimensional models clearer. The two-dimensional version of the rectangle weight function is used here, which is given in equation (4.16). The two-dimensional model is simply

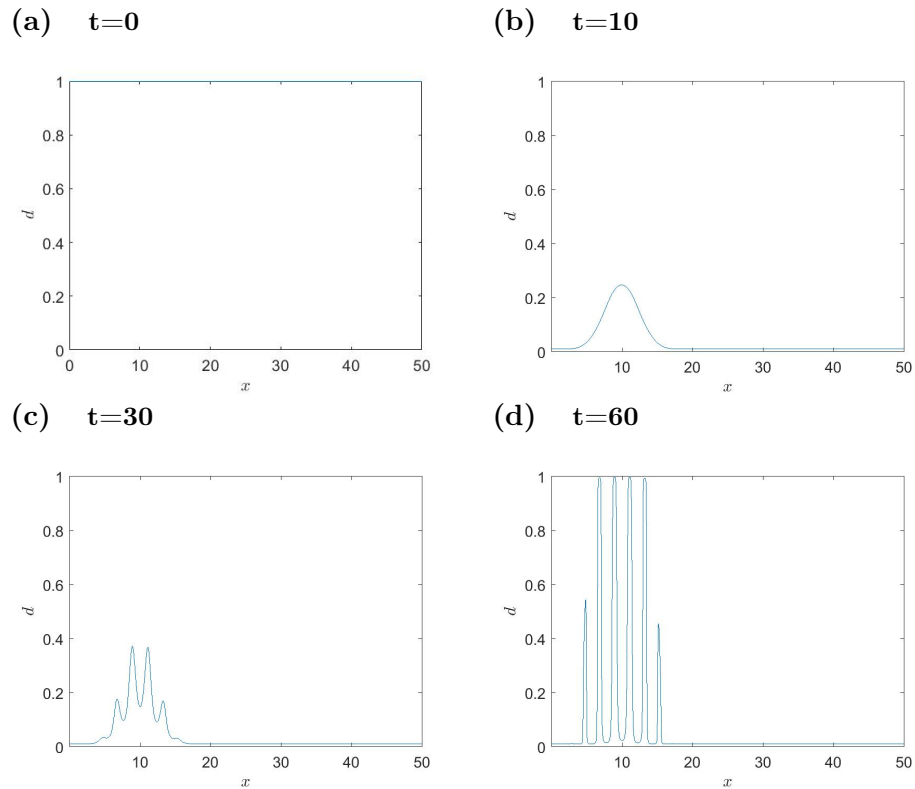


**Figure 4.17:** Delta results with  $a(x) = \frac{1}{2}e^{-\frac{(x-10)^2}{10}}$ , at the same times as before: (a)  $t = 0$ , (b)  $t = 10$ , (c)  $t = 30$ , and (d)  $t = 60$ , with fixed boundary conditions, and with the rectangle weight function. The pattern only emerges in one area of the domain, due to the VEGF function  $a(x)$ .

written as follows:

$$\begin{aligned}\frac{\partial n(\mathbf{x}, t)}{\partial t} &= f(\bar{d}(\mathbf{x}, t)) - n(\mathbf{x}, t), \\ \frac{\partial d(\mathbf{x}, t)}{\partial t} &= \nu(g(n(\mathbf{x}, t)) - d(\mathbf{x}, t)),\end{aligned}\tag{4.40}$$

with  $\mathbf{x} = (x, y)$ , and average Delta concentration  $\bar{d}(\mathbf{x}, t)$

$$\bar{d}(\mathbf{x}, t) = \int_{-\infty}^{\infty} w(\mathbf{s})d(\mathbf{x} - \mathbf{s}, t)ds.\tag{4.41}$$

The minimum value that the 2D rectangle Fourier transform (4.20) can take is  $\hat{w}_{\min} \approx -0.2337$ , giving the critical  $\mathcal{FG}$  value as  $\mathcal{FG}_{crit} \approx -4.2793$ . The functions  $f(\bar{d})$ ,  $g(n)$  with their current parameter values for  $p$  and  $q$  are unable to reach this value for  $\mathcal{FG}$ , even with changes to  $a$  and  $b$ ; therefore the  $p$  and  $q$  values must be changed. Two-dimensional results with periodic boundary conditions, first without and then with a VEGF-function implemented, both produce a hexagonal pattern, and are shown in Figures 4.18 and 4.19. This pattern suggests the hexagonal lattice used for the discrete model is the most realistic layout of cells.

Without a VEGF function, the pattern again covers the whole domain; whether it emerges everywhere at once, like in Figure 4.18, or if it emerges in one location and eventually spreads everywhere. The introduction of the VEGF function limits the pattern to a small area of the domain.

## 4.6 Conclusion

This chapter has introduced and simulated a continuous mathematical model of Delta-Notch signalling and has shown that such a model produces sta-

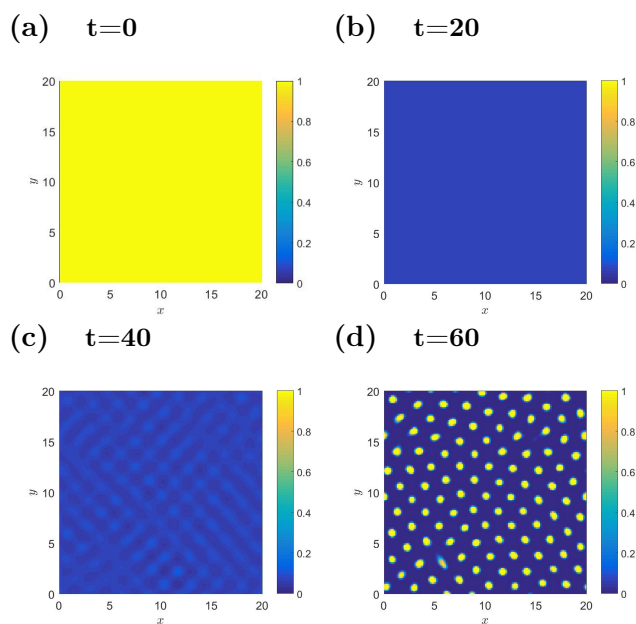


**Figure 4.18:** Two-dimensional periodic results for Delta concentrations on a  $20 \times 20$  domain and a  $140 \times 140$  mesh, for (a)  $t = 0$  (b)  $t = 20$  (c)  $t = 40$  and (d)  $t = 60$ . The weight function used is the 2D rectangle weight function. Parameters are  $p = 3$ ,  $q = 3$ ,  $a = 0.1$ ,  $b = 0.1$ ,  $A_1 = 1$ ,  $A_2 = 1$ , and  $\nu = 1$ .

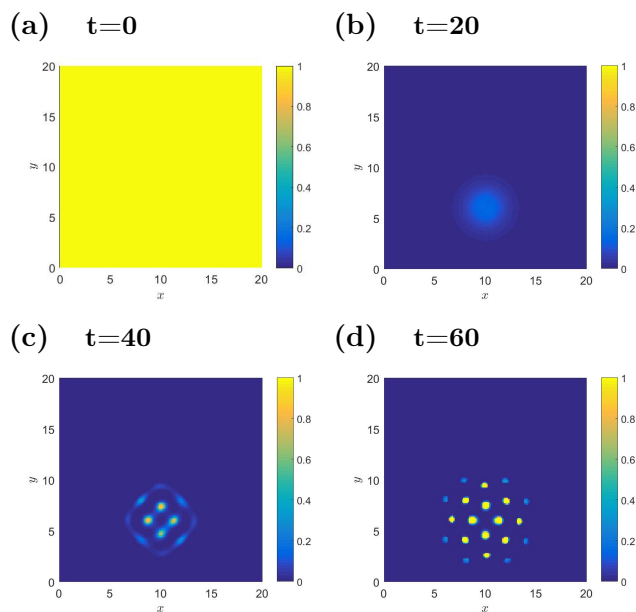


**Figure 4.19:** Two-dimensional Delta results with a VEGF function  $a(x) = \frac{1}{5}e^{-\frac{(x-10)^2}{5} - \frac{(y-6)^2}{5}}$  applied, with VEGF source at  $x = 10$  and  $y = 6$ , using the 2D rectangle weight function. Parameters are  $p = 3$ ,  $q = 3$ ,  $b = 0.1$ ,  $A_1 = 1$ ,  $A_2 = 1$ , and  $\nu = 1$ .

tionary spatial patterns for particular parameter values when inhomogeneous perturbations are applied. The perturbations were applied using random initial conditions for Notch receptor activity. The spatial patterns obtained reflect the behaviour expected of endothelial tissue activated for lateral inhibition when compared to both biological data and mathematical data from its discrete model equivalent.

The discrete model shows pattern formation from an array of identical cells. The continuous model gives the estimated levels of Delta and Notch at a point by averaging suitable neighbour functions for different shaped and sized cell layouts, so that unrealistic identical cell layouts are not assumed. The discrete model is more useful when components need to be tracked and the locations of individual cells need to be known; this can be particularly useful when components are in motion. However, the cells in this model are stationary and an estimated pattern of lateral inhibition is sufficient for coupling to an angiogenesis model.

For parameters which give unstable solutions to inhomogeneous perturbations, the discrete model gives an on-off pattern. The continuous model gives similar results for the rectangle function, but the “on” and “off” peaks are smoother, and give a larger wavelength. The behaviour varies also with the change of weight function; using the triangle weight function for example yields solutions with sharper peaks, which vaguely resembles the triangle function itself. The rectangle function appears to affect solutions in a similar way, with flatter troughs than both the triangle and Gaussian-derived weight function solutions.

For a ring of cells where each cell has exactly two neighbours, the discrete model has one possible neighbour function. There are a few continuous neighbour functions which could be considered the equivalent of the discrete function which gives options for the form of this continuous neighbour function, and choosing the most appropriate proved challenging. Rectangle weight functions that covered everywhere in neighbour cells were investigated, along with delta functions with weight in the centre of neighbour cells only. However, it may have been more accurate to have delta functions on the edges of the neighbour cells instead, as this is where juxtacrine signalling occurs in reality. The wavelength is generally larger for the continuous model, which is expected because of the change in the neighbour function and therefore in the dominant wavenumber  $k^*$  for  $\hat{w}(k^*) = \hat{w}_{\min}$ .

The two-dimensional model has extra choices for neighbour functions in the discrete model, as there are more options for the locations of the neighbour cells. The most used layouts include a square lattice with four neighbours, and a hexagonal lattice with six neighbours. The continuous version in two dimensions again assumes irregular cell distributions and averages the neighbour locations to get weight functions with cross sections that are the same as the weight functions used in one dimension. The two-dimensional modelling makes an important advantage of the continuous model apparent; it does not require a lattice and therefore does not end up being restricted by one. The resulting 2D solutions form peaks of high Delta levels laid out in a hexagonal pattern, similar to the results achieved by the discrete model when using a hexagonal lattice. This result is unsurprising, as a hexagonal lattice is the most efficient and most commonly seen pattern in nature [92]. It is also expected to be seen in angiogenesis, where tip endothelial cells emerge at

the spots with high Delta activity, at a reasonable and efficient distance from each other.

This continuous extension of Collier's model was developed with lateral inhibition in angiogenesis in mind; however, the model can easily be applied to many biological circumstances. Lateral inhibition occurs as a result of many cellular signalling systems, for example, the original focus of Collier's model was on embryonic nervous system development of the fruit fly *Drosophila melanogaster* [45]. It is also possible to use the model for longer-range signals, such as Webb and Owen's model which investigated intra-membrane diffusion [152], and Cohen et al. who modelled nonneighbour juxtacrine signalling, which occurs using thin antennae-like parts of a cell called filopodia [43]. The model could also be adjusted to represent mechanisms which feature a purely positive feedback loop, such as signalling for migration and proliferation of tissue during wound healing, the original motivation of the model by Owen and Sherratt, which the model in the next chapter is based on [117].

While this model provides a good starting point for modelling lateral inhibition, it is very basic and ignores many important features of the Notch signalling pathway, such as production of both receptors and ligands, and the absorbing of activated receptor-ligand complexes by the cell. The paper by Collier et al. in which the discrete model was published acknowledges the limitations of this model and that many biological factors are overlooked; in fact, the model is described in the paper as an adaptable framework, which can be easily extended to include some of these features mentioned [45]. The next chapter will introduce an existing extension of the discrete Collier model and derive its continuous version.

# Chapter 5

## An extended model of lateral inhibition

### 5.1 Introduction

The Delta-Notch model in Chapter 4 is a very basic model of lateral inhibition, where the ligand and receptor activity is described with only a reaction and decay term in each equation. It may be easier than other models with regards to coupling, but its simplicity overlooks many important aspects of Delta-Notch signalling.

This chapter examines another model of lateral inhibition with extensions that include some of these aspects. Section 5.2 introduces this new continuous model of lateral inhibition, which is based on a discrete model by Owen and Sherratt [117]. The link between this model and the model from Chapter 4 is also explained. Section 5.3 presents a stability analysis of the model and derives the instability conditions for which patterns will emerge. The extensions to the model make the stability analysis and the stability conditions

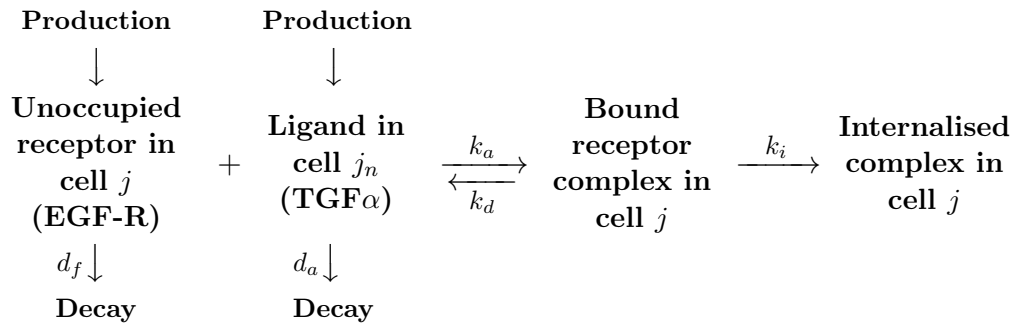


**Figure 5.1:** Relationships in the model of lateral inhibition (5.1) by Owen and Sherratt [117], where  $j_n$  represents a neighbour cell of cell  $j$ .

much more complex, giving many more options for the possible types of solutions obtained. Various results for different conditions are then presented in Section 5.4, and the conclusion of the chapter is given in Section 5.5.

## 5.2 The extended model

The model in Chapter 4 was a very simple case, which is clear when examining the relationship diagram Figure 4.2. A more detailed discrete model by Owen and Sherratt [117] on cell signalling in epidermal wound healing is based on the relationship diagram shown in Figure 5.1, where cell  $j_n$  is a neighbour cell to cell  $j$ .

Production rates of the receptors  $f$  and ligands  $a$  are influenced by the number of occupied receptors  $b$ . Internalisation is the absorption of the complex by the cell. The model, which includes entirely positive feedback between the ligand Transforming Growth Factor  $\alpha$  (TGF $\alpha$ ) and the receptor Epidermal Growth Factor Receptor (EGF-R), must be adjusted to reflect the lateral inhibition of Delta by Notch receptors. The mathematical equations for the

levels of unoccupied receptors  $f_j$ , ligands  $a_j$ , and occupied receptor complexes  $b_j$  for cell  $j$  are written:

$$\begin{aligned}\frac{\partial f_j}{\partial t} &= -k_a \bar{a}_j f_j + k_d b_j + P_f(b_j) - d_f f_j, \\ \frac{\partial a_j}{\partial t} &= -k_a \bar{f}_j a_j + k_d \bar{b}_j + P_a(b_j) - d_a a_j, \\ \frac{\partial b_j}{\partial t} &= k_a \bar{a}_j f_j - k_d b_j - k_i b_j,\end{aligned}\tag{5.1}$$

with binding, dissociation and internalisation rates defined as  $k_a$ ,  $k_d$  and  $k_i$  respectively, and ligand decay rate  $d_a$  and free receptor decay rate  $d_f$ . These parameters are all positive. The average value of variable  $u$  in a neighbour of cell  $j$  is again denoted by  $\bar{u}_j$ . The functions  $P_f(b_j)$  and  $P_a(b_j)$  are the production rates in cell  $j$  of the free receptor and the ligand respectively, and are defined as the Hill functions

$$P_a(x) = \frac{C_1 x^m}{C_2^m + x^m} \quad \text{and} \quad P_f(x) = C_3 + \frac{C_4 x^n}{C_5^n + x^n},\tag{5.2}$$

where positive power  $m$  or  $n$  represents activation, and negative power represents inhibition, of production by bound receptors. A production increase of free receptors and decrease of ligand in the presence of bound receptors are required for lateral inhibition, which is achieved with negative  $m$  and positive  $n$ . The continuous equations take the same form as (5.1) but the  $j$  subscripts are removed. As before, the continuous average will take the form

$$\bar{u}(x, t) = \int_{-\infty}^{\infty} w(s) u(x - s, t) ds,\tag{5.3}$$

with a suitable weight function  $w(s)$ .

### 5.2.1 Nondimensionalisation

The continuous version of this extended model will now be nondimensionalised. The variables  $f$ ,  $a$  and  $b$  represent receptor and ligand concentrations. The dimensions of these variables shall be denoted  $N$ , so that

$$\begin{aligned} [f] = [a] = [b] = N, \quad [k_a] = N^{-1}T^{-1}, \\ [k_d] = [k_i] = T^{-1}, \quad [d_a] = [d_f] = T^{-1}. \end{aligned}$$

Setting  $t^* = d_f t$ ,  $f^* = f k_a / d_f$ ,  $a^* = a k_a / d_f$ , and  $b^* = b k_a / d_f$ , and then removing asterisks derives the dimensionless equations

$$\begin{aligned} \frac{\partial f}{\partial t} &= -\bar{a}f + \mu b + p_f(b) - f, \\ \frac{\partial a}{\partial t} &= -a\bar{f} + \mu\bar{b} + p_a(b) - \delta a, \\ \frac{\partial b}{\partial t} &= \bar{a}f - \mu b - \lambda b, \end{aligned} \tag{5.4}$$

where

$$\delta = \frac{d_a}{d_f}, \quad \mu = \frac{k_d}{d_f}, \quad \lambda = \frac{k_i}{d_f}.$$

The new Hill functions  $p_a(b)$  and  $p_f(b)$  are defined as

$$p_a(b) = \frac{C_6 b^m}{C_7^m + b^m}, \quad \text{and} \quad p_f(b) = C_8 + \frac{C_9 b^n}{C_{10}^n + b^n}, \tag{5.5}$$

for

$$\begin{aligned} C_6 &= \frac{k_a}{d_f^2} C_1, \quad C_7 = \frac{k_a}{d_f} C_2, \quad C_8 = \frac{k_a}{d_f^2} C_3, \\ C_9 &= \frac{k_a}{d_f^2} C_4, \quad C_{10} = \frac{k_a}{d_f} C_5. \end{aligned}$$

## 5.2.2 Reduction of the extended model to the first model

The model (5.4) can be reduced to the Collier model (4.27) from Chapter 4 by making assumptions about the dynamics, as demonstrated by Webb and Owen [151]. This reduction is briefly shown here to highlight both the link between the models and the assumptions made by the Collier model. Recall the Collier equations from Chapter 4

$$\begin{aligned} \frac{\partial n}{\partial t} &= g_1(\bar{d}) - n, \\ \frac{\partial d}{\partial t} &= \nu(g_2(n) - d), \\ g_1(x) &= \frac{D_1 x^p}{(D_2)^p + x^p}, \quad g_2(x) = \frac{D_3 (D_4)^q}{(D_5)^q + x^q}, \end{aligned} \tag{5.6}$$

with the Hill functions and some parameters relabelled to avoid confusion. The extended model equations are now re-stated here:

$$\begin{aligned} \frac{\partial f}{\partial t} &= -\bar{a}f + \mu b + p_f(b) - f, \\ \frac{\partial a}{\partial t} &= -a\bar{f} + \mu\bar{b} + p_a(b) - \delta a, \\ \frac{\partial b}{\partial t} &= \bar{a}f - \mu b - \lambda b, \end{aligned} \tag{5.7}$$

Firstly, if it is assumed in (5.7) that the free and bound receptor total is always fixed at some constant, i.e.  $f + b = r_0$ , then the free receptor variable  $f$  can be eliminated from the model:

$$\begin{aligned} \frac{\partial b}{\partial t} &= \bar{a}(r_0 - b) - \mu b - \lambda b, \\ \frac{\partial a}{\partial t} &= -a(r_0 - \bar{b}) + \mu\bar{b} + p_a(b) - \delta a. \end{aligned} \tag{5.8}$$

Rearranging these equations, the model becomes

$$\begin{aligned}\frac{\partial b}{\partial t} &= (R(\bar{a}) - b)(\mu + \lambda + \bar{a}), \\ \frac{\partial a}{\partial t} &= \delta \left( -\frac{a(r_0 - \bar{b})}{\delta} + \frac{\mu \bar{b}}{\delta} + \frac{p_a(b)}{\delta} - a \right),\end{aligned}\tag{5.9}$$

where

$$R(\bar{a}) = \frac{\bar{a}r_0}{\mu + \lambda + \bar{a}}.\tag{5.10}$$

For  $p = 1$  in the Collier model, and for small binding and dissociation terms  $a(r_0 - \bar{b})$  and  $\mu \bar{b}$  compared to the production and decay terms  $p_a(b)$  and  $\delta a$ , the equations (5.9) can be written as

$$\begin{aligned}\frac{\partial b}{\partial t} &= (f(\bar{a}) - b)(D_2 + \bar{a}), \\ \frac{\partial a}{\partial t} &= \nu \left( \frac{p_a(b)}{\delta} - a \right),\end{aligned}\tag{5.11}$$

where parameters have been set as  $\delta = \nu$ ,  $r_0 = D_1$ ,  $\mu + \lambda = D_2$  and therefore  $R(\bar{a}) = g_1(\bar{a})$ . These equations (5.11) share the same homogeneous and inhomogeneous steady states with the equations (5.6).

The Collier model (5.6) assumes decrease in ligand creation when Notch is activated, as the Collier model is for Delta-Notch signalling specifically. The Owen model (5.4) is more general and allows for alternative reactions by changing parameters in the production rates of ligand and receptor  $p_a$  and  $p_f$ . Both of these models are able to simulate the cell signalling of angiogenesis.

### 5.3 Stability analysis

This section presents a stability analysis of the extended model (5.4). The steady states  $a_e, f_e, b_e$  for the model, where  $\bar{u} = u_e$ , give

$$\begin{aligned} a_e &= \frac{(\mu + \lambda)b_e}{f_e}, \\ p_a(b_e) &= \lambda b_e + \delta a_e, \\ p_f(b_e) &= \lambda b_e + f_e. \end{aligned} \tag{5.12}$$

Applying a small perturbation of the form  $\tilde{u}(x, t) = Ue^{\alpha t + ikx}$  to the base states of  $f$ ,  $a$  and  $b$  gives  $f(x, t) = f_e + \tilde{f}(x, t)$ ,  $a(x, t) = a_e + \tilde{a}(x, t)$ ,  $b(x, t) = b_e + \tilde{b}(x, t)$ , and the averages are of the form

$$\begin{aligned} \bar{u}(x, t) &= u_e + \tilde{u}(x, t) \int_{-\infty}^{\infty} w(s) e^{-iks} ds \\ &= u_e + \tilde{u}(x, t) \hat{w}(k), \end{aligned} \tag{5.13}$$

where  $\hat{w}(k)$  is the Fourier Transform of  $w(s)$ . The linearised versions of equations (5.4) are

$$\begin{aligned} (\alpha + a_e + 1)\tilde{f} + f_e \hat{w} \tilde{a} - (\mu + \mathcal{F})\tilde{b} &= 0, \\ a_e \hat{w} \tilde{f} + (\alpha + f_e + \delta)\tilde{a} - (\mu \hat{w} + \mathcal{A})\tilde{b} &= 0, \\ -a_e \tilde{f} - f_e \hat{w} \tilde{a} + (\alpha + \mu + \lambda)\tilde{b} &= 0, \end{aligned} \tag{5.14}$$

where  $\mathcal{A} = p'_a(b_e)$ ,  $\mathcal{F} = p'_f(b_e)$ .

Written as a matrix this is:

$$\begin{pmatrix} \alpha + a_e + 1 & f_e \hat{w} & -(\mu + \mathcal{F}) \\ a_e \hat{w} & \alpha + f_e + \delta & -(\mu \hat{w} + \mathcal{A}) \\ -a_e & -f_e \hat{w} & \alpha + \mu + \lambda \end{pmatrix} \begin{pmatrix} \tilde{f} \\ \tilde{a} \\ \tilde{b} \end{pmatrix} = 0, \quad (5.15)$$

giving characteristic equation

$$\alpha^3 + a_1 \alpha^2 + a_2(\hat{w}) \alpha + a_3(\hat{w}) = 0, \quad (5.16)$$

where

$$a_1 = f_e + a_e + 1 + \delta + \mu + \lambda,$$

$$a_2 = -\hat{w}^2 f_e (a_e + \mu) - \hat{w} f_e \mathcal{A} + \delta + (\delta + 1)(\mu + \lambda) + f_e (a_e + 1 + \mu + \lambda) + a_e (\delta + \lambda - \mathcal{F}),$$

$$a_3 = -\hat{w}^2 f_e (a_e (\lambda - \mathcal{F}) + \mu) - \hat{w} f_e \mathcal{A} + (f_e + \delta)(a_e (\lambda - \mathcal{F}) + \mu + \lambda).$$

A spatial pattern occurs only for steady states that are stable for homogeneous perturbations (where wavenumber  $k = 0$ , i.e.  $\hat{w} = \int_{-\infty}^{\infty} w(s) ds = 1$ ) and unstable for inhomogeneous perturbations. The steady state is stable when a perturbation is applied if the real parts of all three roots of the characteristic equation are negative.

Roots  $a$ ,  $b$ ,  $c$  to the above cubic equation define  $a_1 = -(a + b + c)$ ,  $a_2(\hat{w}) = ab + ac + bc$ , and  $a_3(\hat{w}) = -abc$ . If all roots have real negative part ( $a, b, c < 0$ ), the following is true:

$$a_1 > 0, \quad a_1 a_2(\hat{w}) - a_3(\hat{w}) > 0, \quad a_3(\hat{w}) > 0. \quad (5.17)$$

Some further analysis was undertaken and proved that these conditions are not only necessary when all roots have negative real part, but are also sufficient to ensure it. Note that the first condition  $a_1 > 0$  already holds for all  $k$ , as the parameters and steady states are positive. These stability criteria are now used to find solutions that are stable to homogeneous perturbations and unstable to inhomogeneous perturbations.

### 5.3.1 Solutions stable to homogeneous spatial perturbations

The last two stability criteria give a region of stability for homogeneous perturbations in the  $\mathcal{A} - \mathcal{F}$  plane, bounded by the lines

$$\begin{aligned} \mathbf{S}_1 : \mathcal{F} = & \lambda + \delta + \frac{f_e + \delta + (\delta + 1)(\mu + \lambda)}{a_e} \\ & + \frac{\delta^2(1 + \mu + \lambda) + \delta(f_e + \delta a_e) + \lambda f_e(a_1 - 1)}{a_e(a_1 - \delta)} \end{aligned} \quad (5.18)$$

$$\begin{aligned} & - \frac{f_e(a_1 - 1)}{a_e(a_1 - \delta)} \mathcal{A}, \\ \mathbf{S}_2 : \mathcal{F} = & \lambda + \frac{f_e \lambda}{\delta a_e} + \frac{\mu + \lambda}{a_e} - \frac{f_e}{\delta a_e} \mathcal{A}, \end{aligned} \quad (5.19)$$

where the region of stability is below both these lines. Both lines cross the  $\mathcal{F}$ -axis at positive  $\mathcal{F}$ , and they both have negative gradient determined by the decay rate ratio  $\delta$ , where for  $\delta < 1$  ( $d_f > d_a$ ),  $\frac{a_1 - 1}{a_1 - \delta} < 1$ , making line  $\mathbf{S}_1$  steeper than line  $\mathbf{S}_2$ . This is the opposite for  $\delta > 1$ . Furthermore, for  $\delta < 1$  the lines intersect at positive  $\mathcal{F}$  and for  $\delta > 1$  the lines intersect at positive  $\mathcal{A}$ . Therefore there are four different forms, two for each of  $\delta < 1$ ,  $\delta > 1$ , that the graph plotting both lines can take, as illustrated in Figure 5.2.

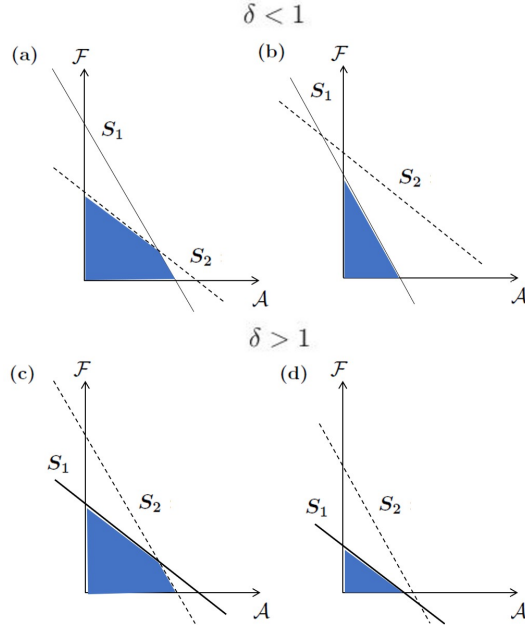


**Figure 5.2:** Graphs showing the four possible forms of the stability regions made from the two lines  $\mathcal{S}_1$  (5.18) and  $\mathcal{S}_2$  (5.19).

### 5.3.2 Solutions unstable to inhomogeneous spatial perturbations

The stable conditions found in Section 5.3.1 will now be assessed on their stability for inhomogeneous spatial perturbations. Patterning requires instability for inhomogeneous perturbations, i.e. for at least one of the three roots  $\alpha$  to have positive real part. Therefore at least one of the following must hold:

$$a_1 < 0, \quad a_1 a_2(\hat{w}) - a_3(\hat{w}) < 0, \quad a_3(\hat{w}) < 0. \quad (5.20)$$

$a_1$  is always positive so one of the other two conditions must be met instead. Consider weight functions  $w(s)$  for which the Fourier transform  $\hat{w}(k)$  lies between  $\kappa$  and 1, for some  $\kappa < 0$ . This is consistent with all the plausible weight functions discussed earlier in Section 4.3.2, where  $\hat{w}(\kappa) = \hat{w}_{\min}$ . Therefore

only solutions to one of the above inequalities for  $\kappa < \hat{w}(k) < 1$  need to be sought. The discrete model had  $\kappa = -1$ , which means the solutions for the continuous model, with  $-1 < \kappa < 0$ , will be different.

There are two cases where solutions are unstable to inhomogeneous perturbations; the case where  $a_1 a_2(\hat{w}) - a_3(\hat{w}) < 0$  shall be referred to as Case 1, and  $a_3(\hat{w}) < 0$  shall be called Case 2. Each case will now be considered separately.

**Case 1:**  $\sigma(\hat{w}) = a_1 a_2(\hat{w}) - a_3(\hat{w}) < 0$ .

$\sigma(\hat{w}) = a_1 a_2(\hat{w}) - a_3(\hat{w})$  is a quadratic function of  $\hat{w}$ . As all solutions are stable to homogeneous perturbations, it is known that  $\sigma(1) > 0$ . Considering the instance where the smallest value of  $\sigma(\hat{w})$  within  $[\kappa, 1)$  is  $\sigma(\hat{w}) = 0$  (when unstable solutions first emerge), the only possibilities for  $\sigma(\hat{w})$ , which are demonstrated in Figure 5.3, are where either the stationary point  $\hat{w}_{stat}$  of the quadratic function  $\sigma(\hat{w})$  is a minimum between  $\kappa$  and 1 (Figure 5.3(a)), a minimum outside  $[\kappa, 1)$  (Figure 5.3(b)), or it is a maximum (Figure 5.3(c)). Due to the stability condition  $\sigma(1) > 0$ , for each of the above possibilities there is no more than one root  $\hat{w}_{crit}$  (i.e.  $\sigma(\hat{w}_{crit}) = 0$ ) between  $\kappa$  and 1.

The possibilities make up two disjoint regions of the  $\mathcal{A} - \mathcal{F}$  plane, such that solutions where  $\sigma(\hat{w})$  has a minimum that lies in the interval  $[\kappa, 1)$  (Figure 5.3(a)) make up one region, which shall be called Region 1, and anything else (Figures 5.3(b), 5.3(c)) makes up the other region, Region 2:

**Region 1:**  $\sigma(\hat{w})$  has a minimum  $\hat{w}_{stat}$  that lies within  $[\kappa, 1)$ , so that

$$\sigma(\hat{w}_{crit} = \hat{w}_{stat}) = 0 \text{ at a repeated root.}$$

**Region 2:**  $\sigma(\hat{w})$  either has a minimum  $\hat{w}_{stat}$  that lies outside  $[\kappa, 1)$ , or it has a maximum, so that  $\sigma(\hat{w}_{crit} = \kappa) = 0$  at a single root in  $[\kappa, 1)$ .

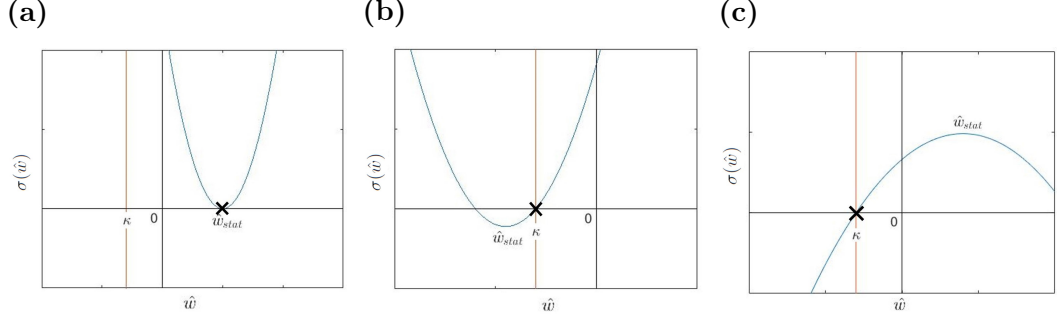


**Figure 5.3:** The possible forms of  $\sigma(\hat{w}) = a_1 a_2(\hat{w}) - a_3(\hat{w})$  in Case 1, in the instance where the smallest value of  $\sigma(\hat{w})$  in  $[\kappa, 1)$  is  $\sigma(\hat{w}) = 0$ . **(a)** Graphs where the stationary point is a minimum between  $\kappa$  and 1 make up Region 1, **(b)** graphs where the stationary point is a minimum outside  $\kappa$  and 1, or **(c)** where the stationary point is a maximum, make up Region 2. The critical point  $\hat{w}_{crit}$  where  $\sigma(\hat{w}_{crit}) = 0$  is marked with a cross on each graph.

Finding the conditions for  $\sigma(\hat{w}) = 0$  for each region finds the inequality conditions for instability; i.e. for  $\sigma(\hat{w}) < 0$ . There will be different conditions for each region.

The stationary point  $\hat{w}_{stat}$  of  $\sigma(\hat{w})$ , where  $\sigma'(\hat{w}_{stat}) = 0$ , is given by

$$\hat{w}_{stat} = -\frac{\mathcal{A}(a_1 - 1)}{2(a_e(a_1 + \mathcal{F} - \lambda) + \mu(a_1 - 1))}. \quad (5.21)$$

For Region 1, this point lies between  $\kappa$  and 1, and the quadratic coefficient  $-f_e(a_e(a_1 + \mathcal{F} - \lambda) + \mu(a_1 - 1))$  is positive. Region 1 is therefore defined by three inequalities:

$$\begin{aligned} \mathbf{R}_\kappa : \mathcal{F} &< \lambda - a_1 - \frac{(\mathcal{A} + 2\kappa\mu)(a_1 - 1)}{2\kappa a_e}, \\ \mathbf{R}_1 : \mathcal{F} &< \lambda - a_1 - \frac{(\mathcal{A} + 2\mu)(a_1 - 1)}{2a_e}, \\ \mathbf{R}_q : \mathcal{F} &< \lambda - a_1 - \frac{\mu(a_1 - 1)}{a_e}, \end{aligned}$$

where Region 2 is the opposite region. A change in stability in Region 1 occurs when  $\sigma(\hat{w}_{stat}) = 0$ . Solving this for  $\mathcal{F}$  after substituting in  $\hat{w}_{stat}$  yields

$$\mathbf{U}_{s_{\pm}} : \quad \mathcal{F} = \frac{-\beta_2 \pm \sqrt{\beta_2^2 - 4\beta_1\beta_3}}{2\beta_1},$$

where

$$\begin{aligned} \beta_1 &= -4a_e^2(a_e + 1 + \mu + \lambda), \\ \beta_2 &= 4a_e(a_e + 1 + \mu + \lambda)(f_e(a_1 + \delta) + a_e(\delta + 2\lambda - a_1) \\ &\quad - \mu(a_1 - 1) + (\delta + 1)(\delta + \lambda + \mu)), \\ \beta_3 &= 4(a_e(a_1 - \lambda) + \mu(a_1 - 1))(a_e + 1 + \mu + \lambda)(f_e(a_1 + \delta) \\ &\quad + a_e(\delta + \lambda) + (\delta + 1)(\delta + \lambda + \mu)) + f_e(a_1 - 1)^2\mathcal{A}^2. \end{aligned}$$

Region 2 has a change of stability at  $\sigma(\kappa) = 0$ , giving

$$\begin{aligned} \mathbf{U}_{\kappa} : \quad \mathcal{F} &= \delta + \lambda + \frac{(1 - \kappa^2)f_e(a_1 + \delta)}{f_e\kappa^2 + (a_e + 1 + \mu + \lambda)} \\ &\quad + \frac{(1 - \kappa^2)f_e\mu(a_1 - 1) + f_e(a_1 - \lambda)}{a_e(f_e\kappa^2 + (a_e + 1 + \mu + \lambda))} \\ &\quad + \frac{((\delta + 1)a_1 - \delta)(\mu + \lambda) + a_e\delta^2 + a_1(\delta + f_e\lambda)}{a_e(f_e\kappa^2 + (a_e + 1 + \mu + \lambda))} \\ &\quad - \frac{f_e\kappa(a_1 - 1)\mathcal{A}}{a_e(f_e\kappa^2 + (a_e + 1 + \mu + \lambda))}. \end{aligned}$$

Instability arises when  $\sigma(\hat{w}_{crit}) < 0$ ; this is when  $\mathbf{U}_{s_-} < \mathcal{F} < \mathbf{U}_{s_+}$  in Region 1, and  $\mathcal{F} > \mathbf{U}_{\kappa}$  in Region 2. The parts of these new unstable regions of Regions 1 and 2 that are also stable to homogeneous perturbations are denoted Region 1<sub>I</sub> and Region 2<sub>I</sub>.

**Case 2:**  $a_3(\hat{w}) < 0$ .

This case can be treated similarly to Case 1, as homogeneous stability again sets  $a_3(1) > 0$ , and  $a_3(\hat{w})$  is also a quadratic function. The stationary point of  $a_3(\hat{w})$  is at

$$\hat{w}_{stat} = -\frac{\mathcal{A}}{2(a_e(\lambda - \mathcal{F}) + \mu)}.$$

Similarly to Regions 1 and 2 for Case 1, Regions 3 and 4 of the  $\mathcal{A} - \mathcal{F}$  plane are described as

**Region 3:**  $a_3(\hat{w})$  has a minimum  $\hat{w}_{stat}$  that lies within  $[\kappa, 1)$ , so that  $a_3(\hat{w}_{crit} = \hat{w}_{stat}) = 0$  at a repeated root.

**Region 4:**  $a_3(\hat{w})$  either has a minimum  $\hat{w}_{stat}$  that lies outside  $[\kappa, 1)$ , or it has a maximum, so that

$$a_3(\hat{w}_{crit} = \kappa) = 0 \text{ at a single root in } [\kappa, 1).$$

In Region 3, the stationary point  $\hat{w}_{stat}$  of  $a_3(\hat{w})$  satisfies  $\hat{w}_{stat} \in [\kappa, 1)$ , and the quadratic coefficient  $f_e(a_e(\mathcal{F} - \lambda) - \mu) > 0$ . This gives Region 3 as

$$\begin{aligned} \mathbf{T}_\kappa : \quad \mathcal{F} &> \lambda + \frac{2\kappa\mu + \mathcal{A}}{2\kappa a_e}, \\ \mathbf{T}_1 : \quad \mathcal{F} &> \lambda + \frac{2\mu + \mathcal{A}}{2a_e}, \\ \mathbf{T}_q : \quad \mathcal{F} &> \lambda + \frac{\mu}{a_e}, \end{aligned}$$

and Region 4 is the opposite of Region 3. The change of stability in Region 3 occurs where  $a_3(\hat{w}_{stat}) = 0$ :

$$\mathbf{V}_{s\pm} : \quad \mathcal{F} = \lambda + \frac{1}{2a_e} \left( 2\mu + \lambda \pm \sqrt{\lambda^2 - \frac{f_e \mathcal{A}^2}{f_e + \delta}} \right),$$

and where  $a_3(\kappa) = 0$  for Region 4:

$$\mathbf{V}_\kappa: \quad \mathcal{F} = \lambda + \frac{f_e((1 - \kappa^2)\mu + \lambda) + \delta(\mu + \lambda)}{a_e((1 - \kappa^2)f_e + \delta)} - \frac{\kappa f_e \mathcal{A}}{a_e((1 - \kappa^2)f_e + \delta)}.$$

Instability occurs where either  $\mathcal{F} < \mathbf{V}_{s_-}$  or  $\mathcal{F} > \mathbf{V}_{s_+}$  in Region 3, and  $\mathcal{F} > \mathbf{V}_\kappa$  in Region 4. The regions in these which are also stable to homogeneous perturbations are called Region 3<sub>I</sub> and Region 4<sub>I</sub>.

To summarise, the four regions of the  $\mathcal{A} - \mathcal{F}$  plane where pattern formation can occur are:

$$\begin{aligned} \text{Region 1}_I: \quad & \mathcal{F} < \mathbf{S}_1, \quad \mathcal{F} < \mathbf{S}_2, \\ & \mathcal{F} < \mathbf{R}_\kappa, \quad \mathcal{F} < \mathbf{R}_1, \quad \mathcal{F} < \mathbf{R}_q, \quad (5.22) \\ & \mathbf{U}_{s_-} < \mathcal{F} < \mathbf{U}_{s_+}, \end{aligned}$$

$$\begin{aligned} \text{Region 2}_I: \quad & \mathcal{F} < \mathbf{S}_1, \quad \mathcal{F} < \mathbf{S}_2, \\ & \mathcal{F} > \mathbf{R}_\kappa \text{ OR } \mathcal{F} > \mathbf{R}_1 \text{ OR } \mathcal{F} > \mathbf{R}_q, \quad (5.23) \\ & \mathcal{F} > \mathbf{U}_\kappa, \end{aligned}$$

$$\begin{aligned} \text{Region 3}_I: \quad & \mathcal{F} < \mathbf{S}_1, \quad \mathcal{F} < \mathbf{S}_2, \\ & \mathcal{F} > \mathbf{T}_\kappa, \quad \mathcal{F} > \mathbf{T}_1, \quad \mathcal{F} > \mathbf{T}_q, \quad (5.24) \\ & \mathcal{F} < \mathbf{V}_{s_-} \text{ OR } \mathcal{F} > \mathbf{V}_{s_+}, \end{aligned}$$

$$\begin{aligned} \text{Region 4}_I: \quad & \mathcal{F} < \mathbf{S}_1, \quad \mathcal{F} < \mathbf{S}_2, \\ & \mathcal{F} < \mathbf{T}_\kappa \text{ OR } \mathcal{F} < \mathbf{T}_1 \text{ OR } \mathcal{F} < \mathbf{T}_q, \quad (5.25) \\ & \mathcal{F} > \mathbf{V}_\kappa. \end{aligned}$$

These regions with selected parameter values are illustrated in Figure 5.4.

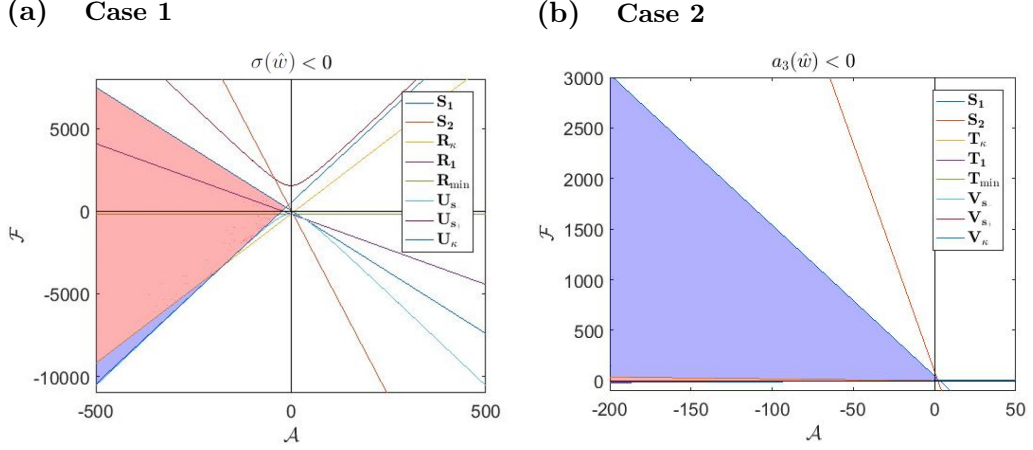


**Figure 5.4:** Plots of the stability conditions on the  $(\mathcal{A}, \mathcal{F})$  plane for parameter values  $\mu = 4$ ,  $\lambda = 2$ ,  $\delta = 1/3$ ,  $f_e = 90$ ,  $b_e = 90$ , and  $\kappa = -0.4726$ ; consistent with the triangle weight function. The shaded regions are the values of  $\mathcal{A}$  and  $\mathcal{F}$  for which patterns form; i.e. stability occurs for homogeneous spatial perturbations of a steady state and instability occurs for inhomogeneous perturbations. The four pattern-forming regions are shown: **(a)** Region  $1_I$  in blue, Region  $2_I$  in red, **(b)** Region  $3_I$  in blue and Region  $4_I$  in red.

### 5.3.3 Bifurcation analysis

A change of stability occurs when the real part of the growth rate  $\alpha$  passes through zero. Therefore, an insight into the types of bifurcations that occur is gained by setting  $\alpha = i\gamma$  so that  $\text{Re}(\alpha) = 0$  and substituting into the characteristic equation (5.16):

$$-i\gamma^3 - a_1\gamma^2 + a_2i\gamma + a_3 = 0. \quad (5.26)$$

Equating real and imaginary parts gives

$$\gamma^2 = \frac{a_3}{a_1}, \quad (5.27)$$

$$a_2 = \gamma^2 = \frac{a_3}{a_1}. \quad (5.28)$$

For  $\gamma \neq 0$  the imaginary part of  $\alpha$  exists, which means there is an oscillatory Hopf bifurcation here. There is a change of stability at  $a_1 a_2 - a_3 = 0$  which corresponds to the instability condition  $\sigma(\hat{w}) = a_1 a_2(\hat{w}) - a_3(\hat{w}) < 0$  in Case 1 above.

For  $\gamma = 0$  there is a change of stability at  $a_3 = 0$  and there is no imaginary part of  $\alpha$  here. This corresponds to Case 2 with instability condition  $a_3(\hat{w}) < 0$ , and the bifurcation is stationary.

It is also worth noting that for oscillatory solutions (i.e.  $\gamma \neq 0$ ),  $a_3 > 0$  is also required as  $\gamma^2 = a_3/a_1$  and  $a_1 > 0$  always. Therefore oscillatory solutions arise only where the instability condition is met in Case 1 and the stability condition is met in Case 2.

## 5.4 Simulation of the extended lateral inhibition model

### 5.4.1 Parameter values

Before running the simulations, the constants of the Hill functions  $p_a(b)$  and  $p_f(b)$  are set specific values to make navigation of the  $\mathcal{A} - \mathcal{F}$  plane easier, as suggested by Owen and Sherratt [117]. Recall the Hill functions given in equation (5.5) are

$$p_a(b) = \frac{C_6 b^m}{C_7^m + b^m}, \quad \text{and} \quad p_f(b) = C_8 + \frac{C_9 b^n}{C_{10}^n + b^n}, \quad (5.29)$$

with

$$\mathcal{A} = p'_a(b_e) = \frac{mb_e^{m-1}}{C_7^m + b_e^m}(C_6 - p_a(b_e)), \quad (5.30)$$

$$\text{and } \mathcal{F} = p'_f(b_e) = \frac{nb_e^{n-1}}{C_{10}^n + b_e^n}(C_9 - p_f(b_e) + C_8). \quad (5.31)$$

The last two steady states from (5.12) are

$$p_a(b_e) = \lambda b_e + \delta a_e, \quad p_f(b_e) = \lambda b_e + f_e,$$

which by substituting into (5.29) give

$$C_6 = (\lambda b_e + \delta a_e) \frac{C_7^m + b_e^m}{b_e^m}, \quad \text{and} \quad C_9 = (\lambda b_e + f_e - C_8) \frac{C_{10}^n + b_e^n}{b_e^n}. \quad (5.32)$$

In the absence of ligand, the number of bound receptors  $b = 0$ , and

$$p_f(0) = f_0, \quad (5.33)$$

where  $f_0$  is the regular number of free receptors when unstimulated by ligand.

With (5.29)<sub>2</sub>, this gives  $C_8 = f_0$ . Further, selecting  $C_7 = C_{10} = b_e$  sets (5.32)

as

$$C_6 = 2(\lambda b_e + \delta a_e), \quad C_9 = 2(\lambda b_e + f_e - f_0), \quad (5.34)$$

and  $\mathcal{A}$  and  $\mathcal{F}$  are now linear functions in terms of  $m$  and  $n$  of the form

$$\mathcal{A} = p'_a(b_e) = \frac{m(\lambda b_e + \delta a_e)}{2b_e} \quad \text{and} \quad \mathcal{F} = p'_f(b_e) = \frac{n(\lambda b_e + f_e - f_0)}{2b_e}. \quad (5.35)$$

Experimental data taken from Waters et al. [148], Oberg et al. [110] and Pandiella and Massague [120] (along with parameters used by Owen and Sher-

ratt [117]) suggests the following parameter values:

$$\begin{aligned} k_a &= 0.0003 \text{ molecule}^{-1}\text{min}^{-1}, & k_d &= 0.12 \text{ min}^{-1}, & k_i &= 0.019 \text{ min}^{-1}, \\ d_a &= 0.01 \text{ min}^{-1}, & d_f &= 0.03 \text{ min}^{-1}, \\ f_e &= 3000, & b_e &= 3000, & f_0 &= 3000, & a_e &= \frac{k_d + k_i}{k_a} = \frac{1390}{3}, \end{aligned}$$

recalling that  $f_e$ ,  $b_e$ ,  $a_e$  represent the steady states of the numbers of free receptors, bound receptors, and ligands. The lower number of ligands is caused by the lower production rate of ligand compared to the production rate of free receptors, which results in higher numbers of free receptors in neighbouring tissue and so ligands are constantly being bound. Using some of this data where appropriate, the parameters of the dimensionless model (5.4) are set as

$$\begin{aligned} \mu &= 4, & \lambda &= 2, & \delta &= \frac{1}{3}, \\ f_e &= 90, & b_e &= 90, & f_0 &= 90, & a_e &= \mu + \lambda = 6, \end{aligned}$$

for all numerical simulations in this chapter, so that the stability of all solutions are determined by the powers of the Hill functions ( $m$  and  $n$ ) only.

## 5.4.2 Numerical Simulation

The numerical simulation of this extended model of lateral inhibition is similar to the simulation of the first model performed in Section 4.5. The extended model also uses a fourth-order Runge-Kutta scheme; however this time all three variables  $f$ ,  $a$  and  $b$  are used in a spatial average function at some point in the model. Therefore, any spatial element of the simulation must take into account all three variables. For example, the periodic boundary conditions that all simulations in this chapter use must set  $f(L+h, t) = f(0, t)$ ,

$a(L + h, t) = a(0, t)$ ,  $b(L + h, t) = b(0, t)$ , for domain size  $L$  and mesh size  $h$ . The initial conditions here are set at or near the steady states:

$$f(x, 0) = f_e - \mathfrak{r}(x), \quad a(x, 0) = a_e, \quad b(x, 0) = b_e, \quad (5.36)$$

where for each  $x$ ,  $\mathfrak{r}(x)$  is a random number between 0 and 0.1.

All simulations presented in this chapter use the triangle weight function for the average neighbour function. The results of the continuous extended model of lateral inhibition show similarities to results of the simpler model from Chapter 4; however, the stability analysis this time yielded more stability conditions, each of which behaves differently. The brief bifurcation analysis in Section 5.3.3 shows that oscillatory-type patterns are expected for Regions  $1_I$  and  $2_I$ , and stationary patterns are expected in Regions  $3_I$  and  $4_I$ . Numerical results were obtained for Regions  $2_I$ ,  $3_I$ , and  $4_I$ , with Region  $1_I$  unable to produce pattern-forming solutions for suitable parameters, as shown by Figure 5.4. A particular stationary pattern observed in Region  $4_I$ , shown in Figure 5.5, is the most similar to the behaviour seen in the first model. This pattern emerges the same way as the pattern from the first model; the perturbation grows and forms a wave; however, after the solution reaches a particular amplitude, the edges of the wave peaks continue to rise without the middle of the wave peak and form spikes for the ligand and free receptor solutions, but not for the bound receptor solutions. The free  $f$  and bound  $b$  receptor solutions have the opposite pattern to the ligand  $a$  solutions, but much higher values, as shown in Figure 5.6.

The spikes in the solutions are likely caused by the conflicting terms in the model, in particular the equation for  $f$ . When binding first occurs and the number of bound receptors  $b$  starts to rise, this causes the number of free

receptors,  $f$ , to fall slightly at the same time as the free receptors become bound (from the binding term  $-\bar{a}f$ ). Once receptors are bound, they induce production of free receptors, so the number of free receptors starts to rise again (from the production term  $p_f(b)$ ). This causes a high number of free receptors where there is a high number of bound receptors, but the number of free receptors is not as high as it would be without the binding term. This behaviour presumably occurs in the discrete model as well, although this hasn't been proven. The wave peaks have a dip in the middle as a result, where the effect of the binding term is larger and there are actually higher levels of free receptors on the peak edges, where there are slightly lower levels of bound receptors.

Stationary patterns were also observed in Region  $3_I$ . This pattern is similar to patterns in Region  $4_I$  except the pattern undergoes a type of amplitude modulation where the actual amplitude is maintained, but the peak and trough values vary across space, as depicted in Figure 5.7(a). Figure 5.7(b) shows a solution in Region  $4_I$  that is closer to stability, which has a regular sinusoidal-type wave with the amplitude decreasing as the solution approaches stability, in agreement with the first model results in Chapter 4.

Given that pattern-forming solutions were not obtained for Region  $1_I$ , the only oscillatory solutions obtained were in Region  $2_I$ . A simulation in this region shows evidence of a Hopf bifurcation; the wave first oscillates around the base state  $a_e$  as it grows in amplitude, and as it approaches the limit cycle at its maximum amplitude it stops oscillating and becomes a travelling wave. A pseudocolor plot of this solution over space and time is shown in Figure 5.8. As expected from the bifurcation analysis, instability for inhomogeneous

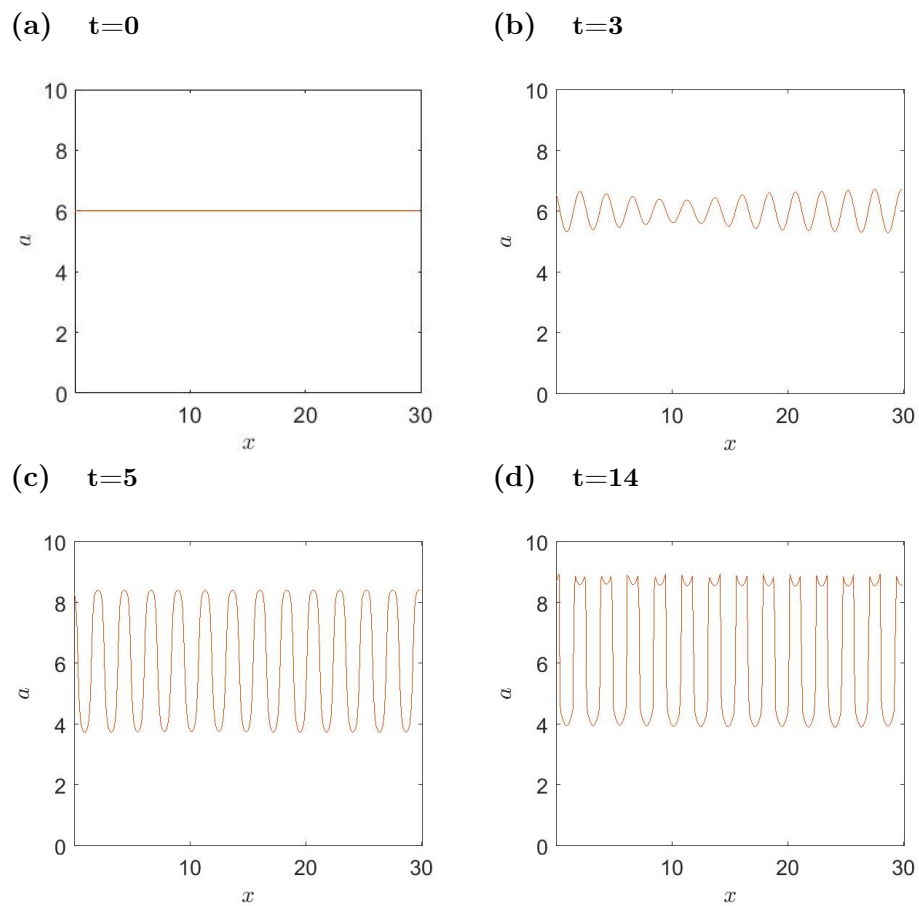


**Figure 5.5:** Results for the ligand  $a$  of the numerical simulation of the extended lateral inhibition model within Region  $4_1$ , for (a)  $t=0$ , (b)  $t=3$ , (c)  $t=5$  and (d)  $t=14$ , over a domain of 30 average cell lengths and with periodic boundary conditions. This and all other simulations use the triangle weight function. The powers of the Hill functions are set as  $m = -20$ ,  $n = 3$ .

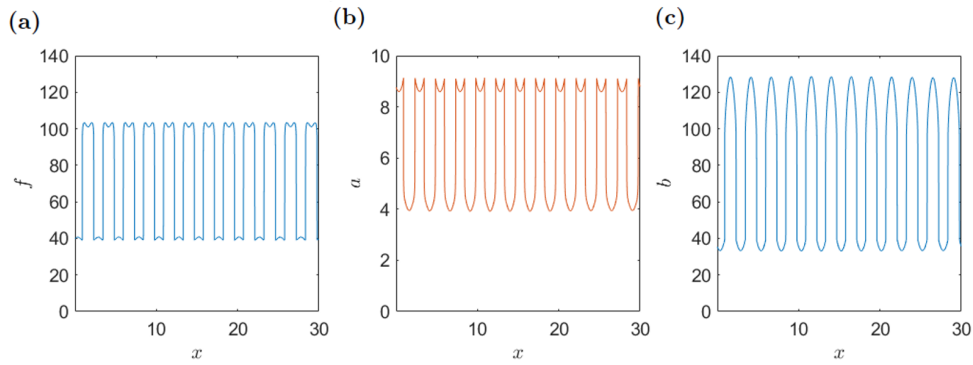


**Figure 5.6:** Final patterns of a simulation in Region  $4_I$  with periodic boundary conditions and  $m = -20$ ,  $n = 3$ , for (a) free receptor  $f$ , (b) ligand  $a$ , and (c) bound receptor  $b$ .

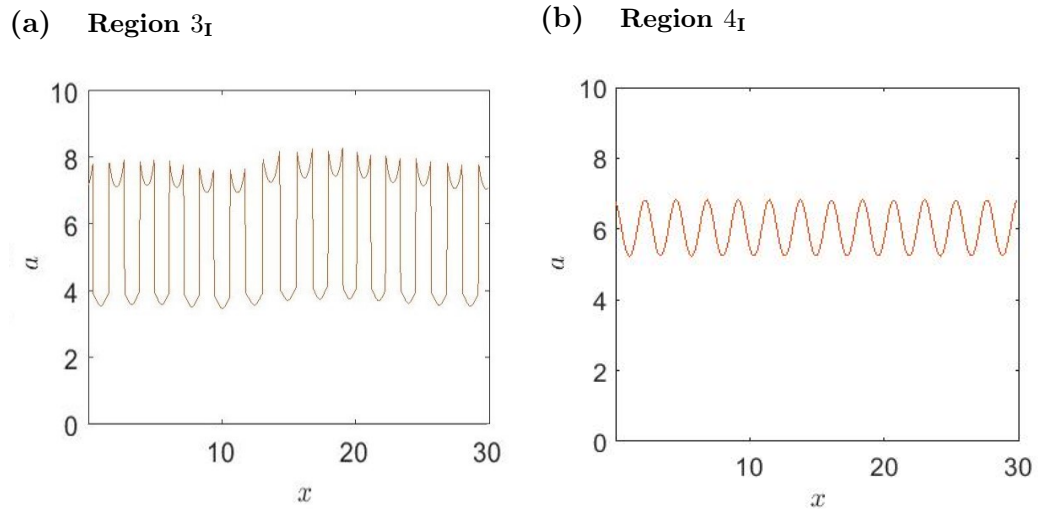


**Figure 5.7:** (a) Dominant pattern for ligand  $a$  in Region  $3_I$  at  $m = -20$ ,  $n = 7$ . There appears to be some underlying, larger wavelength related to the amplitude of the main pattern. (b) Pattern for ligand  $a$  in Region  $4_I$  close to stability with  $m = -20$ ,  $n = 1.1$ , which has the form of a sinusoidal wave.

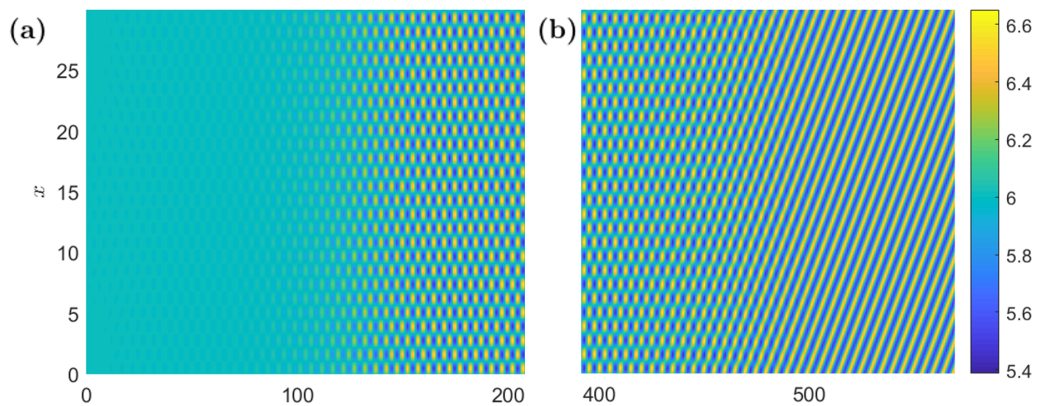


**Figure 5.8:** Region  $2_I$  results of oscillatory solutions at different times for ligand  $a$ , for parameter values  $m = -24, n = 0.2$ , for a domain of 30 cells and times  $0 < t < 569$ . **(a)** The wave grows and oscillates around its base state  $a_e = 6$ . **(b)** As the solution approaches its limit cycle at around  $t = 400$ , the wave begins to travel in space; the direction depends on the random initial condition. Once the stable limit cycle is reached, the wave continues to travel at a constant speed (from  $t = 500$ ).

perturbations in Region 3 or 4 as well as in Region 2 (i.e. where Regions  $2_I$  and  $3_I$ , or  $2_I$  and  $4_I$  overlap) produces a stationary pattern similar to patterns observed in Regions  $3_I$  and  $4_I$ .

Figure 5.9 is a bifurcation diagram for Region 4, obtained by finding the maximum and minimum values of ligand  $a$  for different values of the parameter  $n$  once a stable final solution is reached. The diagram suggests a supercritical pitchfork bifurcation.

Just as in the first model, this model can also set parameters as spatial functions to restrict the formation of a pattern, just like the growth of blood vessels when exposed to VEGF in only one area. For the localised results shown in Figure 5.10, parameters can be set using bifurcation diagram Figure 5.9;  $m = -20$  sets the region as Region  $4_I$  and a spatially dependent function for

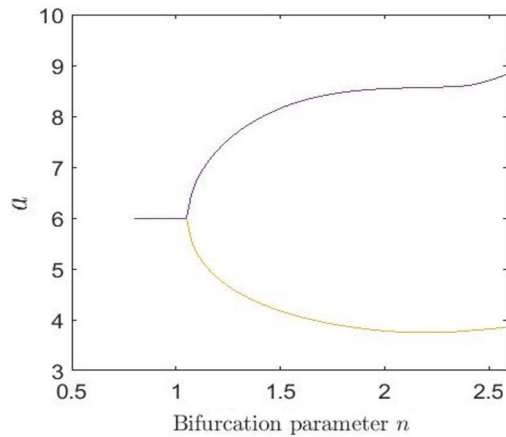


**Figure 5.9:** A bifurcation diagram of results from Region 4 showing the minimum and maximum values of ligand  $a$  once a stable final solution is reached, for different values of bifurcation parameter  $n$ , with  $m = -20$ .

$n$  determines the stability for each position. The VEGF function  $n(x)$  is set in Figure 5.10 as

$$n(x) = 3e^{-\frac{(x-10)^2}{5}}. \quad (5.37)$$

The result is similar to the earlier model from Chapter 4; the stable and unstable areas are still clear, and the perturbation does not grow in the stable areas. However, the peaks with the largest amplitude have spikes on their edges, as seen earlier in Figure 5.5.

## 5.5 Conclusion

The extension of the Collier model that was developed by Owen and Sherratt [117] considered additional and important factors such as production rates of ligand and receptors, and internalisation of active receptors. The Collier model only included the minimum information necessary for a juxtacrine signalling system; the neighbour feedback terms and the decay terms. The Owen

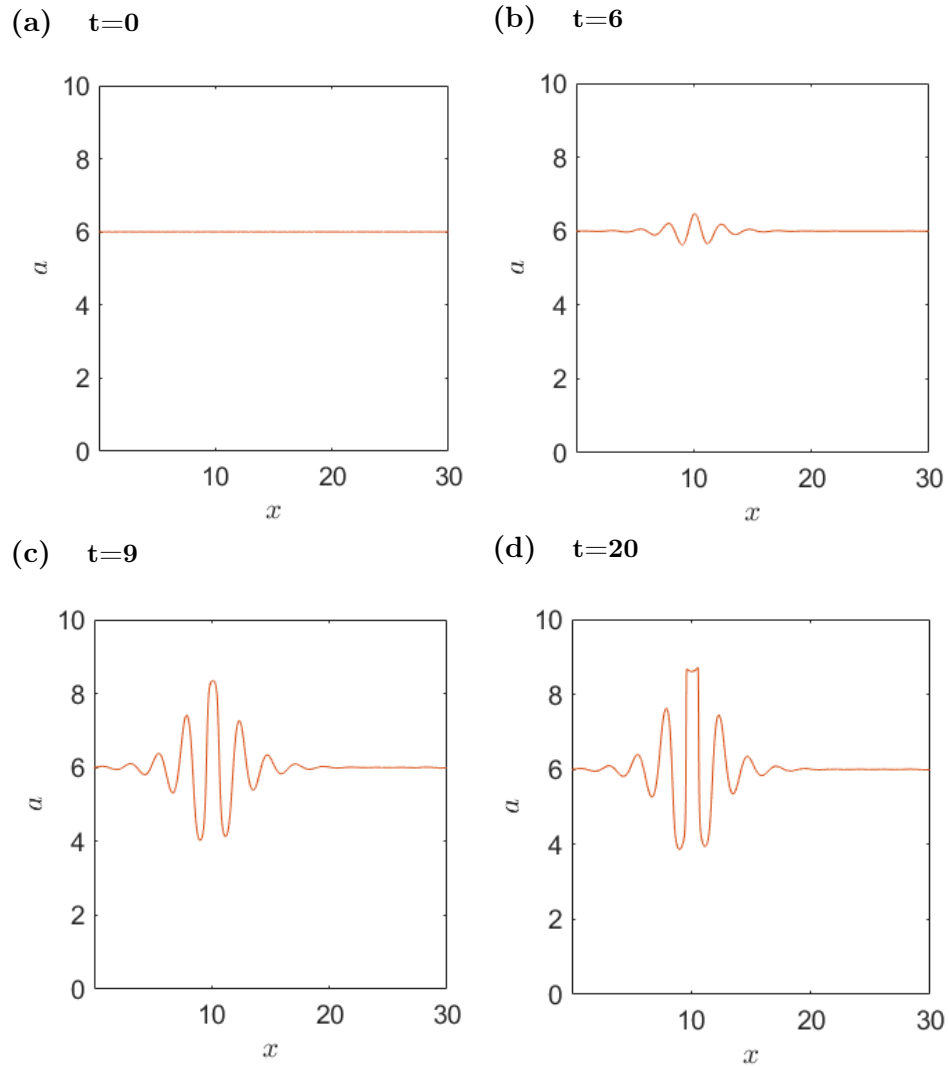


**Figure 5.10:** The pattern of ligand activity in Region  $4_I$  with localised stability as expected when only a small area of endothelium in blood vessels are exposed to angiogenic factor, at times (a)  $t=0$ , (b)  $t=6$ , (c)  $t=9$ , (d)  $t=20$ . The VEGF function is set as  $n(x) = 3e^{-\frac{(x-10)^2}{5}}$ , for VEGF source at  $x = 10$ .

model also considered free and bounded receptors separately, and therefore had more in-depth neighbour interaction terms than the Collier model, which only defined bound receptors by assuming there is a fixed number of total receptors and no new receptors are produced. “Production” of  $n$  in the Collier model is in fact binding of Notch receptors. Although the model was originally used by Owen and Sherratt to model signalling used in wound healing with a purely positive feedback loop, the effect of bound receptors on ligand production levels was set as negative in the continuous model (5.4) by choosing the production function of Delta,  $P_a(b)$ , to be a decreasing Hill function to achieve results which simulate lateral inhibition. The added detail of this extended model meant there were multiple stability conditions which produced several regions of stability, each with different behaviours.

The stationary patterns from Regions  $3_I$  and  $4_I$  were the most similar to the patterns of the earlier continuous Delta-Notch model from Chapter 4. The results show alternating high and low ligand level areas, with both the free and bound receptor results taking high values at low ligand levels as bound receptors have a positive influence on the production of free receptors. However, when a large enough amplitude is reached, the ligand and free receptor results form spikes on the edges of each peak. Changes to the mesh size proved that a coarse mesh was not the cause. Consideration of the model mechanics suggested that the conflicting terms causing both increase and decrease of free receptor levels at the same location could be the culprit.

Solutions which emerge from other instability regions do not reflect the behaviour expected of a cell signalling system. Oscillatory solutions are found in Regions  $1_I$  and  $2_I$ ; although only solutions in Region  $2_I$  were obtained. The

behaviour of Region  $1_I$  could be vastly different from Region  $2_I$ , especially considering the reason results could not be found for Region  $1_I$  was because of the extreme parameter values required. However, it is still known that these oscillatory results, whether they feature a travelling wave or an oscillating standing wave, are not biologically feasible as a representation of Notch signalling.

The model still overlooks some important biological factors, namely those related to the intracellular kinetics, such as the transcription and translation times of ligand and receptor proteins, and also of internalised ligand-receptor complexes. An extended version of this work could investigate these delays caused by gene expression and their effect on the final solutions. Such models which incorporate delay terms have been studied by Veflingstad et al. [142] and Momiji and Monk [104], which were studied when the authors noticed a lack of delays in existing lateral inhibition models. These models found additional homogeneous oscillations emerge before a stationary steady state is reached. Another potential extension to this model could be to consider the behaviour and distribution of ligands and receptors on the cell membrane, as this model currently assumes a homogeneous distribution of ligands and receptors, where each cell is affected by exactly half of the ligands and receptors of each neighbour cell. This is unlikely when considering irregular cell distributions, as is the aim of this work. Webb and Owen derived a discrete model which tracked receptor and ligand levels on individual membrane sections of individual cells [152]. This would be difficult to implement into a continuous model, but the membrane could at least be split into the left and right sides of the cell, with the left side only interacting with the right side of the left cell and the right side interacting with the left side of the right cell.

An important issue in the cell signalling models which must be addressed is the distinction between active and inactive/inhibited areas. The importance of this distinction will become clearer later in Chapter 8 when a continuous lateral inhibition model is coupled to a model of angiogenesis and the endothelial tissue needs to be defined as either activated or not activated for migration. As Wearing et al. [150] indicated, the discrete model solutions show ligand and receptor levels which mostly take one of two values; the cell either has a high level of Delta and is activated, or has a lower level of Delta and is inhibited. The activation/inhibition grouping in the continuous models are less clear; when the pattern switches from high Delta to low Delta over space a continuum pattern will have a changeover period where there will be medium Delta levels near the homogeneous steady state. However, imposing a threshold on the Delta levels in the angiogenesis model where meeting this threshold promotes migration of endothelial tissue will distinguish active from inactive endothelial tissue. The migration rate could increase as the Delta levels rise, as observed in vivo.

These continuous lateral inhibition models introduced in Chapters 4 and 5 can be used in a model of angiogenesis to control the onset of angiogenesis and also to control the branching along new capillaries. Using this method for new capillary selection will mean the angiogenesis model will not be as restrictive with regards to cell sizes and locations. However, the cell signalling occurs along the moving capillary surface the whole time during angiogenesis, and the models developed in these chapters only simulated the cell signalling in Cartesian coordinates. The next part of this work will simulate a continuous model of lateral inhibition on a surface.

# Chapter 6

## Modelling lateral inhibition on a surface

### 6.1 Introduction

The continuous Delta-Notch model formulated in Chapter 4 was simulated on both one-dimensional and two-dimensional domains. The main objective of this thesis is to use a Delta-Notch model to simulate the lateral inhibition signalling between endothelial cells along a capillary surface that is undergoing angiogenesis. Therefore, to be able to couple this model with an angiogenesis model, it must be able to be simulated on a moving surface. The method used to simulate the model uses phase field theory so that the surface approximation can be applied easily to the phase field angiogenesis model that will be used. Motivation for choosing a phase field model for angiogenesis will be discussed later in Chapter 7.

There are other methods for defining PDEs on surfaces, such as the method defined by Bertalmío et al. [16] which uses a level set to define the surface,

and can make the computation easier by performing all calculations within a narrow band around the surface. Another technique involves mapping solutions on a line to the surface. While some of these methods will also be suitable, in this case none will be as easily applied as the phase field approximation method, and may be complicated to implement in an angiogenesis model which will already have the complication of two coupled models.

The method used here is called a phase field approximation method, suggested by Ratz and Voight [125], which defines the Delta-Notch model over the whole domain and uses a spatial function that takes the value of zero everywhere except on and near the blood vessel interface to approximate the model on this interface. This diffuse interface method is ideal for when the interface is not known analytically and is defined using a so-called phase field parameter or order parameter.

In this chapter, Section 6.2 will briefly recall the idea of phase field modelling already covered in Chapter 3, Section 3.4, although more detail is given later in Chapter 7, when the phase field angiogenesis model is presented. Section 6.3 describes the phase field approximation method and performs an asymptotic analysis on such an approximation of a set of simple reaction-diffusion equations, to demonstrate that the approximation reduces to the exact original equations when the interface parameter  $\epsilon$  approaches zero. A similar surface approximation and asymptotic analysis of the continuous Delta-Notch model from Chapter 4 is then given. The numerical results of this surface Delta-Notch model on a variety of surfaces are shown in Section 6.4, and some concluding remarks are presented in Section 6.5.

## 6.2 Phase field modelling

Many physical systems have two or more phases, separated by an interface between the phases. It is this transition between phases which can be difficult to simulate numerically, especially if the transition is sudden. One way to simulate this is to instead represent the interface between phases as a smooth interface, which changes from one phase to another gradually rather than suddenly. The interface is prescribed a particular thickness, often represented with the parameter  $\epsilon$ .

Models involving phases sometimes use a parameter to define the phases. In this chapter, the parameter  $\phi$  will be known as the phase field or order parameter, and holds a particular value in each of the phases. Recall Figure 3.1 in Chapter 3, where an example of a phase field parameter was given for both sharp and diffuse interfaces.

In this chapter the phase field parameter will be  $\phi = 0$  outside the surface and  $\phi = 1$  inside. A tanh function is a common choice for a phase field parameter. Here,  $\phi$  will take the form

$$\phi(\mathbf{x}) = \varphi\left(\frac{r}{\epsilon}\right) = \frac{1}{2} \left( 1 - \tanh\left(\frac{s(\mathbf{x})}{\epsilon}\right) \right), \quad (6.1)$$

where  $\epsilon$  is proportional to the interface thickness, and  $r$  is the distance of  $x$  from the surface, with  $r$  positive outside the surface and negative inside.  $s(\mathbf{x}) = 0$  is the equation of the surface, e.g. for a unit circle,  $s(\mathbf{x}) = x^2 + y^2 - 1 = 0$ .  $\phi$  is a decreasing function of  $s(\mathbf{x})$ , and the graph of  $\phi(s(\mathbf{x}))$  is given in Figure 6.1.

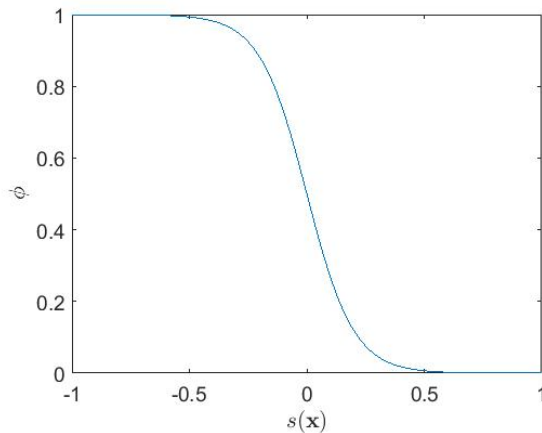


**Figure 6.1:** The order parameter  $\phi(s(\mathbf{x}))$ , given by equation (6.1), with  $\phi = 0$  outside the surface  $s(\mathbf{x}) = 0$  and  $\phi = 1$  inside the surface, for  $\epsilon = 0.2$ .

### 6.3 The phase field approximation method

The details of the phase field approximation method by Ratz and Voigt [125] are described in this section. A function  $B(\phi)$  is introduced, which has the following form:

$$B(\phi) = \phi^2(1 - \phi)^2, \quad (6.2)$$

which sets  $B = 0$  everywhere except on the surface (i.e.  $B(\phi = 0) = 0$ ,  $B(\phi = 1) = 0$ ,  $B(\phi = \frac{1}{2}) = \frac{1}{16}$ ).  $B(\phi)$  can be altered depending on the values of  $\phi$  in the different phases, for example, for phases at  $\phi = 1$  and  $\phi = -1$  instead, set

$$B(\phi) = (\phi + 1)^2(\phi - 1)^2. \quad (6.3)$$

The inclusion of this function  $B(\phi)$  ensures that the equations are only defined on the given interface. The graph (6.2) of  $B(\phi(\mathbf{x}))$ , both in terms of  $\phi$  and in terms of  $s(\mathbf{x})$ , is given in Figure 6.2.

A matched asymptotic analysis of a phase field approximation, first demon-

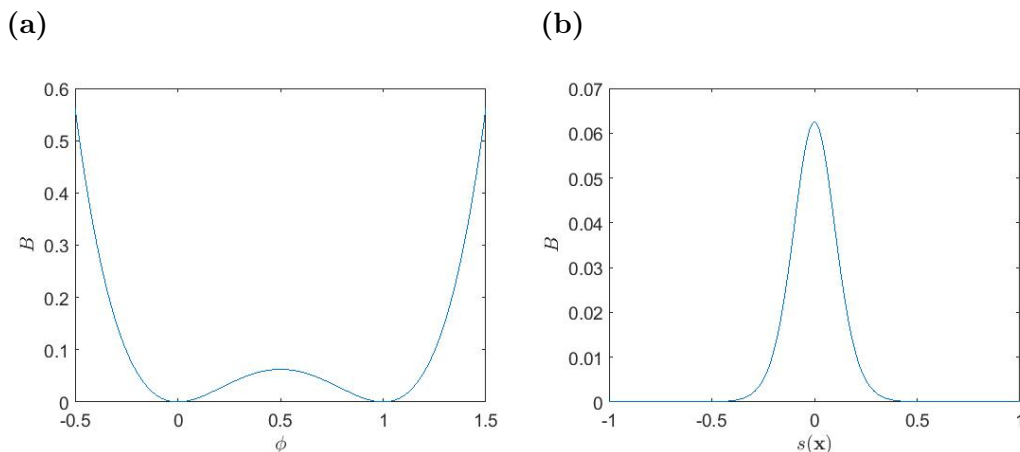


**Figure 6.2:** The graphs of  $B(\phi(s(\mathbf{x}))) = \phi^2(1 - \phi)^2$ , for  $\epsilon = 0.2$ , in terms of **(a)**  $\phi$ , where  $B = 0$  in phases  $\phi = 0$ ,  $\phi = 1$ , and **(b)**  $s(\mathbf{x})$ , where  $B = 0$  everywhere except at and near the interface  $s(\mathbf{x}) = 0$ . Note that as  $\epsilon \rightarrow 0$ ,  $B(s(\mathbf{x}))$  will become a delta function, with a non-zero value at  $s(\mathbf{x}) = 0$  only.

strated by Fife [60] and Caginalp [35], is conducted when the suitability of the approximation must be demonstrated. The aim is to show that the phase field approximation of the lateral inhibition model across the whole domain reduces to the original model on the surface as  $\epsilon \rightarrow 0$ . To introduce the procedure of the matched asymptotic analysis, the first example will be a simple reaction-diffusion model.

### 6.3.1 Reaction-diffusion equations

The general form of a reaction diffusion system is

$$\begin{aligned} \frac{\partial u}{\partial t} &= \nabla_{\Gamma}^2 u + f(u, v) && \text{on } \Gamma, \\ \frac{\partial v}{\partial t} &= D \nabla_{\Gamma}^2 v + g(u, v) && \text{on } \Gamma, \end{aligned} \tag{6.4}$$

with chemical concentrations  $u, v$ , reaction terms  $f(u, v), g(u, v)$ , and diffusion coefficient  $D$ . The phase field approximation is then given as

$$\begin{aligned} B(\phi) \frac{\partial \tilde{u}}{\partial t} &= \nabla \cdot ((\delta(\epsilon) + B(\phi)) \nabla \tilde{u}) + B(\phi) f(\tilde{u}, \tilde{v}) && \text{on } \Omega, \\ B(\phi) \frac{\partial \tilde{v}}{\partial t} &= D \nabla \cdot ((\delta(\epsilon) + B(\phi)) \nabla \tilde{v}) + B(\phi) g(\tilde{u}, \tilde{v}) && \text{on } \Omega, \end{aligned} \quad (6.5)$$

where the presence of the parameter  $\delta$  in the first term on the right-hand side ensures dissipation of the variables away from the interface, but is negligible nearer the interface as  $\delta(\epsilon) \ll \epsilon$ . The first step in the matched asymptotic analysis is to redefine variables in a new coordinate system which represent the directions tangent and normal to the interface  $\Gamma$ :

$$\mathbf{x} = \mathbf{X}(s, \epsilon) + r(x, \epsilon) \mathbf{n}(s, \epsilon), \quad (6.6)$$

where  $\mathbf{X} : S \rightarrow \mathbb{R}$  represents the surface for  $s \in S$ ,  $\mathbf{n}(s, \epsilon)$  is the unit normal to the surface and  $r$  is the normal component of the location  $x$ . Variables  $u(\mathbf{x}, t, \epsilon)$ ,  $v(\mathbf{x}, t, \epsilon)$  and  $\phi(\mathbf{x}, \epsilon)$  are redefined as

$$\hat{u}(r, s, t, \epsilon) = u(\mathbf{x}, t, \epsilon) = u(\mathbf{X} + r\mathbf{n}, t, \epsilon), \quad (6.7)$$

$$\hat{v}(r, s, t, \epsilon) = v(\mathbf{x}, t, \epsilon) = v(\mathbf{X} + r\mathbf{n}, t, \epsilon), \quad (6.8)$$

$$\hat{\phi}(r, s, \epsilon) = \phi(\mathbf{x}) = \phi(\mathbf{X} + r\mathbf{n}) = \varphi\left(\frac{r}{\epsilon}\right). \quad (6.9)$$

Define the stretched variable  $z = \frac{r}{\epsilon}$  to be able to focus on the diffuse interface. For the purposes of the matched asymptotic expansions, the diffuse interface

is labelled here as the “inner boundary layer”. Using this new variable  $z$ :

$$U(z, s, t, \epsilon) = \hat{u}(r, s, t, \epsilon), \quad (6.10)$$

$$V(z, s, t, \epsilon) = \hat{v}(r, s, t, \epsilon), \quad (6.11)$$

$$\Phi(z, s, \epsilon) = \hat{\phi}(r, s, \epsilon) = \varphi(z), \quad (6.12)$$

and the derivatives must also be rewritten in the new coordinates:

$$\begin{aligned} \nabla u &= \nabla_{\Gamma} U + \frac{\partial U}{\partial r} \mathbf{n} \\ &= \nabla_{\Gamma} U + \epsilon^{-1} \partial_z U \mathbf{n}, \end{aligned} \quad (6.13)$$

$$\begin{aligned} \nabla^2 u &= \nabla \cdot (\nabla_{\Gamma} U + \epsilon^{-1} \partial_z U \mathbf{n}) \\ &= \nabla_{\Gamma}^2 U + \frac{\partial}{\partial r} (\epsilon^{-1} \partial_z U) + \epsilon^{-1} (\nabla \cdot \mathbf{n}) \partial_z U \\ &= \nabla_{\Gamma}^2 U + \epsilon^{-2} \partial_z^2 U + \epsilon^{-1} \kappa \partial_z U, \end{aligned} \quad (6.14)$$

with a similar definition for  $\nabla v$ ,  $\nabla^2 v$ .  $\kappa = \nabla \cdot \mathbf{n}$  is the mean curvature (i.e. the sum of the principal curvatures) of  $\Gamma$ . Using the Laplacian (6.14) above, and assuming that  $\delta(\epsilon) \ll \epsilon$ ,

$$\begin{aligned} \nabla \cdot ((B(\phi) + \delta(\epsilon)) \nabla u) &= B(\Phi) \nabla_{\Gamma}^2 U + \epsilon^{-2} \partial_z ((B(\Phi) + \delta(\epsilon)) \partial_z U) \\ &\quad + \epsilon^{-1} \kappa (B(\Phi) + \delta(\epsilon)) \partial_z U + O(\epsilon), \end{aligned} \quad (6.15)$$

as  $B(\phi)$  varies normal to the surface only. The time derivatives are

$$\partial_t u = \partial_t U + \partial_s U \frac{\partial s}{\partial t} + \partial_r U \frac{\partial r}{\partial t}, \quad \partial_t v = \partial_t V + \partial_s V \frac{\partial s}{\partial t} + \partial_r V \frac{\partial r}{\partial t}, \quad (6.16)$$

which, for a surface that is fixed over time, reduce to

$$\partial_t u = \partial_t U, \quad \partial_t v = \partial_t V. \quad (6.17)$$

For small  $\epsilon$ , the series expansions for all of the variables and all of the new coordinates are

$$u(x, t; \epsilon) = u_0(x, t) + \mathcal{O}(\epsilon), \quad (6.18)$$

$$\hat{u}(r, s, t; \epsilon) = \hat{u}_0(r, s, t) + \mathcal{O}(\epsilon), \quad (6.19)$$

$$U(z, s, t; \epsilon) = U_0(z, s, t) + \epsilon U_1(z, s, t) + \epsilon^2 U_2(z, s, t) + \mathcal{O}(\epsilon^3), \quad (6.20)$$

$$v(x, t; \epsilon) = v_0(x, t) + \mathcal{O}(\epsilon), \quad (6.21)$$

$$\hat{v}(r, s, t; \epsilon) = \hat{v}_0(r, s, t) + \mathcal{O}(\epsilon), \quad (6.22)$$

$$V(z, s, t; \epsilon) = V_0(z, s, t) + \epsilon V_1(z, s, t) + \epsilon^2 V_2(z, s, t) + \mathcal{O}(\epsilon^3), \quad (6.23)$$

$$\phi_\epsilon(x) = \phi_0(x) + \mathcal{O}(\epsilon), \quad (6.24)$$

$$\hat{\phi}(r, s; \epsilon) = \hat{\phi}_0(r, s) + \mathcal{O}(\epsilon), \quad (6.25)$$

$$\Phi(z, s; \epsilon) = \Phi_0(z, s) = \varphi(z), \quad (6.26)$$

The third and sixth equations are written out to a higher order because they will be multiplied by terms of orders  $\epsilon^{-1}$  and  $\epsilon^{-2}$ ; therefore these higher order terms are required. The inner boundary layer mentioned when the stretched coordinate was introduced is the area close to the interface  $\Gamma$  and is defined by  $-\infty < z < \infty$ . The outer layer is the term used for the rest of the domain not in the immediate neighbourhood of  $\Gamma$ . In the transition region between these outer and inner layers it is assumed that the two expansions will give the same result, accomplished by requiring that the value of  $U_0$  while leaving the boundary layer ( $z \rightarrow \pm\infty$ ) is equal to the value of  $\hat{u}_0$  while entering the boundary layer ( $z \rightarrow \pm 0$ ). Therefore the matching condition

$$\lim_{z \rightarrow \pm\infty} U_0(z, s, t) = \lim_{z \rightarrow \pm 0} \hat{u}_0(r, s, t) \quad (6.27)$$

holds, and similarly

$$\lim_{z \rightarrow \pm\infty} V_0(z, s, t) = \lim_{z \rightarrow \pm 0} \hat{v}_0(r, s, t), \quad (6.28)$$

$$\lim_{z \rightarrow \pm\infty} \Phi_0(z, s) = \lim_{z \rightarrow \pm 0} \hat{\phi}_0(r, s). \quad (6.29)$$

As  $\phi_0 = 1$  inside the surface and  $\phi_0 = 0$  outside, the matching conditions give

$$\lim_{z \rightarrow -\infty} \Phi_0(z, s) = \lim_{z \rightarrow -0} \hat{\phi}_0(r, s) = 1 \quad (6.30)$$

and

$$\lim_{z \rightarrow +\infty} \Phi_0(z, s) = \lim_{z \rightarrow +0} \hat{\phi}_0(r, s) = 0. \quad (6.31)$$

Substituting (6.15) and expansions (6.20), (6.23) and (6.26) into the phase field approximation (6.5) gives

$$\begin{aligned} B(\Phi_0)\partial_t U_0 &= \epsilon^{-2}\partial_z(B(\Phi_0)\partial_z U_0) + \epsilon^{-1}(\partial_z(B(\Phi_0)\partial_z U_1) + \kappa B(\Phi_0)\partial_z U_0) \\ &\quad + \partial_z(B(\Phi_0)\partial_z U_2) + \kappa B(\Phi_0)\partial_z U_1 + B(\Phi_0)\nabla_{\Gamma}^2 U_0 \\ &\quad + \delta(\epsilon)(\epsilon^{-2}\partial_z^2 U_0 + \epsilon^{-1}\partial_z^2 U_1 + \epsilon^{-1}\kappa\partial_z U_0) \\ &\quad + B(\Phi_0)f(U_0, V_0) + \mathcal{O}(\epsilon), \end{aligned} \quad (6.32)$$

$$\begin{aligned} B(\Phi_0)\partial_t V_0 &= D[\epsilon^{-2}\partial_z(B(\Phi_0)\partial_z V_0) + \epsilon^{-1}(\partial_z(B(\Phi_0)\partial_z V_1) + \kappa B(\Phi_0)\partial_z V_0) \\ &\quad + \partial_z(B(\Phi_0)\partial_z V_2) + \kappa B(\Phi_0)\partial_z V_1 + B(\Phi_0)\nabla_{\Gamma}^2 V_0 \\ &\quad + \delta(\epsilon)(\epsilon^{-2}\partial_z^2 V_0 + \epsilon^{-1}\partial_z^2 V_1 + \epsilon^{-1}\kappa\partial_z V_0)] \\ &\quad + B(\Phi_0)g(U_0, V_0) + \mathcal{O}(\epsilon). \end{aligned} \quad (6.33)$$

The terms of order  $\epsilon^{-2}$  find  $\partial_z U_0 = 0$  and  $\partial_z V_0 = 0$ , which give  $\partial_z U_1 = 0$  and  $\partial_z V_1 = 0$  from the terms of order  $\epsilon^{-1}$ . Using both of these, the terms of order

$\epsilon^0$  give

$$\begin{aligned} B(\Phi_0)\partial_t U_0 &= \partial_z(B(\Phi_0)\partial_z U_2) + B(\Phi_0)\nabla_\Gamma^2 U_0 + B(\Phi_0)f(U_0, V_0), \\ B(\Phi_0)\partial_t V_0 &= D[\partial_z(B(\Phi_0)\partial_z V_2) + B(\Phi_0)\nabla_\Gamma^2 V_0] + B(\Phi_0)g(U_0, V_0). \end{aligned} \quad (6.34)$$

Integrating these equations with respect to  $z$  gives

$$\begin{aligned} \int_{-\infty}^{\infty} B(\Phi_0)dz\partial_t U_0 &= \int_{-\infty}^{\infty} B(\Phi_0)dz\nabla_\Gamma^2 U_0 + \int_{-\infty}^{\infty} B(\Phi_0)dzf(U_0, V_0), \\ \int_{-\infty}^{\infty} B(\Phi_0)dz\partial_t V_0 &= D \int_{-\infty}^{\infty} B(\Phi_0)dz\nabla_\Gamma^2 V_0 + \int_{-\infty}^{\infty} B(\Phi_0)dzg(U_0, V_0). \end{aligned} \quad (6.35)$$

The second term in each equation disappeared as

$$\lim_{z \rightarrow \infty} B(\Phi_0) = \lim_{z \rightarrow -\infty} B(\Phi_0) = 0. \quad (6.36)$$

Dividing by  $\int_{-\infty}^{\infty} B(\Phi_0)dz$  gives

$$\begin{aligned} \partial_t U_0 &= \nabla_\Gamma^2 U_0 + f(U_0, V_0), \\ \partial_t V_0 &= D\nabla_\Gamma^2 V_0 + g(U_0, V_0). \end{aligned} \quad (6.37)$$

With

$$\lim_{z \rightarrow \pm\infty} U_0 = \lim_{r \rightarrow \pm 0} u_0 = u_0|_\Gamma, \quad \lim_{z \rightarrow \pm\infty} V_0 = \lim_{r \rightarrow \pm 0} v_0 = v_0|_\Gamma, \quad (6.38)$$

the equations (6.37) is simply the reaction diffusion system (6.4) on the interface, which shows that the phase field approximation (6.5) over the whole domain converges to the original model on the interface when  $\epsilon \rightarrow 0$ .

Now that the asymptotic analysis process has been demonstrated, a surface approximation of the Delta-Notch model from Chapter 4 shall be derived

and an asymptotic analysis on the approximation will be used to prove its suitability.

### 6.3.2 The lateral inhibition model

A continuous Delta-Notch model based on the model by Collier et al. [45] was derived in Chapter 4. The equivalent model on a moving surface  $\Gamma$  takes the form

$$\begin{aligned} \frac{\partial n}{\partial t} + V \cdot \nabla_{\Gamma} n &= f(\bar{d}) - n, \\ \frac{\partial d}{\partial t} + V \cdot \nabla_{\Gamma} d &= \nu(g(n) - d), \quad \text{on } \Gamma \\ f(x) &= \frac{A_1 x^p}{a^p + x^p}, \quad g(x) = \frac{A_2 b^q}{b^q + x^q}, \end{aligned} \quad (6.39)$$

where  $V$  is the velocity of the surface and the neighbour function has the form

$$\bar{u}(\mathbf{x}, t) = \int_{-\infty}^{\infty} w(y) u(\mathbf{x} - y, t) dy. \quad (6.40)$$

The presence of this nonlocal neighbour term adds a degree of complexity to the asymptotic analysis; thus the corresponding phase field approximation of the model across the whole domain has a different form to the approximation for the reaction-diffusion model given in Section 6.3.1. The absence of a Laplacian here and the presence of the functions  $f$  and  $g$  does not give the desired dissipative behaviour away from the interface. Therefore a Laplacian is introduced outside the inner boundary layer to fix this. The approximation

becomes

$$\begin{aligned}
B(\phi)\frac{\partial\tilde{n}}{\partial t} + V \cdot \nabla(B(c)\tilde{n}) &= B(\phi)\tilde{f}_B(\bar{d}_B) - B(\phi)\tilde{n} + \delta A_1 \nabla^2 \tilde{n}, \\
B(\phi)\frac{\partial\tilde{d}}{\partial t} + V \cdot \nabla(B(c)\tilde{d}) &= \nu(B(\phi)\tilde{g}(\tilde{n}) - B(\phi)\tilde{d}) + \delta A_2 \nabla^2 \tilde{d}, \\
\tilde{f}_B(x) &= \frac{A_1 x^p}{(Ca)^p + x^p}, \quad \tilde{g}(x) = \frac{A_2 b^q}{b^q + x^q},
\end{aligned} \tag{6.41}$$

where

$$\bar{u}_B(\mathbf{x}, t) = \int_{-\infty}^{\infty} B(\phi(\mathbf{x} - y))w(y)u(\mathbf{x} - y, t)dy, \tag{6.42}$$

and  $C$  is a coefficient to be determined from the asymptotic analysis so that the approximation will reduce to the surface model. The model is transformed into the tangential and normal coordinates using

$$\mathbf{x} = \mathbf{X}(s, \epsilon) + r(x, \epsilon)\mathbf{n}(s, \epsilon), \tag{6.43}$$

and the stretched variable over the inner boundary layer is introduced again as  $z = \frac{r}{\epsilon}$ . As the velocity  $V$  is defined only on the interface, it is uniformly stretched over the inner boundary layer and as a result  $V$  is constant in the direction of  $z$ .

The variables  $n$ ,  $d$  and  $\phi$  are redefined for equations (6.41) using these coordinates. They are redefined in the same way as the variables  $u$ ,  $v$  and  $\phi$  in the reaction diffusion model (6.4) were redefined in Section 6.3.1, and the

gradient terms on the left-hand sides of the equations take the form

$$\begin{aligned} V \cdot \nabla(B(\phi)n) &= V \cdot (B(\Phi)\nabla_{\Gamma}N + \frac{\partial(B(\Phi)N)}{\partial r}\mathbf{n}) \\ &= V \cdot (B(\Phi)\nabla_{\Gamma}N + \epsilon^{-1}\partial_z(B(\Phi)N)\mathbf{n}), \end{aligned} \quad (6.44)$$

$$\begin{aligned} V \cdot \nabla(B(\phi)d) &= V \cdot (B(\Phi)\nabla_{\Gamma}D + \frac{\partial(B(\Phi)D)}{\partial r}\mathbf{n}) \\ &= V \cdot (B(\Phi)\nabla_{\Gamma}D + \epsilon^{-1}\partial_z(B(\Phi)D)\mathbf{n}), \end{aligned} \quad (6.45)$$

using equation (6.13). However, the nonlocal neighbour term  $\tilde{f}_B(\bar{d}_B)$  must also be redefined in the new coordinates. This can be achieved using a version of Lemma 2.1 from Du et al. [54]:

**Lemma.** *Let  $\Gamma$  be a smooth surface of dimension  $N - 1$ , within some  $N$ -dimensional domain  $\Omega$ . Let  $\Gamma_{\epsilon}$  be the phase field approximation of the surface  $\Gamma$  which converges to  $\Gamma$  as  $\epsilon \rightarrow 0$ . Let  $d$  be the signed distance from  $\Gamma$  and let  $p$  be an integrable function and  $g$  be a continuous function. Furthermore let  $p$  and  $g$  satisfy*

$$\max_{|t|>s} |p(t)t| \leq \frac{C}{s^m} \quad m > 1. \quad (6.46)$$

Then

$$\lim_{\epsilon \rightarrow 0} \frac{1}{\epsilon} \int_{\Omega} p\left(\frac{d(x)}{\epsilon}\right) g(x) dx = \int_{-\infty}^{\infty} p(t) dt \int_{\Gamma} g(z) dS(z). \quad (6.47)$$

Applying this Lemma to the nonlocal term in the Delta-Notch model yields:

$$\begin{aligned} \lim_{\epsilon \rightarrow 0} \bar{d}_B(\mathbf{x}, t) &= \lim_{\epsilon \rightarrow 0} \int_{\Omega} B\left(\varphi\left(\frac{\mathbf{x} - \mathbf{s}}{\epsilon}\right)\right) w(\mathbf{s}) d(\mathbf{x} - \mathbf{s}) d\mathbf{s} \\ &= \epsilon \int_{-\infty}^{\infty} B(\varphi(\mathbf{x} - r)) dr \int_{\Gamma} w(\mathbf{s}) d(\mathbf{x} - \mathbf{s}) dS \\ &= C \int_{\Gamma} w(\mathbf{s}) d(\mathbf{x} - \mathbf{s}) dS = C\bar{d}(x, t), \end{aligned} \quad (6.48)$$

where  $C$  is set as

$$C = \epsilon \int_{-\infty}^{\infty} B(\varphi(\mathbf{x} - r)) dr.$$

The function  $\tilde{f}_B$  can now be rewritten

$$\tilde{f}_B(\bar{d}_B) = \frac{A_1 \bar{d}_B^p}{(Ca)^p + \bar{d}_B^p} = \frac{A_1 C^p \bar{d}^p}{C^p (a^p + \bar{d}^p)} = f(\bar{d}), \quad (6.49)$$

and the model (6.41) in the new coordinates becomes

$$\begin{aligned} & B(\Phi_0) \partial_t N_0 + V \cdot [B(\Phi_0) \nabla_{\Gamma} N_0 + \epsilon^{-1} \partial_z (B(\Phi_0) N_0) \mathbf{n} + \partial_z (B(\Phi_0) N_1) \mathbf{n}] \\ &= B(\Phi_0) f(\bar{D}_0) - B(\Phi_0) N_0 + O(\epsilon), \end{aligned} \quad (6.50)$$

$$\begin{aligned} & B(\Phi_0) \partial_t D_0 + V \cdot [B(\Phi_0) \nabla_{\Gamma} D_0 + \epsilon^{-1} \partial_z (B(\Phi_0) D_0) \mathbf{n} + \partial_z (B(\Phi_0) D_1) \mathbf{n}] \\ &= \nu (B(\Phi_0) g(N_0) - B(\Phi_0) D_0) + O(\epsilon). \end{aligned} \quad (6.51)$$

Recalling that  $V$  is constant in the direction of  $z$ , integrating the  $\epsilon^0$  terms gives

$$\begin{aligned} & \int_{-\infty}^{\infty} B(\Phi_0) dz \partial_t N_0 + \int_{-\infty}^{\infty} B(\Phi_0) dz V \cdot \nabla_{\Gamma} N_0 \\ &= \int_{-\infty}^{\infty} B(\Phi_0) dz f(\bar{D}_0) - \int_{-\infty}^{\infty} B(\Phi_0) dz N_0 + O(\epsilon), \end{aligned} \quad (6.52)$$

$$\begin{aligned} & \int_{-\infty}^{\infty} B(\Phi_0) dz \partial_t D_0 + \int_{-\infty}^{\infty} B(\Phi_0) dz V \cdot \nabla_{\Gamma} D_0 \\ &= \nu \left( \int_{-\infty}^{\infty} B(\Phi_0) dz g(N_0) - \int_{-\infty}^{\infty} B(\Phi_0) dz D_0 \right) + O(\epsilon). \end{aligned} \quad (6.53)$$

It is now straightforward to obtain

$$\begin{aligned} \partial_t N_0 + V \cdot (\nabla_{\Gamma} N_0) &= f(\bar{D}_0) - N_0, \\ \partial_t D_0 + V \cdot (\nabla_{\Gamma} D_0) &= \nu (g(N_0) - D_0), \end{aligned} \quad (6.54)$$

which with the matching conditions

$$\lim_{z \rightarrow \pm\infty} N_0 = n_0|_{\Gamma}, \quad \lim_{z \rightarrow \pm\infty} D_0 = d_0|_{\Gamma}, \quad (6.55)$$

is the lateral inhibition model (6.39); therefore the approximation reduces to the lateral inhibition model on the interface when  $\epsilon \rightarrow 0$ .

## 6.4 Simulation of the surface lateral inhibition model

The surface lateral inhibition model given in Section 6.3.2 was simulated on multiple different interfaces, both stationary and moving, using domains of the form  $[-L, L]^2$ . The simulation uses a simple forward Euler scheme. Backward Euler would have been too complex to implement with the presence of the  $f(\bar{d})$  and  $g(n)$  functions. Periodic boundary conditions, now needed for both Notch and Delta due to the addition of the diffusion term  $\nabla^2 n$ , were used at the edges of the domain ( $n(-L, y, t) = n(L + h, y, t)$ ,  $n(x, -L, t) = n(x, L + h, t)$ ,  $d(-L, y, t) = d(L + h, y, t)$ ,  $d(x, -L, t) = d(x, L + h, t)$ ), and initial conditions used were similar to those in Chapter 4:

$$n(\mathbf{x}, 0) = 1 - \mathbf{r}(x), \quad d(\mathbf{x}, 0) = 1, \quad (6.56)$$

for uniformly distributed random number  $0 < \mathbf{r}(x) < 0.1$  for each  $x$ . These initial conditions were set across the whole domain, not just on the surface. The phase field surface model causes the initial perturbation to dissipate when away from the interface.

In all of the following simulations, the parameters of the Delta-Notch model

are set as

$$a = 0.1, \quad b = 0.1, \quad p = 3, \quad q = 3, \quad \nu = 1, \quad A_1 = 1, \quad A_2 = 1,$$

and the phase field parameters are set as  $\epsilon = 0.5$ ,  $\delta = 10^{-3}$ . The mesh size used is  $h = 0.125$ . The interface  $\Gamma$  is selected by setting  $s(\mathbf{x})$  in equation (6.1) for  $\phi$ :

$$\phi(\mathbf{x}) = \varphi\left(\frac{r}{\epsilon}\right) = \frac{1}{2} \left( 1 - \tanh\left(\frac{s(\mathbf{x})}{\epsilon}\right) \right). \quad (6.57)$$

The two-dimensional rectangle weight function

$$w(r, \theta) = \begin{cases} \frac{1}{2\pi} & 0.5 < r \leq 1.5, \\ 0 & \text{otherwise,} \end{cases} \quad (6.58)$$

is used for all simulations in this chapter.

### 6.4.1 Results with a stationary interface

A stationary interface has velocity  $V = 0$ . The equation of the interface  $\Gamma$  is  $s(\mathbf{x}) = 0$ . To set  $\Gamma$  as a circle of radius 2,  $s(\mathbf{x})$  takes the form

$$s(\mathbf{x}) = \sqrt{x^2 + y^2} - 2. \quad (6.59)$$

The circle has a circumference of  $4\pi \approx 12.5664$ . The wavelength  $\lambda$  is close to 2, therefore the wave should repeat approximately 6 times along the surface. Figure 6.3 shows a simulation of the Delta-Notch model on this circle at different times, for the domain  $[-4, 4]^2$ . Adjusting the circle radius will change the number of waves of the pattern. Figure 6.4 shows final Delta and Notch concentrations simulated on a circle of radius 5 (with circumference

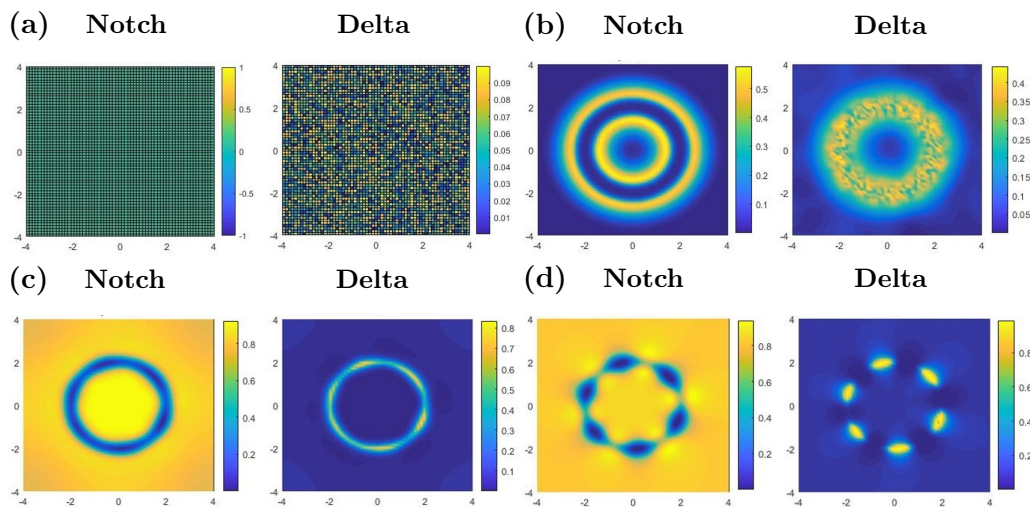


**Figure 6.3:** Notch and Delta concentrations over the domain  $[-4, 4]^2$  with mesh size  $h = 0.125$  on a circle of radius 2 (where the equation for the interface  $\Gamma$  is (6.59)), at times (a)  $t=0$ , (b)  $t=1$ , (c)  $t=7$ , (d)  $t=14$ . The circumference  $4\pi \approx 12.5664$  and the wave repeats approximately 6 times around the circle.

$10\pi \approx 31.4159$  and about 15 wave cycles) in the domain  $[-10, 10]^2$ .

Changing the definition of the interface  $\Gamma$  is simply a matter of changing  $s(\mathbf{x})$  in the equation (6.1). Figure 6.5 shows the simulation of the Delta-Notch model around an ellipse

$$s(x, y) = \sqrt{\left(\frac{x}{5}\right)^2 + \left(\frac{y}{2}\right)^2} - 1. \quad (6.60)$$

Figure 6.6 shows the results along a sine wave

$$s(x, y) = y - \sin(x), \quad (6.61)$$

which is the most similar surface here to the capillary surfaces that will form in the angiogenesis model in Chapter 7, and that the Delta-Notch model will be simulated on in the coupling in Chapter 8.

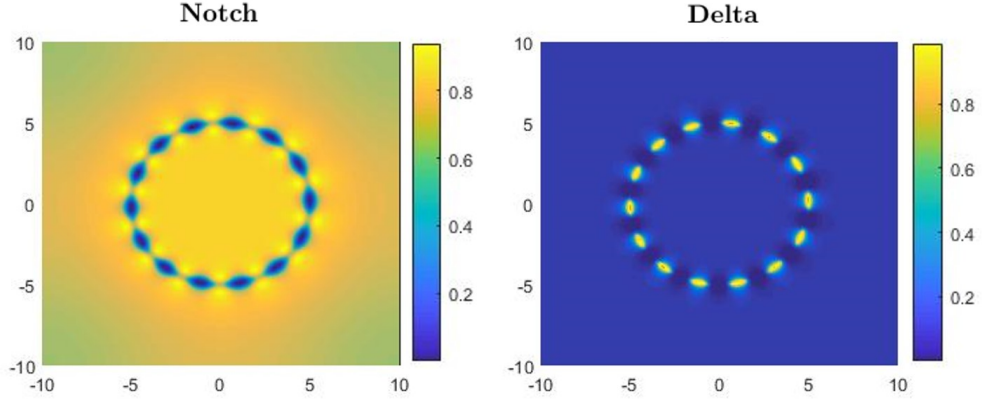


**Figure 6.4:** Solutions for Notch and Delta concentrations over the domain  $[-10, 10]^2$  on a circle of radius 5, circumference  $10\pi \approx 31.4159$ , at time  $t = 375$ .

## 6.4.2 Results with a moving interface

The model was also simulated on a moving surface, as the angiogenesis coupling will involve a moving interface. The simulations used the same 2D rectangle weight function and periodic boundary conditions. The interface used was the circle given in equation (6.59), but with time-dependent terms added:

$$s(\mathbf{x}) = \sqrt{(x - \sin(\omega t))^2 + (y + \cos(\omega t) - 1)^2} - 2, \quad (6.62)$$

where  $\omega$  is some constant used to control the velocity of the circle. The motion created by this function is simply an anticlockwise circular translation.

The patterning of the Delta-Notch model on this interface is successful when a suitable choice for  $\omega$  is made where it is not too large, such as  $\omega = \frac{\pi}{10}$ , but there are minor issues observed around the interface when the interface thickness  $\epsilon$  is smaller, where large fluctuations of the Delta and Notch levels occur. With a sufficient interface thickness, these numerical errors can be resolved, and the results found here are still evidence enough that the approximation

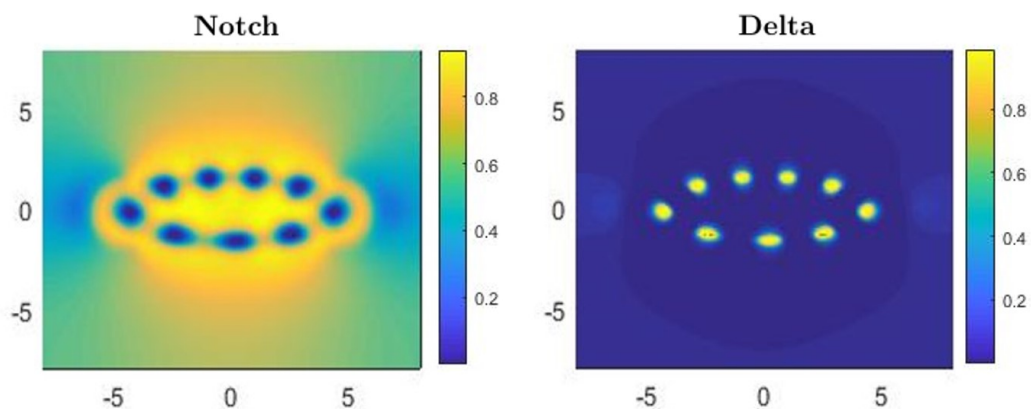


**Figure 6.5:** Final solutions of Notch and Delta on an ellipse with a major axis (horizontal length) of 10 and minor axis (vertical length) of 4 (interface equation (6.60)). The domain is  $[-10, 10]^2$ .

is sufficient.

## 6.5 Conclusion

The Delta-Notch model from Chapter 4 has been approximated on a surface by using a phase field parameter to define the variables across the whole domain and then introducing a function which is non-zero on the interface. Approximating the model using a phase field parameter will enable easier coupling to the phase field angiogenesis model later. The integrity of this approximation was tested using an asymptotic analysis to prove the convergence of the approximation to the surface model for  $\epsilon \rightarrow 0$ , complicated by the presence of the nonlocal term which was not present in phase field approximations by others. The model works on different types of stationary interface, as demonstrated in Section 6.4, and also works on moving interfaces for limited speeds. Changing the interface was straightforward, which is ideal for the moving boundary angiogenesis model that will be introduced in Chapter

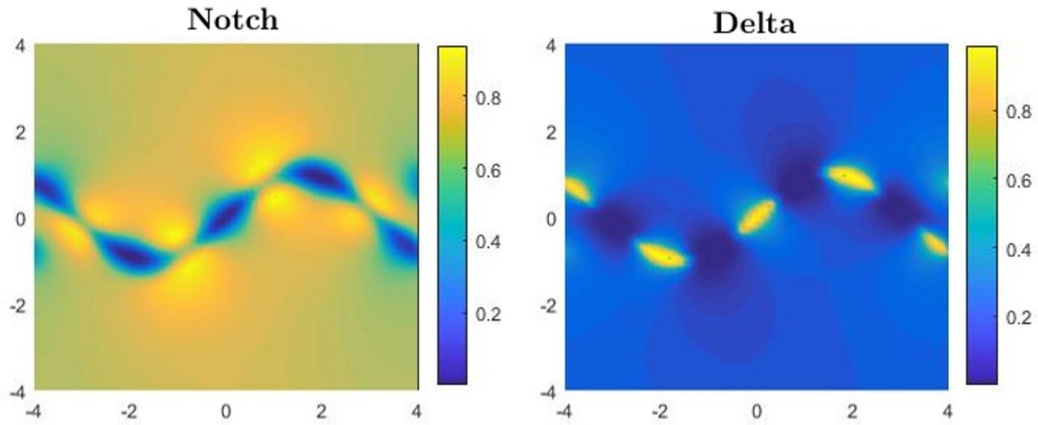


**Figure 6.6:** Final solutions for Notch and Delta concentrations when solved along a sine wave (with interface equation (6.61)), in the domain  $[-4, 4]^2$ .

7, which will require updates of the phase field parameter after every timestep.

The way the phase field approximation method works may cause issues which should be acknowledged. The Delta-Notch variables need to be defined everywhere across the whole domain, instead of just along the capillary surface. This may cause a problem when the interface is a complex shape, as sections along the capillary surface which are not adjacent may be considered adjacent by the model if they are within inhibition range. Such a problem may occur in an angiogenesis model involving a lot of branching.

Numerical issues arose with the moving interface when the interface thickness was small and the velocity of the interface was large. This is to be expected; however, these issues may improve with a more sophisticated time-stepping scheme, such as a Runge Kutta scheme. Adaptive mesh refinement along the interface would also be a useful development, given the peaks that will emerge in the angiogenesis model. A finer mesh around points on the interface with higher curvature may improve the solution; however a signif-

icant improvement may not be seen unless the interface thickness  $\epsilon$  is also changed. The problems caused away from the interface when the surface is moving would also benefit from an adaptive timestep, for example a timestep with a reverse correlation with the interfacial velocity.

The developments made in this chapter have prepared the Delta-Notch model for use in a phase-field angiogenesis model. Such a phase field model will be introduced next in Chapter 7, and the coupling of the two models will be shown in Chapter 8.

# Chapter 7

## A phase field model of angiogenesis

### 7.1 Introduction

The Delta-Notch model was developed to simulate activity along a surface in Chapter 6 so that it can be coupled to an angiogenesis model. This chapter will introduce the angiogenesis model to be used, and this and the surface Delta-Notch model will be coupled in Chapter 8. The angiogenesis model introduced in this chapter is a phase field model. The use of a phase field model will make the coupling to the surface Delta-Notch model later in Chapter 8 easier.

The angiogenesis process is triggered in a capillary by an angiogenic factor called Vascular Endothelial Growth Factor, or VEGF, which is released from cells that require oxygen, otherwise known as hypoxic cells. When VEGF reaches the endothelial cells in the capillary wall, some cells are chosen to migrate and are labelled tip endothelial cells (TECs) and the others proliferate

and become stalk endothelial cells (SECs). A TEC is only activated if there are no other TECs nearby, as TECs inhibit other cells within a certain radius from becoming TECs.

In this chapter, the model will simulate the formation of TECs in a simple way by having a TEC instantly form when a VEGF threshold is reached, as long as it is not within the inhibition radius of another TEC. Chapter 8 will see a more sophisticated representation of TEC selection by coupling to the surface lateral inhibition model from Chapter 6.

This chapter will start with a derivation of the Allen-Cahn and Cahn-Hilliard models using mass balance equations and the laws of thermodynamics in Section 7.2 to show the origin of phase field models, before introducing in Section 7.3 the discrete-continuous hybrid angiogenesis model by Travasso [139] that will be used. Results from simulating this hybrid model are shown in Section 7.4, and Section 7.5 is the concluding section.

## **7.2 Derivation of the Allen-Cahn and Cahn-Hilliard models**

Phase field models are mainly used for easier numerical computation, as the smooth interface removes the jump between phases and the exact location of the interface does not need to be defined; only the locations of the phases. Phase field models can also be used as an accurate depiction of certain phenomena, as there may actually be an interface between phases with a thickness. One example of this is solidification of ice, where water does not instantly turn to ice but is for a time between phases as it freezes [36].

Phase field models follow the laws of thermodynamics. They can be derived from an existing sharp interface model, which is sometimes called the “diffusification” of the problem, as stated by Gomez and Van der Zee [71]. However, diffusification does not guarantee the method will obey the classical laws of thermodynamics. Another way to derive a phase field model is to apply the laws of thermodynamics to mass balance and free energy equations.

The most well-known phase field models are the Allen-Cahn and Cahn-Hilliard models [2, 36]. They are gradient flows, which means the energy of the system is minimized over time. This section follows derivations by Gomez and Van der Zee [71] to see how the Allen-Cahn and Cahn-Hilliard equations can be derived using the laws of thermodynamics.

The free energy, or thermodynamic potential, is given by  $\Psi(\phi, \nabla\phi)$ . To find the total free energy across the entire domain  $\Omega$ , integrate to get the free energy functional:

$$\int_{\Omega} \Psi(\phi, \nabla\phi) d\mathbf{x}. \quad (7.1)$$

A common choice for the free energy  $\Psi$  is the free energy derived by Cahn and Hilliard [36], which takes the form

$$\Psi = W(\phi) + \frac{\epsilon^2}{2} |\nabla\phi|^2,$$

where  $W$  is a function of  $\phi$  and  $\epsilon$  is proportional to the interface thickness. The corresponding Ginzburg-Landau energy functional [70] is used by both the Allen-Cahn and Cahn-Hilliard models. The Ginzburg-Landau functional

has the form

$$\int_{\Omega} \Psi(\phi, \nabla\phi) d\mathbf{x} = \int_{\Omega} \left( W(\phi) + \frac{\epsilon^2}{2} |\nabla\phi|^2 \right) d\mathbf{x}. \quad (7.2)$$

The second law of thermodynamics states that free energy decreases over time, i.e. the free energy dissipation  $\mathcal{D}(\Omega) \geq 0$ . If  $\mathcal{W}(\Omega)$  is defined as the work from external forces through the domain boundary, the energy dissipation in the system can be shown as

$$\frac{d}{dt} \left( \int_{\Omega} \Psi(\phi, \nabla\phi) d\mathbf{x} \right) = \mathcal{W}(\Omega) - \mathcal{D}(\Omega) \quad (7.3)$$

$$= \int_{\Omega} \partial_{\phi} \Psi \partial_t \phi + \partial_{\nabla\phi} \Psi \cdot \partial_t(\nabla\phi) d\mathbf{x}. \quad (7.4)$$

Using the chain rule and integration by parts

$$\begin{aligned} \frac{d}{dt} \left( \int_{\Omega} \Psi(\phi, \nabla\phi) d\mathbf{x} \right) &= \int_{\Omega} \partial_{\phi} \Psi \partial_t \phi d\mathbf{x} + \int_{\Omega} \partial_{\nabla\phi} \Psi \cdot \partial_t(\nabla\phi) d\mathbf{x} \\ &= \int_{\Omega} \partial_{\phi} \Psi \partial_t \phi d\mathbf{x} + \int_{\partial\Omega} \partial_{\nabla\phi} \Psi \cdot \mathbf{n} \partial_t \phi da \\ &\quad - \int_{\Omega} \nabla \cdot \partial_{\nabla\phi} \Psi \partial_t \phi d\mathbf{x} \\ &= \int_{\partial\Omega} \partial_{\nabla\phi} \Psi \cdot \mathbf{n} \partial_t \phi da + \int_{\Omega} \mu \partial_t \phi d\mathbf{x}, \end{aligned} \quad (7.5)$$

for unit normal  $\mathbf{n}$  to domain boundary  $\partial\Omega$ , and for variational derivative

$$\mu = \frac{\delta}{\delta\phi} \int_{\Omega} \Psi d\mathbf{x} = \partial_{\phi} \Psi - \nabla \cdot \partial_{\nabla\phi} \Psi. \quad (7.6)$$

### 7.2.1 The Allen-Cahn Equation

The Allen-Cahn equation models non-conserved phase systems, and can be derived using the balance equation

$$\partial_t \phi = -R(\phi, \nabla \phi, \mu), \quad (7.7)$$

where  $R$  is a energy dissipative function to be found. Substituting this into equation (7.5) gives

$$\frac{d}{dt} \int_{\Omega} \Psi d\mathbf{x} = \int_{\partial\Omega} \partial_{\nabla\phi} \Psi \cdot \mathbf{n} \partial_t \phi da - \int_{\Omega} \mu R d\mathbf{x}. \quad (7.8)$$

The first term of (7.8) is the external work term  $\mathcal{W}(\Omega)$ , as it is defined on the boundary. The second term is therefore the dissipation term, and  $\mathcal{D}(\Omega) = \int_{\Omega} \mu R d\mathbf{x}$ . Choosing  $R = m(\phi)\mu$  for some  $m(\phi) \geq 0$  satisfies the free-energy dissipation law. Therefore the mass balance equation (7.7) becomes

$$\partial_t \phi = -m(\phi)\mu. \quad (7.9)$$

Calculating the variational derivative  $\mu$  from the Ginzburg-Landau functional (7.2) gives the Allen-Cahn equation:

$$\partial_t \phi = -m(\phi) (W'(\phi) - \epsilon^2 \Delta \phi). \quad (7.10)$$

### 7.2.2 The Cahn-Hilliard Equation

Deriving the Cahn-Hilliard equation is similar, but it models conserved phase systems, and so the following mass conservation equation is used:

$$\partial_t \phi = -\nabla \cdot \mathbf{h}. \quad (7.11)$$

Substituting into (7.5) yields

$$\frac{d}{dt} \int_{\Omega} \Psi d\mathbf{x} = \int_{\partial\Omega} \partial_{\nabla\phi} \Psi \cdot \mathbf{n} \partial_t \phi da - \int_{\Omega} \mu \nabla \cdot \mathbf{h} d\mathbf{x}. \quad (7.12)$$

Integrating by parts gives

$$\begin{aligned} \frac{d}{dt} \int_{\Omega} \Psi d\mathbf{x} &= \int_{\partial\Omega} \partial_{\nabla\phi} \Psi \cdot \mathbf{n} \partial_t \phi da - \int_{\partial\Omega} \mu \mathbf{h} \cdot \mathbf{n} da + \int_{\Omega} \nabla \mu \cdot \mathbf{h} d\mathbf{x} \\ &= \int_{\partial\Omega} (\partial_{\nabla\phi} \Psi \partial_t \phi - \mu \mathbf{h}) \cdot \mathbf{n} da + \int_{\Omega} \nabla \mu \cdot \mathbf{h} d\mathbf{x}. \end{aligned} \quad (7.13)$$

The dissipation is therefore  $\mathcal{D}(\Omega) = \int_{\Omega} -\nabla \mu \cdot \mathbf{h} d\mathbf{x}$ , and  $\mathbf{h} = -m(\phi) \nabla \mu$  is chosen to satisfy the free-energy dissipation law. Substituting this into (7.11) derives the Cahn-Hilliard equation:

$$\partial_t \phi = \nabla \cdot (m(\phi) \nabla (W'(\phi) - \epsilon^2 \Delta \phi)). \quad (7.14)$$

### 7.3 A phase field model for angiogenesis

This section presents the hybrid angiogenesis model by Travasso et al. [139] that will be used. Angiogenesis models have an equation for the movement of the endothelial cells, and another equation for the diffusion and uptake of the angiogenic factor VEGF. The location of the endothelial tissue, or endothelium, will be modelled here using a phase field parameter  $c$ , where  $c = 1$  is the endothelium phase and  $c = -1$  is the Extracellular Matrix (ECM) phase, so that  $-1 < c < 1$  represents the interface between the endothelial tissue and the ECM. The model will simulate early stages of angiogenesis, where the system is not yet mature and has not yet developed into blood vessels with a lumen for the blood to flow through, and therefore the phase field model has no lumen or blood phase.

The phase field model uses a Cahn-Hilliard-type equation to represent the interfacial dynamics, with an extra term added for the proliferation of endothelial cells which is triggered by interaction with VEGF. A simple reaction-diffusion equation represents the dynamics of the VEGF concentration  $f$ , where the reaction term represents the uptake of factor by the nearby capillaries. The other vital elements which should be included in such a model, such as the source of VEGF and the initiation of a new branching capillary, will be incorporated in the discrete part of the model. The continuous equations take the following form:

$$\begin{aligned}\frac{\partial f}{\partial t} &= D\Delta f - B_u f c \mathcal{H}(c), \\ \frac{\partial c}{\partial t} &= M\Delta(\mu_c - \lambda^2 \Delta c) + B_p(f) c \mathcal{H}(c),\end{aligned}\tag{7.15}$$

where the initial condition for  $c$  is set using a tanh function similar to the equation for  $\phi$  in (6.1):

$$c(\mathbf{x}, 0) = -\tanh\left(\frac{y - 2R_V}{\sqrt{2}\lambda}\right),\tag{7.16}$$

for capillary radius  $R_V$ . This model has many parameters which are described in more detail in Section 7.3.2. As stated before, the equation for VEGF concentration (7.15)<sub>1</sub> is a simple reaction-diffusion equation with diffusion coefficient  $D$ . The reaction term represents uptake of VEGF by endothelial cells with uptake rate  $B_u$  and this term only exists where  $c > 0$ , as ensured by the Heaviside function  $\mathcal{H}(c)$ . Equation (7.15)<sub>2</sub> is a Cahn-Hilliard equation

with a reaction term, where

$$B_p(f) = \begin{cases} B_p f & \text{for } f < f_p, \\ B_p f_p & \text{for } f \geq f_p. \end{cases} \quad (7.17)$$

$M$  is a coefficient related to the mobility of the endothelial cells. The chemical potential is  $\mu_c - \lambda^2 \Delta c$  where  $\mu_c$  is found from the variational derivative definition as  $\mu_c = c^3 - c$ .  $\lambda$  is the interfacial thickness between the phases.

### 7.3.1 The discrete component

The other important parts of angiogenesis which have not yet been included in the model, specifically the presence and behaviour of the tip endothelial cells and hypoxic cells (which act as a VEGF source), will be covered by discrete components in the model. The incorporation of these components in the model will be detailed here.

#### The tip endothelial cells

The way tip endothelial cells activate, migrate and deactivate again is represented discretely in this chapter, but these discrete components will be replaced by the continuous lateral inhibition model in Chapter 8. If a spatial point  $\mathbf{x}^*$  meets certain criteria, a new tip endothelial cell will be created with  $\mathbf{x}^*$  as its centre. The criteria that must be met involve the values of  $c(\mathbf{x}^*)$ ,  $f(\mathbf{x}^*)$ , and  $\nabla f(\mathbf{x}^*)$ , which must meet certain thresholds for a tip cell to activate. The motivation behind these criteria are clear; any new TECs must be above a certain value of  $c$  to be considered part of the endothelium phase, and the VEGF concentration and its gradient must be high enough to activate a cell. Also, the distance from other tip endothelial cells is needed to check

if TEC activation is blocked through lateral inhibition. Mathematically, the criteria the centre of a new tip endothelial cell  $\mathbf{x}^*$  must meet is as follows:

- $c(\mathbf{x}^*) \geq c_{act}$ ,
- $f(\mathbf{x}^*) \geq f_{act}$ ,
- $\nabla f(\mathbf{x}^*) \geq G_{act}$ ,
- $|\mathbf{x}^* - \mathbf{x}_{TEC}^j| \geq \delta_4, \forall j = 1, \dots, N_{TEC}(t_n)$ ,

where  $\delta_4$  is the range of the lateral inhibition signalling and  $\mathbf{x}_{TEC}^j$  is the centre of the  $j$ th existing TEC. It should be noted that if more than one location exists that meets the above criteria, then the location with the highest VEGF level is selected as a tip endothelial cell, as only one is formed per timestep to prevent activation of many at the same time that are closer than the inhibition range. As soon as any one of the above criteria is no longer met by a TEC, the TEC is deactivated. Once the centres of the tip endothelial cells have been found, a subdomain for each centre  $\mathbf{x}_{TEC}^l$  which defines the domain of each tip endothelial cell is found as

$$\Omega_{TEC}^l(t_{n+1}) = \{\mathbf{x} \in \Omega | \mathbf{x} - \mathbf{x}_{TEC}^l| \leq R_{EC}\}. \quad (7.18)$$

The  $c$ -values within these tip endothelial cell subdomains will be overwritten; within each TEC  $i$  defined by the subdomain  $\Omega_{TEC}^i$ , the new  $c$  values are defined as

$$c_{TEC}^i = \frac{B_p(f_{TEC}^i)\pi R_{EC}}{2|\mathbf{v}_{TEC}^i|}, \quad (7.19)$$

where  $R_{EC}$  is the average radius of endothelial cells,  $f_{TEC}^i$  is the concentration of VEGF at the centre of the TEC, and  $\mathbf{v}_{TEC}^i$  is the velocity of the TEC,

calculated at the centre of the TEC with a formula used by Travasso:

$$\mathbf{v}_{TEC}^i = \chi \nabla f(\mathbf{x}_{TEC}^i) \mathcal{L}(|\nabla f(\mathbf{x}_{TEC}^i)|), \quad (7.20)$$

with chemotactic constant  $\chi$ . The limiting function  $\mathcal{L}(|\nabla f(\mathbf{x}_{TEC}^i)|)$  is defined as

$$\mathcal{L}(|\nabla f(\mathbf{x}_{TEC}^i)|) = 1 + \left( \frac{G_M}{|\nabla f|} - 1 \right) \mathcal{H}(|\nabla f| - G_M), \quad (7.21)$$

which gives a maximum velocity of  $\mathbf{v}_{TEC}^i = \chi G_M$ , where  $G_M$  is a predetermined parameter for the value of  $|\nabla f|$  that corresponds to the maximum velocity. Equation (7.19) is a ratio of endothelial tissue produced and area swept by the tip endothelial cell per timestep.

To implement these discrete components for the tip endothelial cells computationally and combine them with the continuous equations (7.15), a diffuse approximation for the  $c$ -values is calculated to combine with the phase field model, using another interface thickness  $\epsilon$ . Noting that  $c$  must take values  $-1 \leq c \leq 1$ , and recalling that the centre of the  $k$ th TEC is denoted  $\mathbf{x}_{TEC}^k$ , the approximation for the  $c$  values in each of the subdomains  $\Omega$  is

$$g_c^i(\mathbf{x}) = \left( \frac{c_{TEC}^i - 1}{2} \right) - \left( \frac{c_{TEC}^i + 1}{2} \right) \tanh \left( \frac{|\mathbf{x} - \mathbf{x}_{TEC}^i| - R_{EC}}{2\epsilon} \right), \quad (7.22)$$

and the combination of these  $g_c^i$  is given as

$$g_c(\mathbf{x}) = \max(g_c^i(\mathbf{x})). \quad (7.23)$$

Figure 7.1(a) graphs  $g_c^i(\mathbf{x})$  for two tip endothelial cell locations with the resulting  $g_c(\mathbf{x})$ . The  $c$  values  $c_D(\mathbf{x}, t_n)$  that will be used in the continuous equations

for the  $n$ th timestep ( $t = t_n$ ) are found using

$$c_D(\mathbf{x}, t_n) = \max(c(\mathbf{x}, t_{n-1}), g_c(\mathbf{x})). \quad (7.24)$$

### The hypoxic cells

The source of VEGF ( $f$ ) in the model is represented by the presence of hypoxic cells. Initially a number of hypoxic cells  $N_{HC}$  are randomly distributed. A change in the number of hypoxic cells in this model occurs only if a hypoxic cell  $\mathbf{x}_{HC}$  is saturated and thus deactivated. This is when there exists a  $\mathbf{x}$  such that  $c(\mathbf{x}) > c_{act}$  and

$$|\mathbf{x}_{HC} - \mathbf{x}| < f_{sat}, \quad (7.25)$$

where  $f_{sat}$  is the nutrient diffusion range, which is the distance from a capillary at which nutrient has dissipated below some tissue saturation threshold. Any hypoxic cells with centre within this nutrient diffusion range will be saturated. The subdomain  $\Omega_{HC}^l$  for hypoxic cell with centre  $\mathbf{x}_{HC}^l$  is

$$\Omega_{HC}^l(t_{n+1}) = \{\mathbf{x} \in \Omega | \mathbf{x} - \mathbf{x}_{HC}^l | \leq R_{HC}\}. \quad (7.26)$$

As with the tip endothelial cells, the values of  $f$  in the hypoxic cell subdomains are also overwritten, but they are simply overwritten with a predetermined parameter  $f_{HC}$  equal to the VEGF concentration in the hypoxic cells:

$$f_{HC}^i = f_{HC}. \quad (7.27)$$

The computational implementation uses a different diffuse approximation to the diffuse approximation of the  $c$  values in the tip endothelial cells, as  $f$  takes values  $0 \leq f \leq 1$ . The values of  $f$  to be input into continuous equations

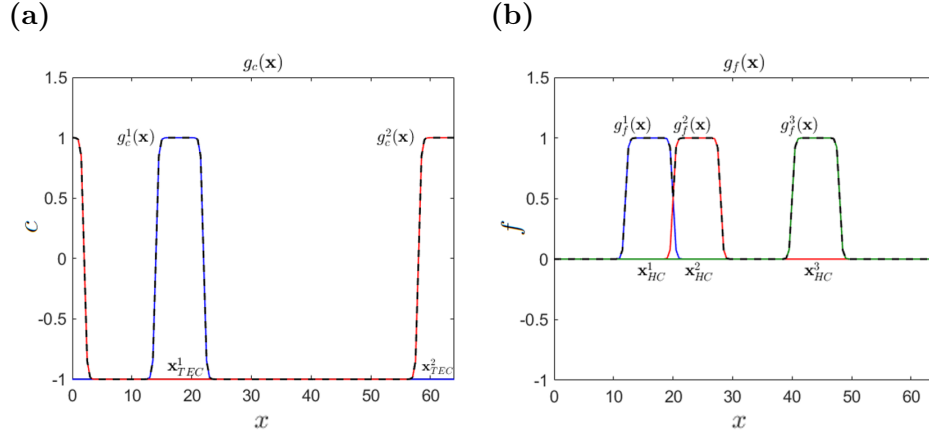


**Figure 7.1:** Approximations of the discrete components using example TECs and HCs; **(a)** the functions  $g_c^i(\mathbf{x})$ , which approximate the values of  $c$  in the TEC with centre  $\mathbf{x}_{TEC}^1$ , shown in blue, and the TEC with centre  $\mathbf{x}_{TEC}^2$ , shown in red, with the combination of both,  $g_c(\mathbf{x})$ , shown with a dashed line, **(b)** the functions  $g_f^i(\mathbf{x})$  which approximate the values of  $f$  in the hypoxic cell with centre  $\mathbf{x}_{HC}^1$ , shown in blue, the hypoxic cell with centre  $\mathbf{x}_{HC}^2$ , shown in red, and the hypoxic cell with centre  $\mathbf{x}_{HC}^3$ , shown in green, with the combination of them all,  $g_f(\mathbf{x})$ , shown with a dashed line.

(7.15) at the  $n$ th timestep are

$$f_D(\mathbf{x}, t_n) = \max(f(\mathbf{x}, t_{n-1}), g_f(\mathbf{x})), \quad (7.28)$$

using the approximation

$$g_f^i = f_{HC}^i \left( \frac{1}{2} - \frac{1}{2} \tanh \left( \frac{|\mathbf{x} - \mathbf{x}_{HC}^i| - R_{HC}}{2\epsilon} \right) \right), \quad (7.29)$$

and

$$g_f(\mathbf{x}) = \max(g_f^i(\mathbf{x})). \quad (7.30)$$

Figure 7.1(b) shows the  $g_f^i(\mathbf{x})$  functions for three example hypoxic cell locations and the resulting  $g_f(\mathbf{x})$  function.

### 7.3.2 Biological interpretation of the phase field model

It can be difficult to interpret phase field models in a biological sense. In this case, the smooth interface has no physical meaning and is used for computational ease, as when simulating the Delta-Notch model on the surface in Chapter 6. In reality, the thickness of the interface would be zero; the interface between capillaries and the extracellular matrix does not exist (see again Figure 3.1 from Chapter 6).

The values of  $f$  representing the angiogenic factor VEGF only vary between zero and one and can be thought of as being relative to the maximum ( $f = 1$ ) and minimum ( $f = 0$ ) concentration of VEGF. The values of  $c$  are similar, but cannot be thought of as an exact ratio in the same way. If the values of  $c$  are thought of as being analogous to the maximum ( $c = 1$ ) and minimum ( $c = -1$ ) density of endothelial cells, this would be inaccurate, as the interface  $-1 < c < 1$  does not exist biologically. A better visualisation would be to think of  $c$  as being analogous to the presence ( $c = 1$ ) and absence ( $c = -1$ ) of endothelial cells instead (recall that the blood passages of the capillaries have not yet formed in this early stage of angiogenesis), which supports the earlier statement about the interface  $-1 < c < 1$  not existing in biological terms.

Behaviour observed in laboratory experiments is used to assign quantitative values to the parameters. The diffusion of VEGF  $D$ , set at around  $D = 10^{-1}$  micrometres squared ( $\mu\text{m}^2$ ) per second (where  $1\mu\text{m} = 10^{-6}\text{m}$ ), is based on values from Schugart et al. [129], as is the value for the endothelial cell mobility  $M$ , set at  $M = 10^{-3} \mu\text{m}^2 \text{ s}^{-1}$ . The proliferation constant  $B_p$  is found as  $B_p = 8.981 \times 10^{-4} \text{ s}^{-1}$ , as the maximum proliferation rate is fixed at  $\max(B_p(f)) = B_p f_p = 0.97 \text{ hr}^{-1}$ , as it is in the Travasso model, and the

dimensionless parameter  $f_p$  is set by Vilanova as  $f_p = 0.3$ . The uptake constant  $B_u$  is set as  $B_u = \frac{D}{R_{EC}^2}$ , as endothelial cell walls cause the uptake of factor to decrease with cell size. From Gebb and Stevens [68], the cell radii are  $R_{EC} = R_{HC} = 5 \mu\text{m}$ , which fixes  $B_u = 0.004 \text{ s}^{-1}$ . The value for the radius  $R_V$  is set at  $12.5 \mu\text{m}$ .

The range of lateral inhibition is twice the endothelial cell diameter, as noted when selecting the lateral inhibition weight functions in Chapter 4, so  $\delta_4 = 20 \mu\text{m}$ . The saturation distance is set as  $f_{sat} = 25 \mu\text{m}$ , as the distance away from a capillary that tissue is still saturated with oxygen is stated by Grote to be  $25 \mu\text{m}$  [77].

$c_{act}$  is a dimensionless quantity, as it is a value of the phase field. It is set at  $c_{act} = 0.9$ , which is chosen to be moderately high as it must define the capillary phase. Similarly,  $f_{act}$ ,  $f_p$  and  $f_{HC}$  are all also dimensionless. The value given to the VEGF level at maximum proliferation,  $f_p$ , was stated earlier when setting the proliferation rate. The amount of VEGF found in the centre of the hypoxic cells is set as  $f_{HC} = 1$ , because it is in the hypoxic cells where the largest ratio of VEGF is found. The VEGF threshold where tip cells can activate,  $f_{act}$ , is taken from Travasso, who made sure  $f_{act}$  was lower than the maximum value of  $f$  that can be found in the endothelium phase; this value was found to be at  $f = 0.061$ , so the threshold for emerging TECs is set at  $f_{act} = 0.055$ . VEGF gradient-related parameters  $G_{act}$  and  $G_M$  are set at values estimated by Travasso after a parametric study of the model; these are  $G_{act} = 0.008 \mu\text{m}^{-1}$  and  $G_M = 0.024 \mu\text{m}^{-1}$ . The chemotactic constant  $\chi$  is given the value  $\chi = 14.583 \mu\text{m}^2 \text{ s}^{-1}$  by setting the maximum velocity  $\chi G_M \approx 0.35 \mu\text{m} \text{ min}^{-1}$ .

The dimensionless versions of the parameters must be calculated to be used in the dimensionless equations. These can be found using the length and time scales, set by fixing the cell radii as  $R_{EC} = R_{HC} = 4$  length units, which means the length scale is 1 length unit =  $1.25 \mu\text{m}$ , and fixing  $M = 1$  sets the time scale as 1 time unit =  $\frac{1.25^2}{10^{-3}} \approx 26$  minutes.

Lastly the interface parameters  $\lambda$  and  $\epsilon$  are set. The interfacial width of the endothelium-ECM interface  $\lambda$  is an important parameter in a phase field model; choosing the optimal value is vital. As the interface is non-existent in reality,  $\lambda$  will ideally be as close to zero as possible. A simple parametric study on  $\lambda$  (which is shown later in Section 7.4, Figure 7.9) verified that setting the interfacial width as one length unit ( $\lambda = 1$ ) is a sufficient choice;  $\lambda = 1$  still produces similar results to those produced for smaller  $\lambda$  values, but without the numerical errors that result from these smaller values for the selected mesh size. The interfacial width for the diffuse approximations of the discrete components is set as  $\epsilon = 0.1$ . This is because the mesh for these approximations is finer than that used for the continuous part of the model.

Table 7.1 summarises all the values allocated to each parameter in this section with their dimensional and dimensionless forms. These allocated values are the control values, and are the values used in all simulations of Section 7.4 except where a parameter value is clearly stated otherwise.

Parameter	Symbol	Real value	Dimensionless value
Length scale	$L$	$1.25 \mu\text{m}$	1
Time scale	$T$	1560s	1
Diffusion coefficient of $f$	$D$	$10^{-1} \mu\text{m}^2 \text{s}^{-1}$	100
Mobility coefficient of $c$	$M$	$10^{-3} \mu\text{m}^2 \text{s}^{-1}$	1
Tip endothelial cell radius	$R_{EC}$	$5 \mu\text{m}$	4
Hypoxic cell radius	$R_{HC}$	$5 \mu\text{m}$	4
Radius of the initial capillary	$R_V$	$12.5 \mu\text{m}$	10
Uptake rate of VEGF	$B_u$	$0.004 \text{s}^{-1}$	6.25
Proliferative rate of ECs	$B_p$	$8.981 \times 10^{-4} \text{s}^{-1}$	1.401
Range of lateral inhibition	$\delta_4$	$20 \mu\text{m}$	16
Nutrient diffusion length	$f_{sat}$	$25 \mu\text{m}$	20
TEC threshold for EC phase	$c_{act}$	N/A	0.9
VEGF level in hypoxic cells	$f_{HC}$	N/A	1
TEC VEGF threshold	$f_{act}$	N/A	0.055
VEGF cap on EC proliferation	$f_p$	N/A	0.3
TEC VEGF gradient threshold	$G_{act}$	$0.008 \mu\text{m}^{-1}$	0.01
VEGF gradient cap on velocity	$G_M$	$0.024 \mu\text{m}^{-1}$	0.03
Chemotactic constant	$\chi$	$14.583 \mu\text{m}^2 \text{s}^{-1}$	242.67
Interfacial width for the continuous equations	$\lambda$	$1.25 \mu\text{m}$	1
Interfacial width for the discrete component approximation	$\epsilon$	$0.125 \mu\text{m}$	0.1

**Table 7.1:** Dimensional and dimensionless values of the parameters of the model.

## 7.4 Simulation of the angiogenesis model

The initial condition for the phase field  $c$  was given in equation (7.16) as

$$c(\mathbf{x}, 0) = -\tanh\left(\frac{y - 2R_V}{\sqrt{2}\lambda}\right), \quad (7.31)$$

which imitates an original capillary located at the bottom of the domain. For VEGF concentration  $f$ , the initial condition sets  $f(\mathbf{x}, 0) = f_{HC}$  in all hypoxic cells and  $f(\mathbf{x}, 0) = 0$  elsewhere. The locations of the hypoxic cells will be specified in Section 7.4.2.

The model applies periodic boundary conditions in the horizontal direction, but symmetric Neumann boundary conditions in the vertical direction, to prevent the bottom capillary from sprouting through to the top of the domain. Finite differences are used in the surface Delta-Notch model and therefore are also used here in the angiogenesis model. The mesh used by the discrete components and the simulation plots is twice as fine as the mesh used by the continuous equations to make the mesh size used as small as possible without significantly affecting the simulation speed. The finer mesh is calculated by interpolating the results of the continuous part of the model.

### 7.4.1 Convex splitting

A fully explicit scheme for the simulation will need to rely on a small timestep to maintain stability, as the Cahn-Hilliard equation is a nonconvex gradient flow and therefore a unique stable solution is not guaranteed. To improve performance, a semi-implicit scheme can be used instead which is split across timesteps in a way that causes the scheme to be unconditionally gradient stable, which means the simulation remains stable for all timesteps. The splitting

is found using Eyre's convex splitting method [58].

The method can be used to find an appropriate numerical scheme for a gradient flow of the form

$$\frac{\partial u}{\partial t} = -\nabla \mathcal{F}(u), \quad (7.32)$$

for function  $\mathcal{F} : \mathbb{R} \rightarrow \mathbb{R}$ , which does not increase over time (i.e.  $\frac{d(\mathcal{F}(u))}{dt} \leq 0$ ). If  $\mathcal{F}(u)$  is convex, that is, if its second derivative  $\mathcal{F}''(u)$  is never smaller than zero, then a unique stable solution already exists and the flow is contractive. For nonconvex  $\mathcal{F}(u)$ , the convex splitting method splits  $\mathcal{F}(u)$  into a contractive stable term and an expansive growth term, and rewrites  $\mathcal{F}(u)$  as the difference of two convex functions  $\mathcal{F}_c(u)$ ,  $\mathcal{F}_e(u)$ :

$$\mathcal{F}(u) = \mathcal{F}_c(u) - \mathcal{F}_e(u). \quad (7.33)$$

Figure 7.2 shows an example of such a splitting into two convex functions. The new scheme is unconditionally stable as it expresses the expansive term  $-\mathcal{F}_e(u)$  explicitly and the contractive term  $\mathcal{F}_c(u)$  implicitly:

$$\frac{U_{n+1} - U_n}{\tau} = \nabla \mathcal{F}_e(U_n) - \nabla \mathcal{F}_c(U_{n+1}). \quad (7.34)$$

Proof of the unconditional stability of this scheme is given by Eyre [58].

The convex splitting method is used to split the Cahn-Hilliard part of equation (7.15)<sub>1</sub> to make the simulation of the angiogenesis model run faster. This is achieved by finding a splitting for the gradient flow

$$\frac{\partial c}{\partial t} = M\Delta(\mu_c - \lambda^2\Delta c), \quad \mu_c = c^3 - c. \quad (7.35)$$

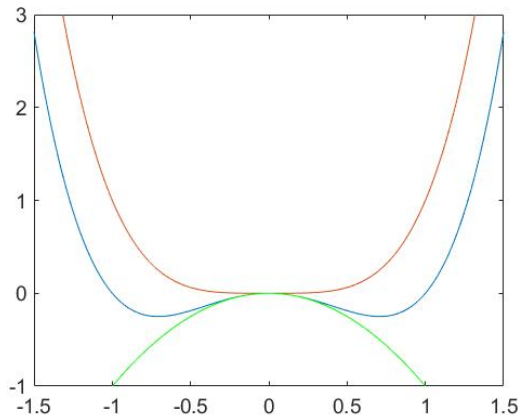


**Figure 7.2:** The function  $\mathcal{F}(u) = u^4 - u^2$ , shown in blue, is a non-convex function. This can be rewritten in terms of two convex functions  $\mathcal{F}_c(u)$  and  $\mathcal{F}_e(u)$ :  $\mathcal{F}(u) = \mathcal{F}_c(u) - \mathcal{F}_e(u)$ , where  $\mathcal{F}_c(u) = u^4$  is in red and  $-\mathcal{F}_e(u) = -u^2$  is in green.

There are many ways to define the contractive and expansive terms  $\mathcal{F}_c(u)$  and  $\mathcal{F}_e(u)$ , as the only requirement for stability is that both must be convex functions. However, is it also desirable that:

- The truncation error is small, and
- The resulting scheme is straightforward to simulate.

To find a splitting with the lowest truncation error possible, set  $\mathcal{F}_e(u)$  as the sum of the expansive terms of  $\mathcal{F}(u)$  and  $\mathcal{F}_c(u)$  as the sum of the contractive terms, as no extra terms are added and subtracted in the splitting. Considering each term of equation (7.35) individually, the term  $-\lambda^2 \Delta^2 c$  represents diffusion and is stable. As for the chemical potential terms,  $-\Delta c$  is expansive and causes the interesting behaviour of the flow, and  $\Delta c^3$  stabilises the flow. Therefore a potential splitting is

$$\frac{C_{n+1} - C_n}{\tau} = M\Delta[(C_{n+1})^3 - \lambda^2 \Delta C_{n+1}] - M\Delta C_n. \quad (7.36)$$

However, the implicit nonlinear term  $c^3$  will make the scheme difficult to simulate, so a linearly stabilised splitting scheme will be found instead. Such a scheme is linear in  $C_{n+1}$ , and is given by

$$\frac{C_{n+1} - C_n}{\tau} = M\Delta[2C_{n+1} - \lambda^2\Delta C_{n+1}] + M\Delta[(C_n)^3 - 3C_n], \quad (7.37)$$

and the scheme used for equation (7.15)<sub>1</sub> in the simulation of the angiogenesis model is

$$\begin{aligned} \frac{C_{n+1} - C_n}{\tau} = & M\Delta[2C_{n+1} - \lambda^2\Delta C_{n+1}] + M\Delta[(C_n)^3 - 3C_n] \\ & + B_p(F_n)C_nH(C_n), \end{aligned} \quad (7.38)$$

with the addition of the proliferation term.

## 7.4.2 Results

The domain used for most of the simulations shown is of size  $128 \times 128$ , which using the length scale is equivalent to  $160\mu\text{m} \times 160\mu\text{m}$ . As mentioned earlier in this section, the initial condition for the VEGF levels  $f$  has locations of high  $f$ -values, which represent hypoxic cells in the model. All simulations with a domain size of  $128 \times 128$  use the exact same initial condition of 50 hypoxic cells distributed over the domain.

Figure 7.3 shows a simulation over time for the control parameters given in Table 7.1. The simulation shows the initiation and progression stages of angiogenesis over a time period of 8 hours and 14 minutes (or 19 time units). While branching from growing capillaries does occur, the model favours sprouting from the initial capillary at the start. Capillaries grown from secondary

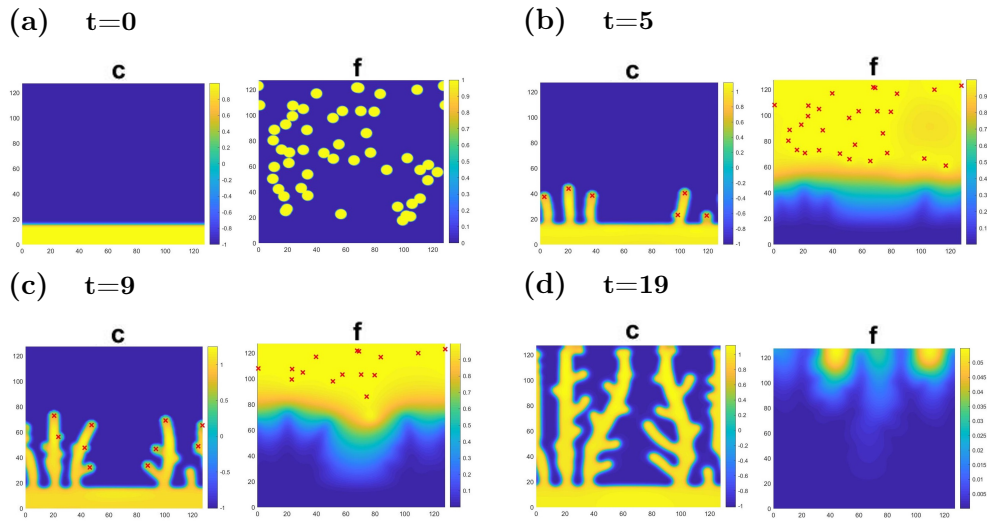


**Figure 7.3:** Simulation of Travasso's angiogenesis model on a domain of size  $128 \times 128$ , at times (a)  $t=0$ , (b)  $t=5$ , (c)  $t=9$ , and (d)  $t=19$ , with endothelium/ECM phase field parameter  $c$  on the left and VEGF levels  $f$  on the right. Parameters are as given in Table 7.1. The initial conditions represent a capillary at the bottom of the domain, and 50 randomly distributed hypoxic cells with centres indicated by the red crosses.

sprouting are not particularly long, and tertiary sprouting seems almost non-existent, even on larger domains, as seen in Figure 7.4, which shows a run on a larger domain of  $256 \times 256$ , or  $320 \times 320 \mu\text{m}$ . The total time taken for this simulation is just under 16 hours.

When the nutrient diffusion length  $f_{sat}$  is altered, the number of capillaries and the amount of branching changes. For a shorter diffusion length, some hypoxic cells previously saturated by capillaries are no longer saturated and deactivated, as the capillary is not close enough anymore. This causes additional branching as the capillaries migrate closer to deactivate the hypoxic cells. See Figure 7.5 for a simulation with a smaller  $f_{sat}$ .

Figure 7.6 shows a parametric study with the final results of nine simulations

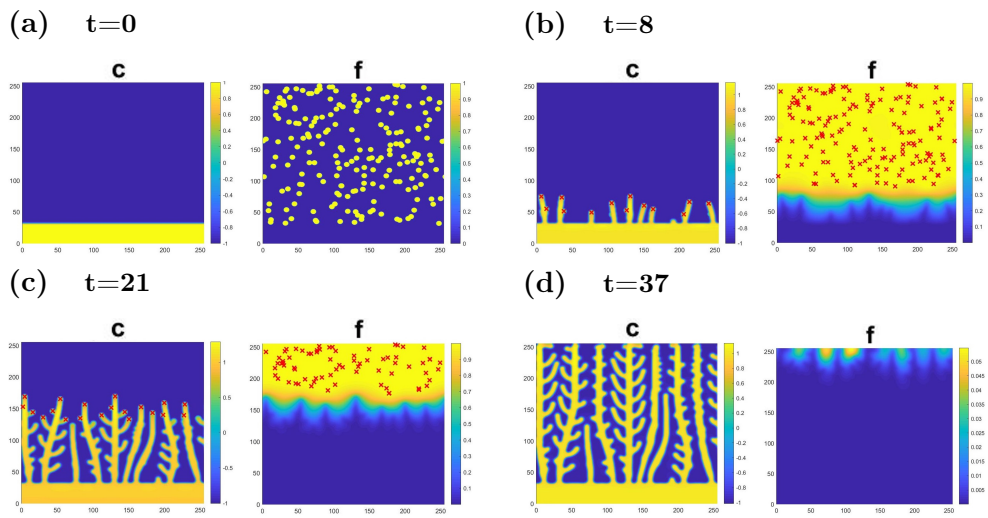


**Figure 7.4:** Simulation on a larger domain of size  $256 \times 256$ , with 200 hypoxic cells initially, at (a)  $t=0$ , (b)  $t=8$ , (c)  $t=21$ , and (d)  $t=37$ , and with parameter values from Table 7.1.

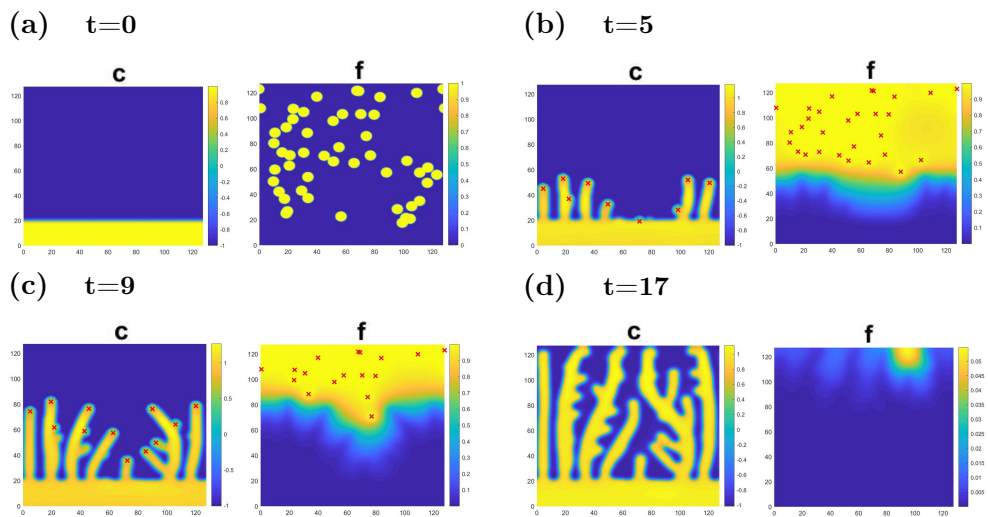


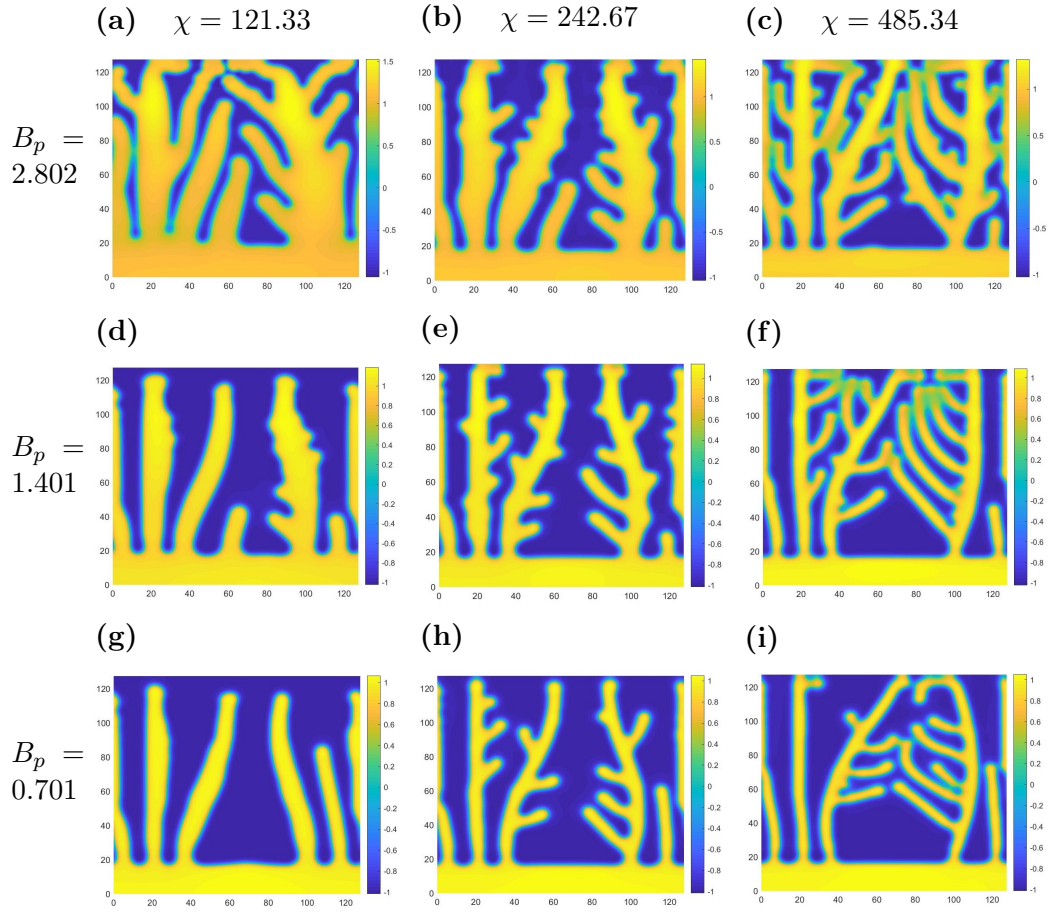
**Figure 7.5:** Simulation of the angiogenesis model with nutrient diffusion length  $f_{sat} = 10$ , at times (a)  $t=0$ , (b)  $t=5$ , (c)  $t=9$ , and (d)  $t=17$ .

when two parameters, the chemotactic constant  $\chi$  and proliferation rate  $B_p$ , are changed. The figure shows what effect changing these parameters has; increasing  $\chi$  results in thinner capillaries, as does decreasing  $B_p$ . Increasing  $\chi$  also results in longer capillaries as the TECs' higher velocity allows them to migrate further before they get deactivated, and increasing  $B_p$  results in more capillary sprouting. Therefore when both chemotaxis and proliferation are fast the capillary network is very compact and covers a lot of the domain. Parametric studies for other parameter combinations are shown in the Appendix.

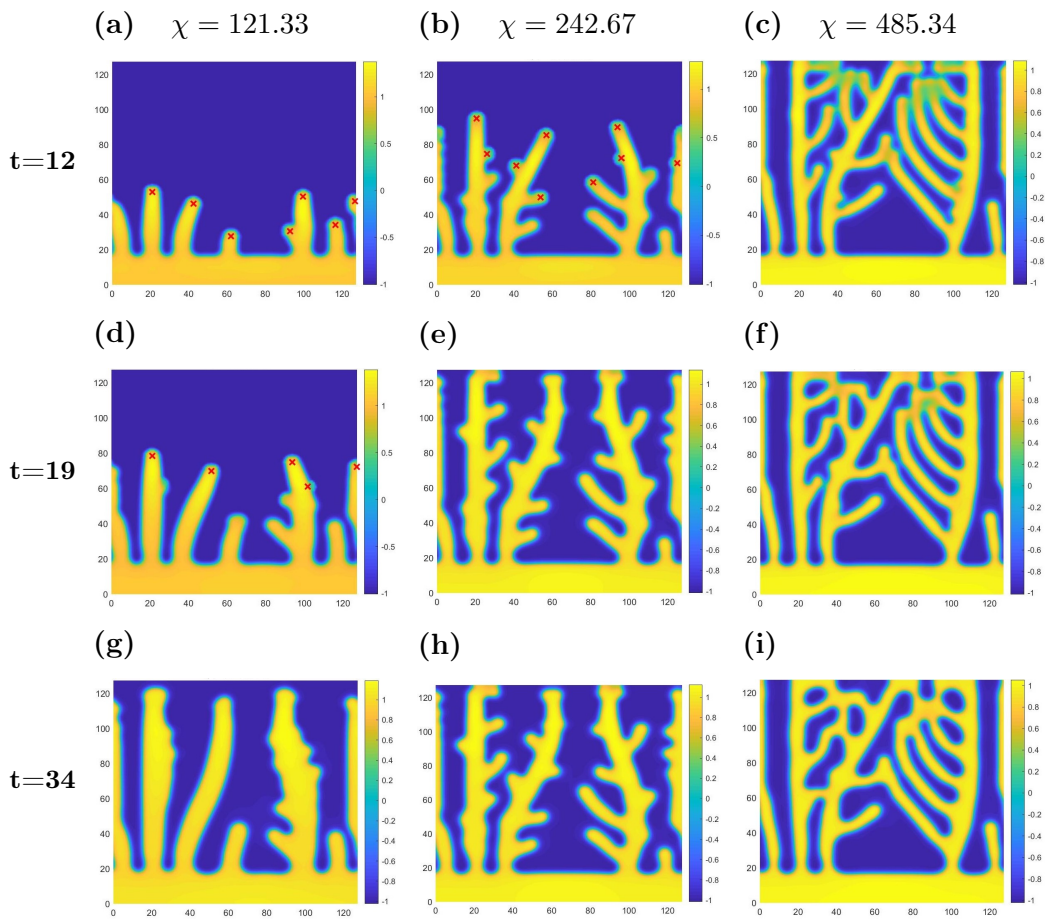
Figure 7.7 shows the results of the different values of  $\chi$  used before, but at three different time stages to see the effect  $\chi$  has on the speed of angiogenesis development. The simulation where  $\chi$  is set as half its control value of  $\chi = 242.27$  takes almost twice as long as the simulation at the control value, which takes almost twice as long as the result with double the control value.

Figure 7.8 shows the difference in the final condition when the tip endothelial cells form on the interface of the capillary instead of in the endothelium phase itself. This causes more tip cells to form. These simulations show that tip cells can be created in the interface without problems in the results, which is important as when it comes to coupling the surface Delta-Notch model to this angiogenesis model in Chapter 8, the tip cells will be formed within the phase interface.

The interfacial thickness is set as  $\lambda = 1$ . As mentioned in Section 7.3.2, the selection of  $\lambda$  is important because it needs to be large enough to make the numerical computation easier, but it needs to be small enough to make the



**Figure 7.6:** Parametric study where changes of the parameters  $\chi$  and  $B_p$  are studied. Results shown are solutions where no VEGF is left (VEGF levels have dropped below the TEC threshold  $f_{act}$  everywhere). The values of  $\chi$  for each column and  $B_p$  for each row are shown on the top and left.



**Figure 7.7:** Simulations for different values of  $\chi$  at times  $t = 12$ ,  $t = 19$ , and  $t = 34$ . See the different speeds at which the capillary networks form.

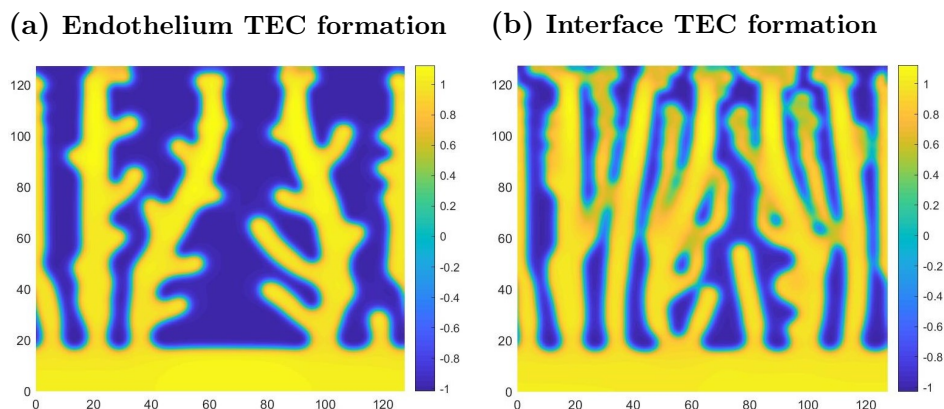


**Figure 7.8:** Final values of phase-field parameter  $c$  where **(a)** TECs form in the endothelium phase ( $c > 0.9$ ) **(b)** TECs form on the interface between the endothelium and ECM phases ( $-0.9 \leq c \leq 0.9$ ).

numerical results as accurate as possible. Figure 7.9 shows final conditions with different values of  $\lambda$ ; the results with the smallest  $\lambda$  is for  $\lambda = 0.1$ . This is clearly too small, as the thin interface has caused the phases to mix.  $\lambda = 0.5$  has no mixing, and results are very similar to the results with  $\lambda = 1$ , but the interface is not smooth, and so the mesh size is too large for this value of  $\lambda$ .  $\lambda = 2$  is also shown, with a clearly visible interface. For the selected mesh size of  $h = 1$ ,  $\lambda = 1$  has the best balance for efficiency, between not being too large and allowing the computation to run effectively. The interface thickness could be made smaller for smaller mesh sizes, but this was not investigated in this work due to long computation times.

Mesh refinement showed that a mesh size of  $h = 1$  ( $128 \times 128$  mesh points) was sufficient. Figure 7.10 shows results with different mesh sizes, and a coarser mesh of  $64 \times 64$  does not have smooth phase transition. Finer meshes do not show much improvement from  $128 \times 128$ ; however these finer meshes would allow smaller values of  $\lambda$ , as discussed above.

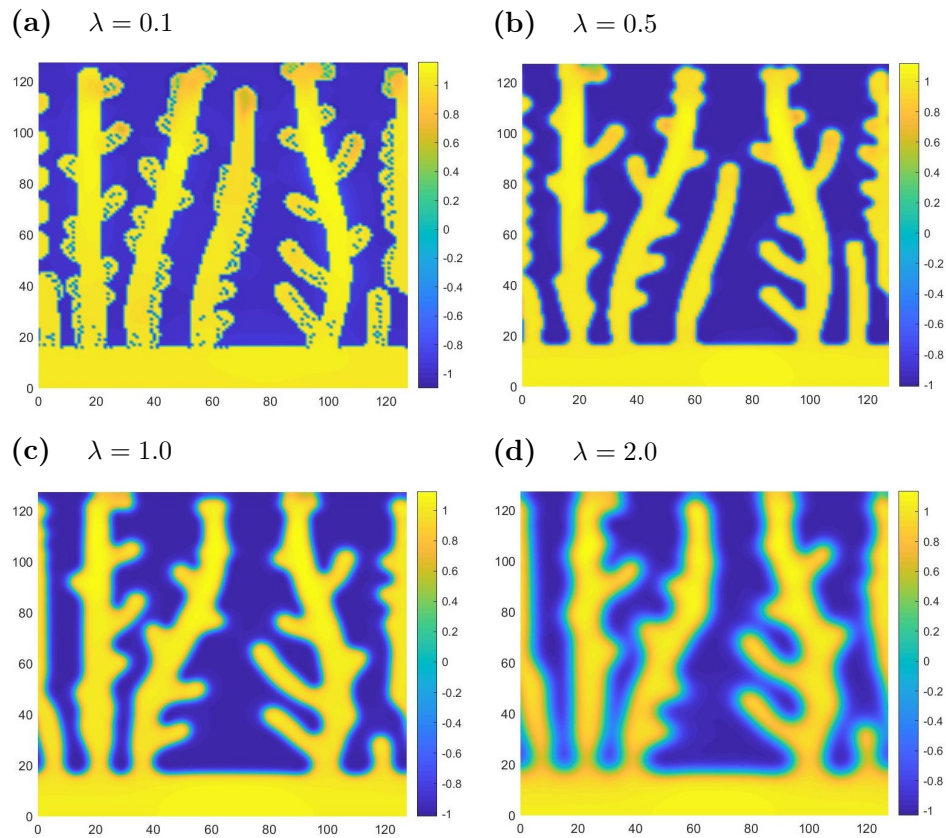


**Figure 7.9:** Simulations for different values for the phase interface thickness  $\lambda$ : (a)  $\lambda = 0.1$ , (b)  $\lambda = 0.5$ , (c)  $\lambda = 1$ , (d)  $\lambda = 2$ . Poor results are seen for  $\lambda < 1$ .

Figure 7.11 shows results with two clusters of high VEGF levels representing the release of Tumour Angiogenesis Factor (TAF) from a multifocal tumour. The domain size is  $256 \times 256$  and the size of each tumour is 80 length units, or  $100 \mu\text{m}$  in diameter, in agreement with data of TAF-releasing tumours in vivo from Folkman and Kalluri [65]. The total time of this simulation is longer at 26 and a half hours, which can be explained by the initial hypoxic cell locations being further away from the initial capillary, and when the VEGF reaches it the concentration of VEGF is still very low; thus TEC migration is initially slow. Tertiary sprouting now occurs due to the more localised

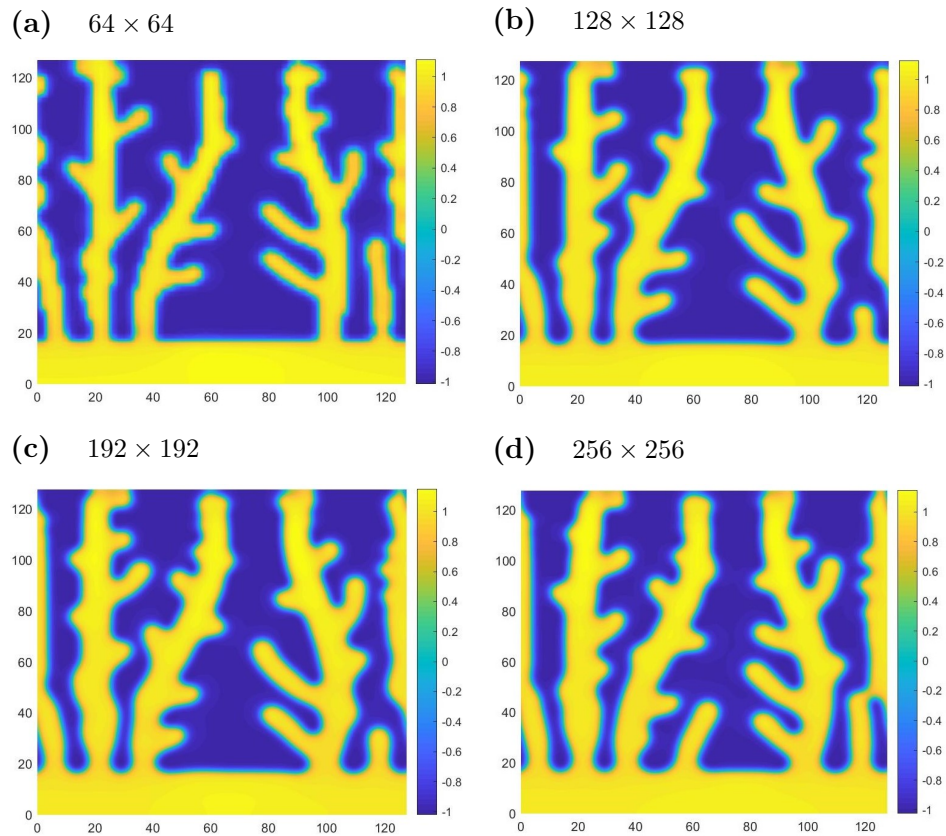


**Figure 7.10:** Simulations for the same domain size of  $128 \times 128$  units but for different mesh sizes; (a)  $h = 2$  ( $64 \times 64$  mesh points), (b)  $h = 1$  ( $128 \times 128$ ), (c)  $h = 0.667$  ( $192 \times 192$ ), (d)  $h = 0.5$  ( $256 \times 256$ ).

hypoxic areas.

## 7.5 Conclusion

This chapter has introduced the angiogenesis model by Travasso et al. [139] and produced simulations of the model. These simulations will be used to compare to simulations of the coupled model, which will be derived in Chapter 8. The model was given by a Cahn-Hilliard equation with an added reaction term for the phase variable coupled to a reaction-diffusion equation for the

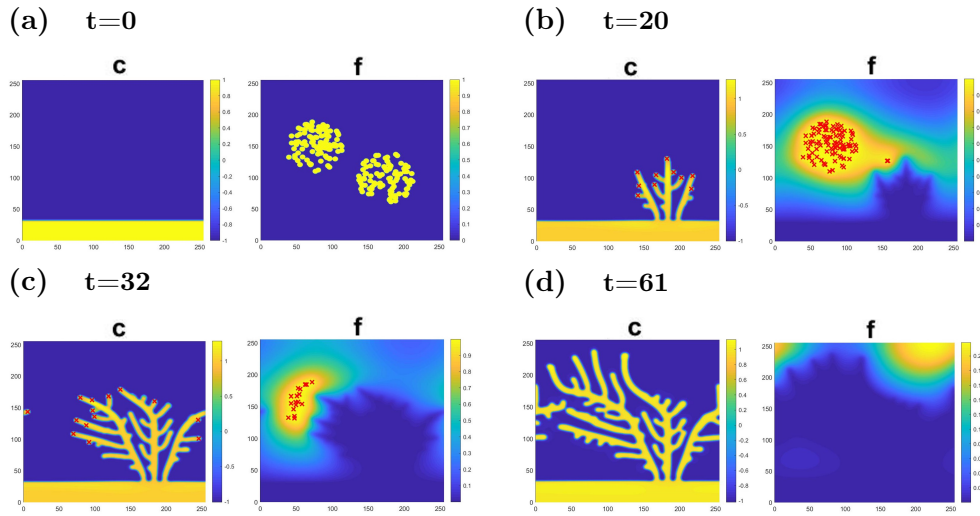


**Figure 7.11:** Simulations with two main hypoxic locations, much like a multifocal avascular tumour releasing Tumour Angiogenesis Factor (TAF), at times (a)  $t=0$ , (b)  $t=20$ , (c)  $t=32$ , and (d)  $t=61$ . Model parameters used are still given by Table 7.1. The time taken for this simulation is much longer because the angiogenic factor takes longer than normal to reach the initial capillary via diffusion.

angiogenic factor variable, and had a discrete definition for the formation of the tip cells and the hypoxic cell locations.

The diffuse interface in the model required investigation into the most appropriate value for the interface thickness  $\lambda$ . A parametric study on  $\lambda$  with a fixed mesh size of  $h = 1$  found that  $\lambda = 1$  produced the most accurate results with no numerical issues. However, this is still a large value for the interface thickness. A finer mesh would have allowed for a smaller  $\lambda$  value; however this was not pursued due to much larger computation times for finer meshes.

There are biological factors in angiogenesis that are not considered by this particular model. For example, the time between initial migration and proliferation of endothelial cells and the formation of the blood vessel lumen is ignored, which means endothelial cells that are not yet mature nutrient-

carrying blood vessels are given the ability to saturate hypoxic cells in this model, and a hypoxic cell in the model is defined as saturated as soon as the endothelium is in proximity.

Another factor overlooked by the model is related to the way tip cell inhibition is defined. In real systems the tip cell inhibition only takes effect along the capillary, not across ECM space. The mathematical model does not account for this and as a result there may be a few instances in the model where a tip cell inhibits endothelial tissue that is not of its own capillary. This also occurs in the surface lateral inhibition model, as already stated in the conclusion of Chapter 6. Another issue is that the boundary conditions of the model affect the VEGF levels in particular, as the system is closed which means if the domain is too small, the VEGF will not be able to diffuse far away. A large domain size compared to the length scale of the simulation is ideal where possible.

Avascular tumours that release TAF are still growing, and therefore more hypoxic cells are created since the start of the initiation of angiogenesis. The final condition portrayed in Figure 7.11 does not necessarily represent the final vascular structure of the tumour; as the tumour grows the new parts of the tumour will need vascularisation and will release TAF later. The fact new hypoxic areas are not created during the simulation is a limitation of this model. Coupling Travasso's model with a tumour growth model has already been achieved by Xu et al. [159], where the supply of VEGF depends on a phase-field tumour equation.

The discrete definition of the tip endothelial cells in this model is very lim-

iting, which causes rather predictable behaviour. The fixed lateral inhibition radius for each TEC means that no TECs can form within this radius, but can form just outside. There is no smooth change in the TEC formation probability which clashes with the continuous definition of the endothelium in the angiogenesis model. In the continuous lateral inhibition models, recall the triangle and smooth weight functions for lateral inhibition which would give a more continuous TEC selection process, where the areas of activated and inhibited tissue are found. The surface Delta-Notch model and the angiogenesis model have been successfully simulated and will now be combined to construct a coupled model in Chapter 8.

# Chapter 8

## A coupled lateral inhibition-angiogenesis model

### 8.1 Introduction

Chapter 7 introduced an angiogenesis model by Travasso et al. [139] that defined the tip endothelial cells and their behaviour using discrete components. In this chapter, a coupled angiogenesis-lateral inhibition model is created by using the surface lateral inhibition model calculated in Chapter 6 to replace the discrete tip endothelial cell formation in Travasso's angiogenesis model.

The ligand in angiogenesis signalling is named Delta-Like Ligand 4 (DLL4), due to its homology with Delta. While Delta exists in the fruit fly “*Drosophila melanogaster*” to determine the lateral inhibition in a number of functions, DLL4 is present in mammals and controls endothelial cell migration. The Delta-Notch model and its surface counterpart from Chapters 4 and 6 respectively are still accurate models of capillary signalling in angiogenesis. In this chapter the model will sometimes be referred to as the DLL4-Notch model.

Numerically, the models will be progressed in time together as the time scales of lateral inhibition and angiogenesis are similar. The DLL4 and Notch levels will be calculated on the surface of the capillary defined by phase field parameter  $c$  from the angiogenesis model. There will be a threshold for DLL4 levels which will trigger capillary surface migration when reached. The lateral inhibition model will then calculate the DLL4-Notch behaviour again on the updated surface.

This process reflects real-life angiogenesis; the angiogenic factor VEGF triggers the migration of cells towards the VEGF source. The sprouting pattern is caused by Notch receptors in the endothelial cells, where VEGF receptors in cells with a high level of active Notch are downregulated and these cells do not migrate.

This chapter will first introduce the equations of the fully coupled model in Section 8.2, as well as the representation of the VEGF source through discrete definitions of hypoxic cells. All the new components of the model are described. The numerical process of the coupling and the parameter values to be used are discussed in Section 8.3, and numerical results are also shown in this section. This section has a discussion of the differences between the original angiogenesis model and the coupled angiogenesis model. Section 8.4 is the conclusion, which talks further about the benefits of such a model and mentions potential for further work, as a preface to the Conclusion chapter.

## 8.2 The lateral inhibition driven angiogenesis model

This section will detail the equations used in the new coupled model, describe the parameters involved and explain the introduction of any new terms. The equations themselves are variants of the equations from Chapters 6 and 7; the surface DLL4-Notch equations and Travasso's model of angiogenesis. The newly coupled equations include a dependence of Notch on VEGF  $f$ , as well as a dependence of the endothelial tissue-ECM phase on DLL4.

### 8.2.1 The angiogenesis equations

For coupling to a set of DLL4-Notch equations, the following equations for angiogenesis are used:

$$\begin{aligned}\frac{\partial f}{\partial t} &= D\Delta f - B_u f c \mathcal{H}(c), \\ \frac{\partial c}{\partial t} &= M\Delta(\mu_c - \lambda^2 \Delta c) + B_p(f) c \mathcal{H}(c) + B_M(c, d, f).\end{aligned}\tag{8.1}$$

These equations (8.1) are similar to the equations (7.15) of the Travasso model shown in Chapter 7, with the exception of a new migration term in the phase equation to replace the discrete allocation of tip endothelial cells. The function  $\mathcal{H}(c)$  once more represents the Heaviside function and  $B_M(c, d, f)$  is a migration function dependent on phase field parameter  $c$ , DLL4 concentration  $d$ , and VEGF  $f$ . It takes the form

$$B_M(c, d, f) = \begin{cases} \mathbf{V}(f) B(c) d c \mathcal{H}(c) & \text{for } d \geq d_{act} \\ 0 & \text{for } d < d_{act}, \end{cases}\tag{8.2}$$

where the interface equation  $B(c)$  will be defined in Section 8.2.2 with the DLL4-Notch part of the model. This term only exists in the presence of a sufficient amount of DLL4; specifically when the DLL4 concentration is above a threshold  $d_{act}$ . The idea of having an activation threshold for the lateral inhibition model was briefly discussed in the conclusion of Chapter 5. In this model, presence of DLL4 can be thought of as analogous to the presence of VEGF receptors, and high Notch levels (or low DLL4 levels) represent downregulation of VEGF, which is in agreement with the role Notch receptors have in downregulating VEGF receptors in angiogenesis.

$\mathbf{V}(f)$  is the continuous equivalent of  $\mathbf{v}_{TEC}^i$  in equation (7.20) from Chapter 7:

$$\mathbf{V}(f) = \chi \nabla f \mathcal{L}(|\nabla f|), \quad (8.3)$$

based on the chemotactic constant  $\chi$ , the velocity gradient, and the limiting function

$$\mathcal{L}(|\nabla f|) = 1 + \left( \frac{G_M}{|\nabla f|} - 1 \right) \mathcal{H}(|\nabla f| - G_M). \quad (8.4)$$

The hypoxic cells, from which VEGF is secreted, are determined in the same way as before; with subdomains

$$\Omega_{HC}^l(t_{n+1}) = \{\mathbf{x} \in \Omega | \mathbf{x} - \mathbf{x}_{HC}^l | \leq R_{HC}\} \quad (8.5)$$

for cell with centre  $\mathbf{x}_{HC}^l$ , and deactivation of a hypoxic cell if

$$|\mathbf{x}_{HC}^l - \mathbf{x}| < f_{sat} \quad (8.6)$$

and  $c(\mathbf{x}) > c_{act}$ . The  $f$ -values inside the subdomains are once again set as  $f_{HC}^i = f_{HC}$ .

## 8.2.2 The DLL4-Notch equations

The DLL4-Notch equations suggested are

$$\begin{aligned} B(c) \frac{\partial n}{\partial t} + V \cdot \nabla(B(c)n) &= B(c)F_B(\bar{d}_B) - (B(c) + \delta)n, \\ B(c) \frac{\partial d}{\partial t} + V \cdot \nabla(B(c)d) &= \nu(B(c)G(n) - (B(c) + \delta)d), \end{aligned} \quad (8.7)$$

$$F_B(x) = \frac{A_1 x^p}{(B(c)a(f))^p + x^p}, \quad G(x) = \frac{A_2 b^q}{b^q + x^q},$$

where  $V$  is the velocity of the interface and

$$\bar{u}_B(\mathbf{x}, t) = \int_{-\infty}^{\infty} B(c(\mathbf{x} - s))w(s)u(\mathbf{x} - s, t)ds. \quad (8.8)$$

These equations are slightly modified versions of the surface Delta-Notch equations in Chapter 6, where  $B(c)$  takes the form

$$B(c) = (c + 1)^2(c - 1)^2, \quad (8.9)$$

which was mentioned briefly in Chapter 6, equation (6.3), to satisfy the condition that  $B(c) \neq 0$  on the phase interface only.

The variable  $n$  depends on the presence of VEGF  $f$  through the VEGF function  $a(f)$  found in the Hill function  $F_B$ , much like the VEGF function first defined in Chapter 4, equation (4.39) to localise the pattern of Delta and Notch. The VEGF function is set as  $a(f) = a_p f$  for VEGF-Notch reaction parameter  $a_p$ .

The difference in the endothelial cell size  $R_{EC}$  and the inhibition length  $\delta_4$  from those used in Chapter 6 will affect the form of the weight function. A

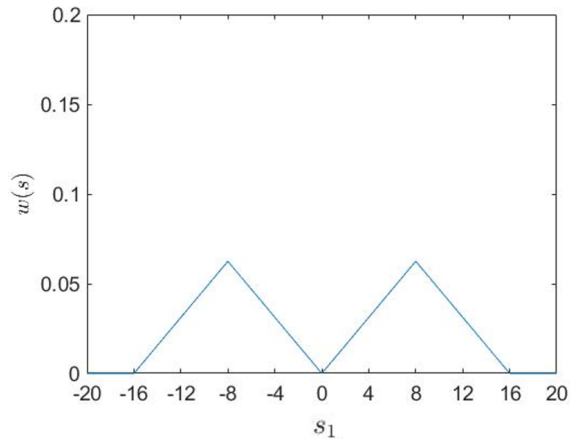


**Figure 8.1:** Cross section of the 2D triangle weight function (8.10) for the coupled angiogenesis model. Notice the larger number of  $s$ -values that are now assigned a weight, as a result of the selection of the new radius  $R_{EC} = 4$  and inhibition radius  $\delta_4 = 16$ .

2D triangle weight function is used in the coupled angiogenesis model, which is written

$$w(\mathbf{s}) = \begin{cases} \frac{2|\mathbf{s}|}{\delta_4^2} & |\mathbf{s}| \leq \frac{\delta_4}{2}, \\ \frac{2(\delta_4 - |\mathbf{s}|)}{\delta_4^2} & \frac{\delta_4}{2} < |\mathbf{s}| \leq \delta_4 \\ 0 & \text{otherwise,} \end{cases} \quad (8.10)$$

where  $R_{EC} = 4$  and  $\delta_4 = 16$ , is displayed in Figure 8.1.

### 8.3 Simulating the coupled model

There are two ways to advance the time in the model. One way is to use a multiscale approach where DLL4 and Notch are calculated on the surface  $c = 0$  (given by the initial condition for the phase field  $c$ ) and the lateral inhibition model is then advanced on its own. The angiogenesis equations will be advanced once a threshold for DLL4 is passed. The VEGF levels and phase field parameter will be updated, and the lateral inhibition will be calculated

on this new interface. This method means the interface is treated as fixed in the case of the lateral inhibition equations, and the lateral inhibition time scale is instantaneous compared to the angiogenesis time scale.

However, as stated by Wearing et al. [150], the time scale for the lateral inhibition model ranges from hours to days, and Chapter 7 established that the time scale for the angiogenesis model on a  $160\mu\text{m} \times 160\mu\text{m}$  domain is eight hours. Therefore, evolving the two sets of equations in successive timesteps is more appropriate. Using this staggered approach, and starting with the initial conditions for DLL4  $D_0$ , Notch  $N_0$ , phase parameter  $C_0$  and VEGF  $F_0$ , the equations are evolved from timestep  $s$  to  $s + 1$  as follows:

Step 1: Use values  $D_s$ ,  $N_s$ ,  $C_s$  and  $F_s$  in the angiogenesis equations (8.1) to find

$$C_{s+1} \text{ and } F_{s+1}$$

Step 2: Use values  $C_{s+1}$ ,  $F_{s+1}$ ,  $D_s$  and  $N_s$  in the DLL4-Notch equations (8.7) to

$$\text{find } D_{s+1} \text{ and } N_{s+1}$$

Step 3: Repeat with  $s = s + 1$  until no hypoxic cells remain.

The coupling of these models will introduce a delay to the pattern formation in the DLL4-Notch model, as the initial condition for VEGF will cause the VEGF function  $a(f)$  to correspond to a stable solution at the surface initially and the pattern will only begin to form later when VEGF diffuses to the surface. An important question to be considered is whether this delay will cause any qualitative difference in the results. However, Veflingstad et al. [142] witnessed no change in the final solution of their Delta-Notch model with a delay and the only effect witnessed was the time elapsed before reaching the final solution. Once the hypoxic sources of VEGF are deactivated,  $a(f)$  will drop again at the surface and the DLL4 levels will fall and cease surface motion.

Another delay in the model relating to the time DLL4 takes to appear and activate tip cells is discussed later in this chapter (see Figure 8.4).

For the simulations of the coupled model, tip cells will only be allowed to form on the interface of the capillary to make the coupling with the surface lateral inhibition calculations possible. Chapter 7 showed that the behaviour when tip cells form on the interface causes more initial sprouting than when they form within the endothelium, but the behaviour is still typical of angiogenesis (see Figure 7.8).

The lateral inhibition model (8.7) uses the 2D triangle weight function (8.10) in all simulations.

### 8.3.1 Parameter values

Many of the parameter values used in the angiogenesis model in Chapter 7 are also used here and should be assumed the same except the ones given a different value here, or where specified different later in Section 8.3.2 due to a parametric study. The length and time scales are unchanged from Chapter 7. Parameters from the angiogenesis equations that take a different control value here to that taken in Chapter 7 are the radius of the initial capillary, which is taken as  $R_V = 8$ , and the two interfacial thicknesses which are changed to  $\lambda = 2$  and  $\epsilon = 0.2$  to regulate the large fluctuations in the DLL4 and Notch values near the moving interface when the interface thickness is too small, as mentioned previously in Chapter 6. The new parameter for tip cell activation,  $d_{act}$ , is dimensionless and set at  $d_{act} = 0.25$ . The length and time scales, and all angiogenesis parameters, are given in Table 8.1. As the DLL4-Notch model is dimensionless, all the parameters are too, and are set the same

as in Chapter 6, except the VEGF parameter  $a_p$  which is set as  $a_p = 0.4$  so that at the activation threshold  $d_{act} = 0.25$ , the VEGF function  $a(f) = 0.1$ . The lateral inhibition parameters are given in Table 8.2.

### 8.3.2 Results

The results here intend to show that the coupled angiogenesis model (8.1), (8.7) is comparable to the behaviour of tip cell selection and branching in angiogenesis. The convex splitting method used for Travasso's angiogenesis model in Chapter 7 is also used for the coupled model here, with an explicit method to simulate the DLL4-Notch equations. Boundary conditions are set the same as in Chapter 7, with periodic boundary conditions horizontally and symmetric Neumann boundary conditions vertically. The initial condition set in Chapter 7, Figure 7.3(a) is used here for better comparison of the two models, with locations of  $f(\mathbf{x}, 0) = f_{HC}$  to represent hypoxic cells, and an initial capillary at the bottom of the domain, of thickness  $2R_V$ . The initial conditions for DLL4 and Notch sets Notch at its base solution everywhere and DLL4 as a small perturbation of its base solution. For the DLL4 and Notch parameter values given in Table 8.2, the initial conditions are set as

$$n_0 = n_e \approx 0.24, \quad d_0 = d_e + \tilde{d} \approx 0.07 + \tilde{d}, \quad (8.11)$$

for random perturbation  $\tilde{d} \in [0, 0.1]$ , where the base solutions  $n_e, d_e$  are approximated with  $a(f) = 0.1$ . These particular initial conditions are selected to allow the DLL4 and Notch patterns to emerge faster, as the values start to converge to the base states  $n_e, d_e$  before the pattern starts to form.

The simulation of the coupled angiogenesis model using the parameter values

Parameter	Symbol	Real value	Dimensionless value
Length scale	$L$	$1.25 \mu\text{m}$	1
Time scale	$T$	1560s	1
Diffusion coefficient of $f$	$D$	$10^{-1} \mu\text{m}^2 \text{s}^{-1}$	100
Mobility coefficient of $c$	$M$	$10^{-3} \mu\text{m}^2 \text{s}^{-1}$	1
Tip endothelial cell radius	$R_{EC}$	$5 \mu\text{m}$	4
Hypoxic cell radius	$R_{HC}$	$5 \mu\text{m}$	4
Radius of the initial capillary	$R_V$	$10 \mu\text{m}$	8
Uptake rate of VEGF	$B_u$	$0.004 \text{s}^{-1}$	6.25
Proliferative rate of ECs	$B_p$	$8.981 \times 10^{-4} \text{s}^{-1}$	1.401
Range of lateral inhibition	$\delta_4$	$20 \mu\text{m}$	16
Nutrient diffusion length	$f_{sat}$	$25 \mu\text{m}$	20
TEC threshold for EC phase	$c_{act}$	N/A	0.9
VEGF level in hypoxic cells	$f_{HC}$	N/A	1
TEC VEGF threshold	$f_{act}$	N/A	0.055
VEGF cap on EC proliferation	$f_p$	N/A	0.3
TEC VEGF gradient threshold	$G_{act}$	$0.008 \mu\text{m}^{-1}$	0.01
VEGF gradient cap on velocity	$G_M$	$0.024 \mu\text{m}^{-1}$	0.03
Chemotactic constant	$\chi$	$14.583 \mu\text{m}^2 \text{s}^{-1}$	242.67
TEC DLL4 level threshold	$d_{act}$	N/A	0.25
Interfacial width for continuous equations	$\lambda$	$2.5 \mu\text{m}$	2
Interfacial width for discrete component approximation	$\epsilon$	$0.25 \mu\text{m}$	0.2

**Table 8.1:** Dimensional and dimensionless values of the length and time scales of the coupled model, and the parameters from the angiogenesis equations.

Parameter	Symbol	Real value	Dimensionless value
VEGF-Notch reaction coefficient	$a_p$	N/A	0.4
Hill function parameter in $g$	$b$	N/A	0.1
Exponent for $f$	$p$	N/A	3
Exponent for $g$	$q$	N/A	3
DLL4-Notch ratio	$\nu$	N/A	1
Hill function coefficient for $f$	$A_1$	N/A	1
Hill function coefficient for $g$	$A_2$	N/A	1

**Table 8.2:** Dimensionless values of the parameters from the surface DLL4-Notch equations of the coupled model.

given in Tables 8.1 and 8.2 gives values for the angiogenesis and DLL4-Notch variables as shown in Figures 8.2 and 8.3 respectively. Notice that the time elapsed until all hypoxic cells are deactivated is longer due to the new delay caused by the presence of the DLL4-Notch model. The activation of Notch by DLL4 in surrounding tissue inhibits tip endothelial cells close to existing ones. Tip endothelial cells can easily be identified in Figure 8.3(c) as the locations with high DLL4 levels.

The method of tip endothelial cell activation greatly differs from other angiogenesis models which use discrete methods for TEC allocation. While Travasso's angiogenesis model treats the activation of TECs as instantaneous once the VEGF conditions are met, here the VEGF activates the DLL4-Notch patterning, which has a threshold for endothelial cell migration. This delay means the VEGF released from the hypoxic cells has diffused across the ECM and has reached more of the original capillary surface before migration starts. Therefore more tip cells emerge along the original capillary than in

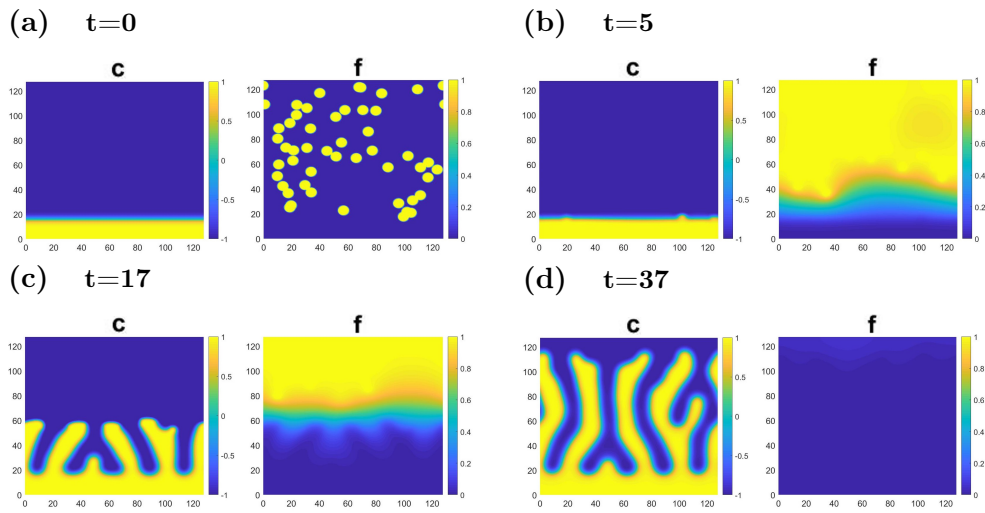


**Figure 8.2:** Phase field parameter  $c$  and VEGF  $f$  values from simulations of the coupled angiogenesis model with DLL4-Notch tip cell selection at times (a)  $t=0$ , (b)  $t=5$ , (c)  $t=17$ , and (d)  $t=37$ , with parameter values as given in Tables 8.1 and 8.2. The initial condition for VEGF is the same as the initial condition used in Chapter 7 for most simulations of Travasso’s angiogenesis model (see Figure 7.3). The times indicate that the pattern takes around 16 hours to reach the final solution shown in (d).

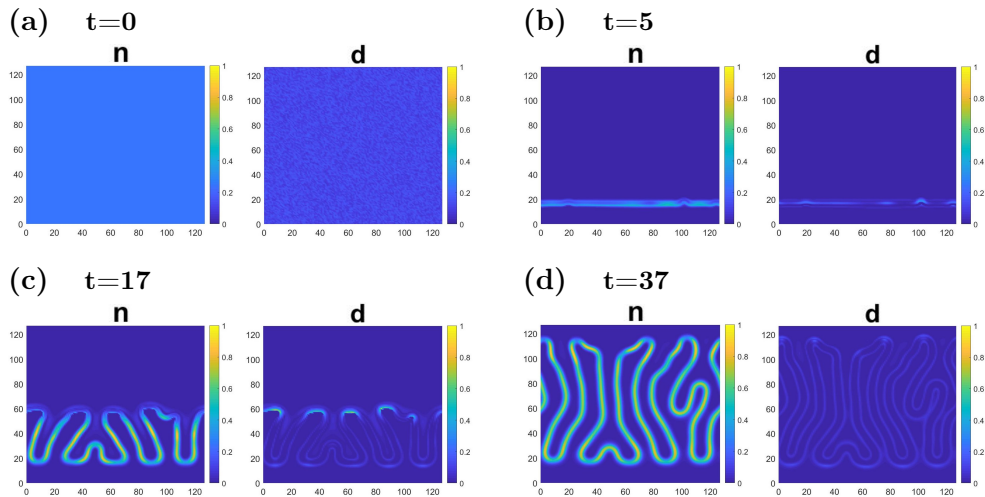


**Figure 8.3:** Notch  $n$  and DLL4  $d$  values which correspond to the results for  $c$  and  $f$  in Figure 8.2, at times (a)  $t=0$ , (b)  $t=5$ , (c)  $t=17$ , and (d)  $t=37$ .

the Travasso model, which had new capillaries emerge earlier and therefore hypoxic cells begin to deactivate earlier.

Figure 8.4 shows results where VEGF evolution is paused while the lateral inhibition pattern is emerging, to be able to more accurately compare the results to those from Chapter 7. This is accomplished by setting the VEGF values equal to those of the previous timestep. The periods where VEGF evolution is paused are controlled by the DLL4 concentration on the interface; when the TEC threshold,  $d_{act}$ , is reached on the interface, the VEGF equations are activated again. The results here are more similar to those from Chapter 7, with more branching and a lower number of tip cells forming from the original capillary compared to Figure 8.2. The rest of the simulations discussed in this chapter return to the original simulation, and VEGF evolution is no longer paused.

When the nutrient diffusion length  $f_{sat}$  is reduced and there is a need for capillaries to migrate closer to hypoxic cells before they are deactivated, more branching is expected, as seen earlier for the non-coupled model in Chapter 7, Figure 7.5. The time taken is shorter as the capillaries get closer to hypoxic cells without deactivating them and cause the VEGF gradient to be higher. This makes chemotaxis of the TECs towards the hypoxic cells faster, TECs will advance quicker and thus the angiogenesis process as a whole will be quicker. Figure 8.5 shows such results with lower diffusion length  $f_{sat}$ .

A parametric study similar to the one shown in Chapter 7, Figure 7.6 is shown in Figure 8.6. The chemotactic constant  $\chi$  and the proliferation rate  $B_p$  are the parameters varied once again, and the results seen are similar to those in

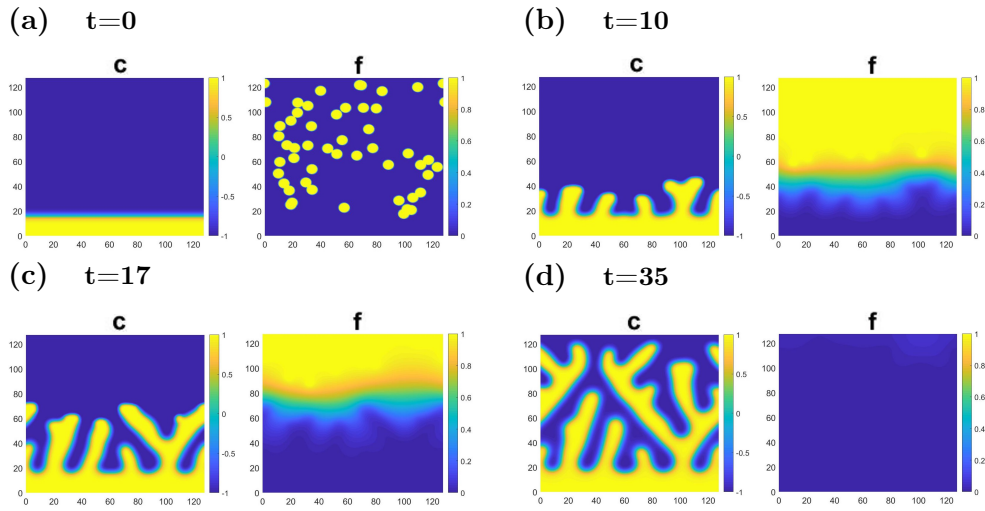


**Figure 8.4:**  $c$  and  $f$  values in a simulation where VEGF evolution is temporarily paused until the DLL4-Notch solutions on the capillary surface are stable. This is done to compare the results of this model to the results from Chapter 7. The time elapsed is close to the original solution in Figure 8.2, with (a)  $t=0$ , (b)  $t=10$ , (c)  $t=17$ , and (d)  $t=35$ .

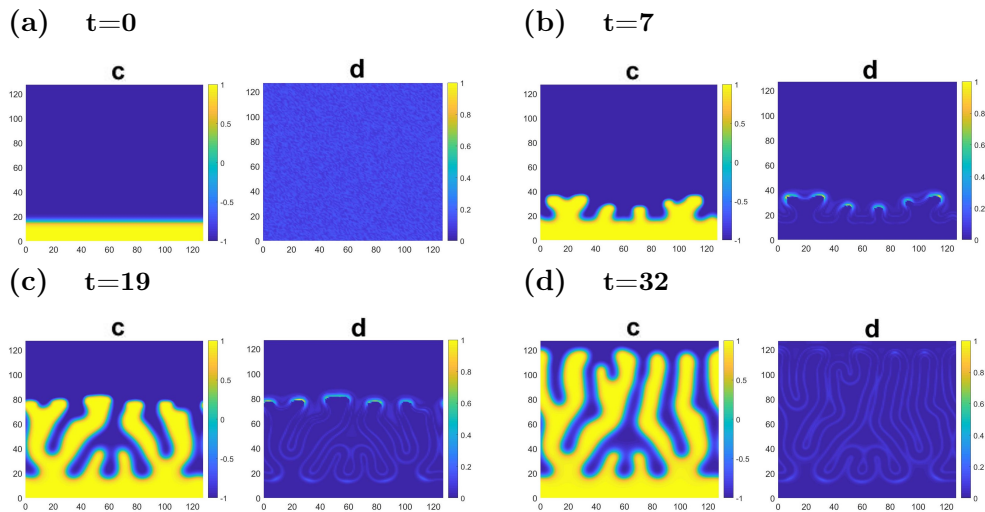


**Figure 8.5:** Results of phase field parameter  $c$  and DLL4 levels  $d$  with a shorter nutrient diffusion distance  $f_{sat} = 10$ , which causes more branching and a more crowded domain. Times are (a)  $t=0$ , (b)  $t=7$ , (c)  $t=19$ , and (d)  $t=32$ .

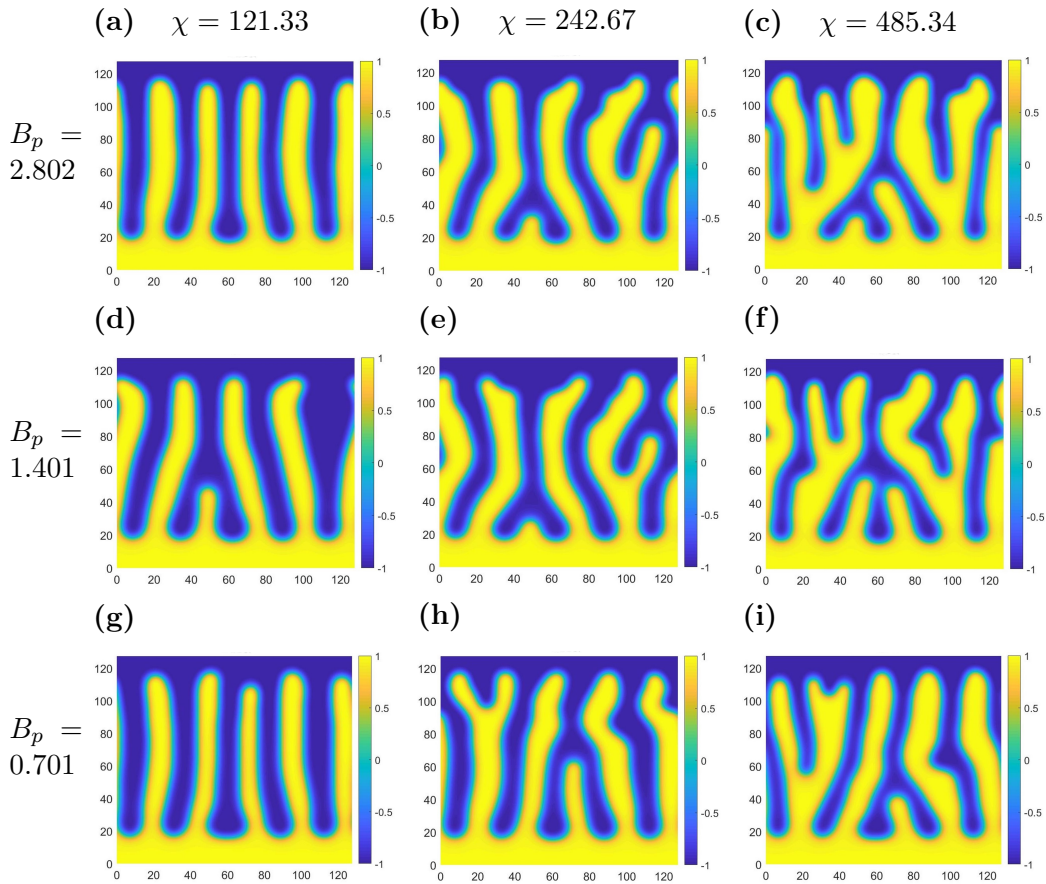


**Figure 8.6:** Parametric study for  $\chi$  and  $B_p$ , which shows final solutions for nine different parameter settings. The values of  $\chi$  for each column and  $B_p$  for each row are shown on the top and left. All other parameters are set at the values given in Tables 8.1 and 8.2. The results vary in capillary thickness and the amount of branching.

Figure 7.6; an increase in  $B_p$  causes thicker capillaries, and a more complex network of capillaries is again observed for high  $B_p$  and  $\chi$ . However, higher  $\chi$  does not give faster capillary formation or thinner capillaries for this model. This may be due to the spatial uniformity of the VEGF levels, which will increase the proliferation along the capillary stalk but also decrease the gradient of VEGF and consequently the TEC velocity.

A simulation for the case where a tumour represented by two clusters of hypoxic cells is present is shown in Figures 8.7 and 8.8. Comparing to the tumour simulation in Chapter 7 Figure 7.11, the main differences in the coupled version which stand out are the increased amount of time taken, which is caused by the delay as discussed earlier, the lower number of capillaries, and the reduced amount of branching. However, the tumour simulation for the coupled model still shows more branching than in all previous runs of the coupled model with scattered hypoxic locations.

## 8.4 Conclusion

It has been shown in this chapter that a continuous model of lateral inhibition signalling can be coupled to an angiogenesis model to provide a novel way of simulating the onset of angiogenesis. The simulations show that sensible results are achieved for appropriate parameter values and unstable solutions to inhomogeneous perturbations in the DLL4-Notch model.

There is a lot more research to be conducted on this topic. The numerical results from Section 8.3 study changes in parameters related to the angiogenesis equations but the coupling to the DLL4-Notch model involves more parameters that also need investigating. For instance, studies on the effect of the Hill function parameters may yield interesting results, but care must be taken to not choose parameters that cause the DLL4-Notch pattern to no longer form. The VEGF function could be investigated and given a different form to  $a(f) = a_p f$ , although such a suitable form is currently elusive.

Many other biological mechanisms have been ignored for ease of simulation,

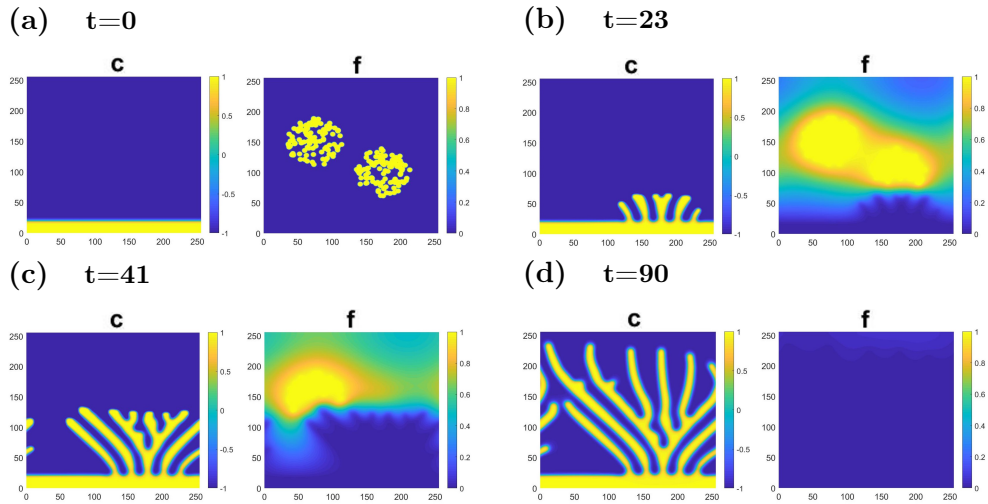


**Figure 8.7:** Results of  $c$  and  $f$  on a  $256 \times 256$  domain with two large hypoxic regions resembling a multifocal tumour, at times (a)  $t=0$ , (b)  $t=23$ , (c)  $t=41$ , (d)  $t=90$ , using parameter values from Tables 8.1 and 8.2.

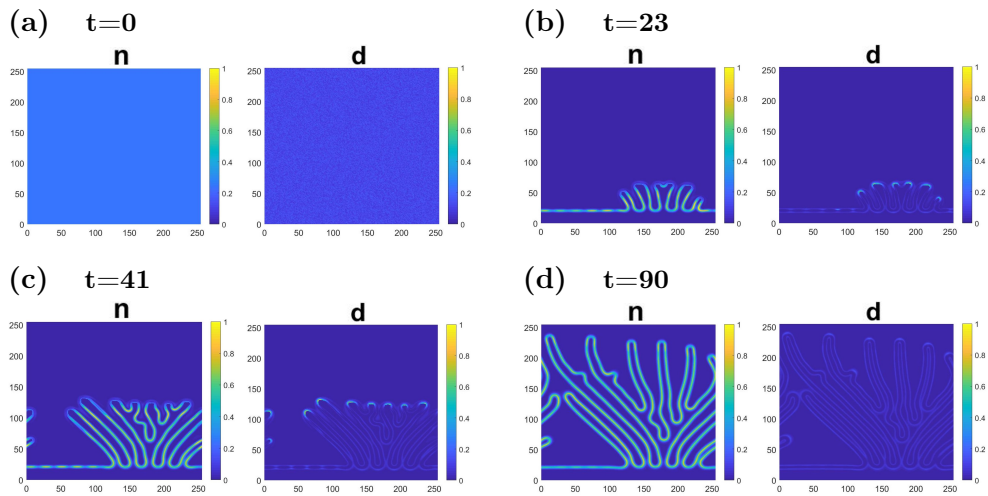


**Figure 8.8:** Notch and DLL4 values of the same simulation as shown in Figure 8.7 of a multifocal tumour, at times (a)  $t=0$ , (b)  $t=23$ , (c)  $t=41$ , (d)  $t=90$ .

but could be implemented. The time scale for the whole angiogenic process is different to the time scales seen in this model as many individual processes are not considered, such as formation of the lumens within the capillaries and diffusion of oxygen from the capillaries into the hypoxic tissue.

The DLL4-Notch model used here is the continuous version of Collier's Delta-Notch model [45] introduced in Chapter 4 and later defined on a surface in Chapter 6, Section 6.3.2. Another area not explored here is the use of the continuous Delta-Notch model introduced in Chapter 5, which was an extension of Collier's model developed by Owen and Sherratt [117].

The model would improve with a faster and more stable numerical method. While convex splitting was used to stabilise the Cahn-Hilliard equation, the DLL4-Notch equations used an explicit method which meant the timestep could not be set too large. As stated in the conclusion of Chapter 6, the surface equations would benefit from a time adaptive scheme which depends on the velocity of the capillary surface. A faster numerical method would also allow a finer mesh to be used, which would allow a smaller interface thickness to be set than the current thickness of  $\lambda = 2$ . Another area for improvement would be the computation of the nonlocal term in the Notch equation (8.7)<sub>1</sub>. The calculation of the nonlocal term was improved, but it remains time-expensive and further work on the numerical efficiency of this model is required.

The model is still not fully continuous due to the discrete setting of the hypoxic cell locations which act as a source for VEGF. However, a fully continuous model is possible through a source term in the VEGF equation. Introduction

of such a source term in the Travasso model has already been demonstrated with success by Xu et al. [159], where the source term depends on a tumour variable defined by its own equation. The only discrete part of the model used by Xu et al. involves the tip endothelial cells, which means their model can be combined with this chapter's lateral inhibition-driven angiogenesis model to produce a fully continuous model for angiogenesis.

Coupling to a full tumour growth model is possible, and should not be too challenging once a VEGF source term is introduced as detailed above, and the model is fully continuous. Both avascular and vascular stages of tumour growth are able to be simulated with the addition of this model, with TAF being released from hypoxic tumour tissue which is present once the tumour has grown to a particular size. The vascular network will saturate the hypoxic tissue when close enough and will encourage the further growth of the tumour.

Antiangiogenesis therapies are a rising treatment for tumours; so much so that mathematical models on such therapies are becoming increasingly popular. Many models of angiogenesis have been extended to include a drug which restricts angiogenesis (see Cai et al. [37]) but the possibility of antiangiogenesis therapies taking advantage of the link between Notch signalling and angiogenesis has still not been fully explored. Future work may involve research into the effects of a drug that increases Notch potency of DLL4 inhibition or of VEGF-R downregulation.

The main objective of the thesis has been reached in this chapter. There are many applications of this model now available and many improvements and extensions to the model can be made.

# Chapter 9

## Conclusion

The aims of this thesis were to create a continuous mathematical model of lateral inhibition and to couple it to a model of angiogenesis. These were to be accomplished using the objectives:

1. To develop a continuous model for lateral inhibition cell signalling by redefining the way the lateral inhibition is implemented in existing cell signalling models, in order to avoid using fixed cell locations and to model average signalling based on average cell distributions instead
2. To extend the continuous lateral inhibition model to include extra biological features
3. To simulate the cell signalling model on a surface using a surface approximation method
4. To study a hybrid model for angiogenesis that uses discrete cell signalling components
5. To successfully couple the continuous cell signalling model to the angiogenesis model and use the coupled model to simulate the activation

of angiogenesis in both healthy conditions and cases where a tumour is present.

After the Introductory Chapter 1, the biological background of the research was explored in Chapter 2. This chapter included a discussion of cancer and how it develops, as well as background information on angiogenesis and the Notch signalling that occurs during the onset of angiogenesis. It was explained that the reason cancer is so unpredictable and uncontrollable is because it is able to become self sufficient in everything it needs, and overcome cell signals that control abnormal cell activity. To do this, cancer cells acquire certain abilities, named by Hanahan and Weinberg as the Hallmarks of Cancer [80].

One important hallmark required for malignant growth is a tumour's ability to induce angiogenesis, so that it is able to gain its own blood supply. Angiogenesis is activated in endothelial cells of nearby blood vessels by angiogenic factors, such as Vascular Endothelial Growth Factor (VEGF), which bind to VEGF receptors in the endothelial cells and promote migration of the cells towards the VEGF source. Notch signalling between endothelial cells ensures that not all cells are activated for migration, where a ligand named Delta-Like Ligand 4 (DLL4) binds to Notch receptors in adjacent cells, which prevent VEGF binding in their own cell, so that there are rarely neighbouring cells that are both activated for migration.

Chapter 3 discussed the history of mathematical models related to the work in this thesis. Existing models of cell signalling and angiogenesis were mentioned, and the concept of phase field modelling, that has already been used to simulate many processes including angiogenesis ([139, 144]), was introduced. This chapter highlighted a significant gap in the literature; most existing an-

giogenesis models, such as the model by Travasso et al. [139], use discrete rules to allow some cells to become tip (migratory) cells and prevent their neighbours from exhibiting this same migratory behaviour. These discrete rules often assume a lot of information about the cells, such as unanimous sizes and shapes. A continuous model of lateral inhibition used to replace these discrete rules would remove assumptions on the information about the cells, and would represent averages of the ligand and receptor levels instead.

Such a continuous model of lateral inhibition was derived in Chapter 4 from a discrete model by Collier et al. [45]. An extended version of this Collier model was derived by Owen and Sherratt [117], and a continuous version was simulated in Chapter 5. The average neighbour function which represents the juxtacrine cell signalling in the model had to be redefined to better resemble the average signalling of a range of possible cell distributions. Results were found for the model in Chapter 4 in both one and two dimensions, and the models from both Chapters 4 and 5 included results which simulated conditions similar to the behaviour observed in angiogenesis, where the pattern only emerges in one area due to the localised presence of the angiogenic factor VEGF. This was achieved with the use of a VEGF function to replace the parameter  $a$ , which varied the stability of the model over space.

The model from Chapter 4 only included the minimum features required in a cell signalling model. The extended model in Chapter 5 had more detail but still omitted some biological mechanisms, such as the intracellular processes that play a vital role in cell signalling. The first model was acceptable for producing the results desired in this work, but models such as the model from Chapter 5 that include more information can be used if particular mechanisms

wish to be considered.

The lateral inhibition models from Chapters 4 and 5 were defined in Cartesian coordinates and were not dependent on a surface, which will be required for coupling to the angiogenesis model as the model will need to be able to work along an interface that will represent a moving capillary. Chapter 6 rectified this by using a phase-field surface approximation method to reproduce the first model from Chapter 4 on a given surface, where a phase field  $\phi$  represented the surface at  $\phi = 0.5$ , and the surface was assigned a thickness  $\epsilon$ . The approximation method defined the variables over a whole two-dimensional domain and used a function  $B(\phi)$  that was non-zero on the interface only to define the model on the interface. The accuracy of this phase field approximation method was analysed using an asymptotic analysis to prove the model reduces to the regular surface model when the interface thickness  $\epsilon \rightarrow 0$ .

The results of the surface lateral inhibition model simulated conditions on stationary and moving interfaces. Results for a moving interface were as expected on the interface when the constant  $\omega$  proportional to the velocity was not too large. A suitable value for the interface thickness must be chosen to avoid inaccuracies further away from the interface. A Runge-Kutta scheme may also improve these numerical issues. A feature of the surface method that was addressed in Chapter 6 is that parts of the interface that are not considered adjacent to each other may still inhibit each other if they are close enough, caused by the fact the equations technically exist across the whole domain. This is also a feature of the Travasso angiogenesis model [139], but in the Travasso model tip cells cannot be inhibited as they are already tip cells. A threshold for migratory endothelial tissue could be introduced in the

coupled angiogenesis model so that if endothelial tissue meets the threshold, it is not inhibited.

The angiogenesis model to be coupled to the surface lateral inhibition model was introduced in Chapter 7. The model was a hybrid model of angiogenesis by Travasso et al. [139], where the angiogenic factor source and the tip endothelial cells were represented by discrete components, and the other dynamics of the model were represented by a Cahn-Hilliard equation with a reaction term for the phase field  $c$  and a reaction-diffusion equation for the angiogenic factor  $f$ . Results simulated both physiological and pathological angiogenesis by adjusting the locations of angiogenic factor sources, where a tumour was imitated by setting the initial condition as a cluster of hypoxic cells.

The results for the Travasso model were largely used to investigate parameter changes in the model, such as the proliferation and uptake rates, the chemotactic constant, and the nutrient diffusion length. The interfacial thickness  $\lambda$  was also trialled to find its optimal value. Results mainly showed a small amount of branching from the original capillary and secondary branches sprouting from these new capillaries, with possible variation in density of the vascular system or capillary thickness depending on the parameter values. The results which started with clusters of hypoxic cells saw focused vascular growth around those areas, as expected from the presence of a TAF-releasing tumour.

The assignment of the TECs in the Travasso model used discrete definitions to assign the centre of a TEC from the VEGF levels  $f$ , defined the domain of this new TEC from the fixed TEC radius, and inhibited other points within

an inhibition radius from being designated a TEC centre. The complication of coupling the discrete TEC and hypoxic cell components to the continuous equations of the model can slow down the computation and makes further coupling harder.

The replacement of this discrete TEC selection method with a continuous model of lateral inhibition in the angiogenesis model was executed in Chapter 8. The surface lateral inhibition model from Chapter 6 was coupled to Travasso's angiogenesis model from Chapter 7 by including a migration term  $B_M(c, d, f)$  dependent on DLL4  $d$  in the phase field  $c$  equation of the angiogenesis model, and a VEGF function  $a(f)$  dependent on angiogenic factor  $f$  in the Hill function  $F_B(\bar{d}_B)$  from the Notch  $n$  equation of the lateral inhibition model.

Results for the coupled model showed less branching than the Travasso model, which was caused by the removal of the forced TEC allocation where a TEC would always form immediately when the conditions were met. There was a delay in the coupled model caused by the time taken for the DLL4-Notch pattern to form. Time scales of Notch signalling models [150] and the previous angiogenesis model support this delay, and suggest a similar time scale for both of these processes. The reason the delay resulted in less vessel branching in the coupled model was because of the near-uniform angiogenic factor levels this caused.

The signalling of endothelial tissue across the extracellular matrix is present in the angiogenesis models from both Chapters 7 and 8, but Travasso's model in Chapter 7 does not inhibit endothelium that is already designated a tip

cell. This is why two tip cells can meet and combine in the model, a process that is called anastomosis in real life angiogenesis. This is not frequently observed in the coupled model of Chapter 8, but could be introduced through the migration term  $B_M(c, d, f)$ . If this term is not equal to zero then the tissue could be labelled “migratory” and be made immune to inhibition.

Both angiogenesis models from Chapters 7 and 8 unrealistically assume instant creation of fully functioning blood vessels as soon as the endothelial cells have migrated, where the endothelial phase in the model is able to saturate and deactivate hypoxic cells instantly when near enough. A development on the coupled angiogenesis model therefore could include the later stages of angiogenesis, where a model could simulate the formation of a lumen and perhaps even the remodelling of the vascular system.

As in Chapter 7, Chapter 8 also used different hypoxic cell locations, defined discretely, to simulate physiological and pathological angiogenesis, where a cluster of hypoxic cells resembled the presence of a tumour. Coupling fully to a tumour growth model, where the tumour is affected by the presence of the blood vessels as well as the converse, and the release of TAF from the tumour replaces the need for the discrete hypoxic cell components, is discussed in more detail later in Section 9.1.1.

Another aim of the thesis was to demonstrate the benefits of replacing the discrete rules for lateral inhibition in the angiogenesis model with the continuous lateral inhibition model. Information on the endothelial cells in the model is not known, and by using this continuous average representation of the ligand and receptor levels, no information is assumed about the cells to match this.

Coupling to the angiogenesis model also took away the assumptions on cell information made by the discrete TEC components of this model.

## 9.1 Potential for Future Work

Further work on the content of this thesis may come in many forms, such as additions to the model, changes, or numerical improvements. Some potential future work has already been mentioned earlier in this chapter.

The weight functions derived in Chapter 4, Section 4.3.2 were calculated by averaging different types of standard weight functions such as rectangle functions and Dirac delta functions. However, most of the weight functions derived were not used in the final coupled model in Chapter 8. Results comparing simulations that implement these different weight functions may produce interesting results.

The continuous model in Chapter 5 included many mechanisms of cell signalling, such as production of free receptors, and internalisation of bound ligand-receptor complexes. However, further extensions to a lateral inhibition model suggested by Wearing et al. could consider the movement of ligands and receptors on the surface of the cell (cell polarisation), unequal distribution of receptors on the cell membrane, or even cleavage from the cell altogether and the occurrence of paracrine signalling [150].

An assumption made by the angiogenesis models from Chapters 7 and 8, as mentioned earlier in this chapter, is that the differentiation and maturation stages of angiogenesis are instantaneous. The fact that the endothelial

phase can instantly deliver nutrient to nearby hypoxic areas in the model is unrealistic, as the formation of the capillary lumens, which are the passages through which the nutrient-carrying blood travels, occurs after the progression stage where the endothelial cells migrate and proliferate. Mathematical models exist that include the differentiation and maturation stages of angiogenesis [22]. The model also ignores the remodelling stage of angiogenesis, where ineffective blood vessels are pruned to improve efficiency of the vascular system. Remodelling is more complicated to implement, as decisions on pruning depend on the blood flow of the model, as demonstrated in a model by Owen et al. [119]. The coupled angiogenesis model could be extended to incorporate some or all of these states of angiogenesis.

The two-dimensional results of the Delta-Notch model in Chapter 4 could be used for another extension to this work. The model could be applied to a three-dimensional model of angiogenesis, where the two-dimensional Delta-Notch model is simulated on the now-2D capillary surface. This 3D model will give a more in-depth simulation of angiogenesis.

Another important application that was not covered is drug delivery, in particular antiangiogenic therapies. Examples of some of these therapies include those that target existing vasculature and cause vascular collapse, and those that target proliferating endothelial cells early in angiogenesis [119]. The latter therapies in particular provide interesting ideas for the application of the coupled lateral inhibition-angiogenesis model, where perhaps therapies that target the Notch signalling can be investigated.

### 9.1.1 Application to a tumour growth model

An area of research that was briefly investigated in this work was tumour angiogenesis. Chapters 7 and 8 both investigate results with an initial condition of a cluster of hypoxic cells to imitate the release of angiogenic factor from a tumour, but tumour growth itself was not included. A fully continuous model of tumour growth and angiogenesis could be developed by extending the coupled angiogenesis model, where the avascular, vascularisation, and vascular stages of tumour growth can be simulated at once.

A model by Xu et al. [159], mentioned briefly in the Conclusion of Chapter 8, altered the Travasso model to replace the discrete hypoxic cell components for the angiogenic factor source by coupling the model to a tumour growth model, where the angiogenesis equations would become

$$\begin{aligned}\frac{\partial f}{\partial t} &= D\Delta f - B_u f c \mathcal{H}(c) + \varphi(1-f)G(\sigma), \\ \frac{\partial c}{\partial t} &= M\Delta(\mu_c - \lambda^2 \Delta c) + B_p(f)c \mathcal{H}(c),\end{aligned}\tag{9.1}$$

where  $\varphi$  is a phase field variable representing the density of tumour cells and  $\sigma$  is the nutrient variable, both with their own separate equations, and  $G(\sigma)$  is some function of the nutrient  $\sigma$ . Xu et al. mention that the only feature keeping their model from being fully continuous is the discrete components for TEC selection. The coupled model from Chapter 8 has successfully removed these discrete rules for the phase field parameter  $c$ , and can be coupled to the Xu model to create a completely continuous model with angiogenesis

equations

$$\begin{aligned}\frac{\partial f}{\partial t} &= D\Delta f - B_u f c \mathcal{H}(c) + \varphi(1-f)G(\sigma), \\ \frac{\partial c}{\partial t} &= M\Delta(\mu_c - \lambda^2 \Delta c) + B_p(f)c\mathcal{H}(c) + B_M(c, d, f).\end{aligned}\tag{9.2}$$

This tumour growth model could potentially be extended further by examining the point when the tumour tissue begins to invade some healthy tissue phase, and is henceforth defined as cancer. The model may be able to simulate tumour invasion by activating an invasion ability in the tumour when it surpasses some parameter related to the growth, which will likely only happen in the presence of high nutrient levels, and therefore show that the model supports the fact that angiogenesis is required for cancer to develop.

## 9.2 Final thoughts

This thesis has provided the first coupling of a continuous model of lateral inhibition to an angiogenesis model. In my opinion, one of the most important potential areas of future research that was not accomplished in this work was the extension of the angiogenesis model to include later stages of angiogenesis, in particular the inclusion of lumen formation and diffusion of nutrient only able to originate from fully functioning blood vessels with a lumen. This could be implemented by including an extra “lumen” phase which emerges in the middle of a vessel once it reaches a certain thickness. Another important future development, which was an original aim when work on this thesis began, is coupling the angiogenesis model to the angiogenesis-tumour growth model by Xu et al. [159] discussed in Section 9.1.1.

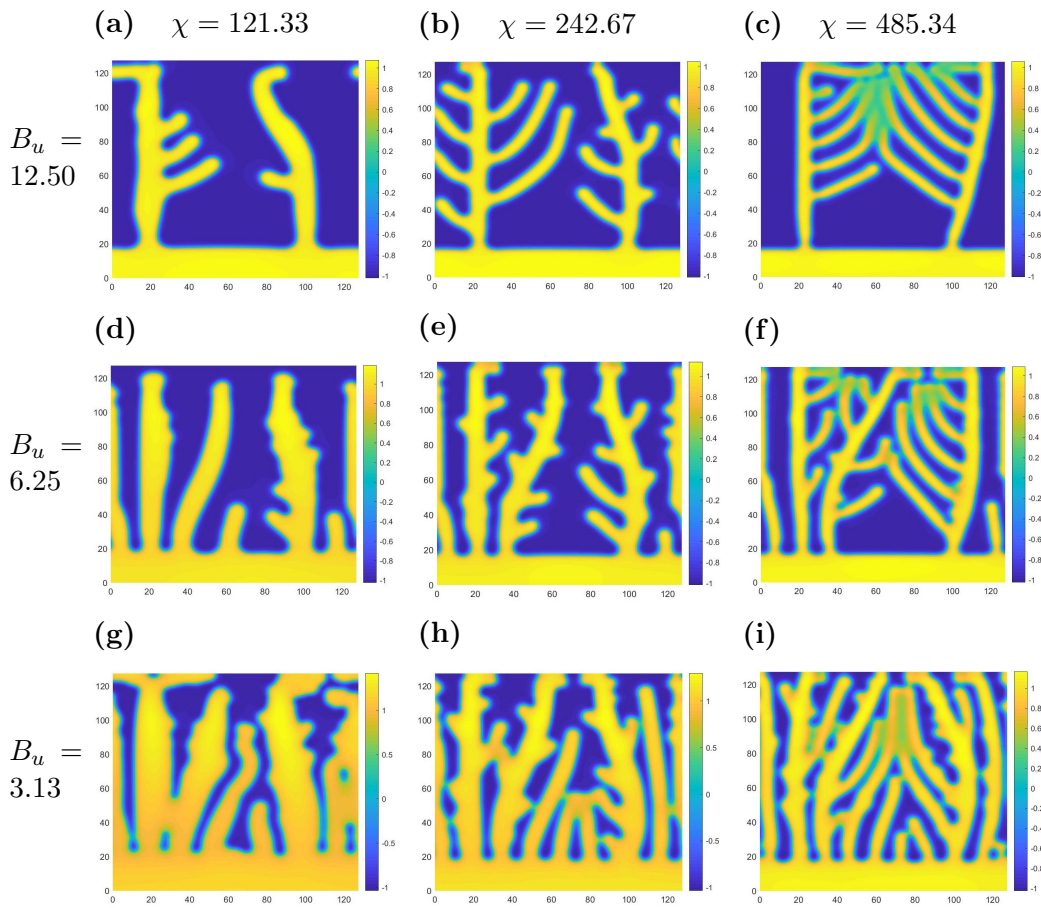
The Delta-Notch model also has many further applications outside of angiogenesis, for example the role of Delta and Notch in cell differentiation, which occurs in cell generation processes such as gliogenesis (the generation of glial cells, which support the nervous system) [128], and the angiogenesis model itself can also be used to simulate other uses of angiogenesis. I believe that the applications of the ideas developed in this thesis are vast.

# Appendix

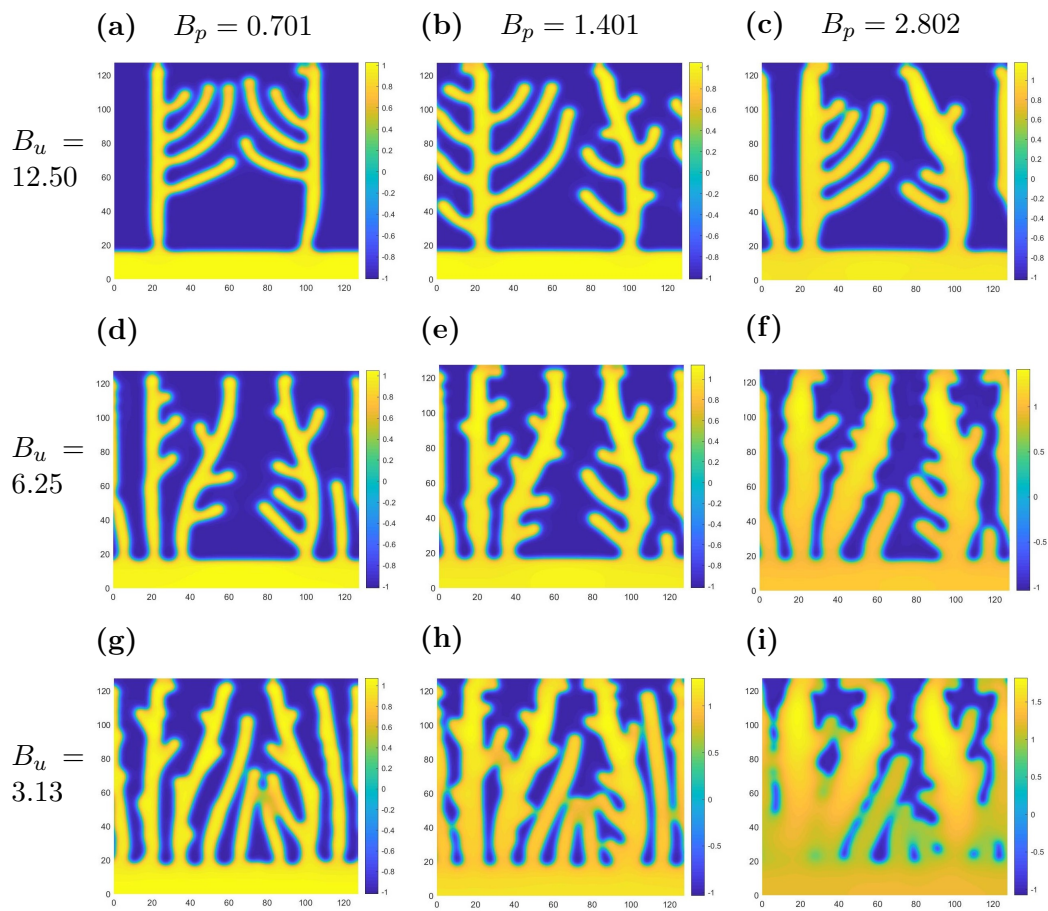
## A.1 Parameter studies for the angiogenesis model from Chapter 7

Figure 9.1 is a parametric study of the chemotactic constant of TECs  $\chi$  and the uptake rate of angiogenic factor,  $B_u$ . Lower  $B_u$  and higher  $\chi$  shows a compact vascular system. The faster consumption of angiogenic factor by the endothelial cells has a similar result to slower proliferation, seen earlier in Figure 7.6.

Figure 9.2 shows a change of the proliferation rate  $B_p$  and the uptake rate  $B_u$  together. High  $B_p$  and low  $B_u$  results in a denser vascular system than the other results. Both high  $B_p$  and low  $B_u$  result in thicker capillaries, but higher  $B_p$  has more of an effect on capillary thickness. A higher uptake rate results in a lower number of capillaries because the number of TECs activated is lower from the angiogenic factor levels dropping below the TEC threshold quicker.



**Figure 9.1:** A parametric study where changes of parameters  $\chi$  and  $B_u$  are studied.



**Figure 9.2:** Parametric study where changes of parameters  $B_p$  and  $B_u$  are studied.

# Bibliography

- [1] B Addison-Smith, DLS McElwain, and Philip K Maini. A simple mechanistic model of sprout spacing in tumour-associated angiogenesis. *Journal of theoretical biology*, 250(1):1–15, 2008.
- [2] Samuel M Allen and John W Cahn. A microscopic theory for antiphase boundary motion and its application to antiphase domain coarsening. *Acta Metallurgica*, 27(6):1085–1095, 1979.
- [3] Alexander RA Anderson and MAJ Chaplain. Continuous and discrete mathematical models of tumor-induced angiogenesis. *Bulletin of mathematical biology*, 60(5):857–899, 1998.
- [4] ARA Anderson and Mark AJ Chaplain. A mathematical model for capillary network formation in the absence of endothelial cell proliferation. *Applied mathematics letters*, 11(3):109–114, 1998.
- [5] ARA Anderson, MAJ Chaplain, C Garcia-Reimbert, and CA Vargas. A gradient-driven mathematical model of antiangiogenesis. *Mathematical and computer modelling*, 32(10):1141–1152, 2000.
- [6] ARA Anderson, MAJ Chaplain, EL Newman, RJC Steele, and AM Thompson. Mathematical modelling of tumour invasion and

- metastasis. *Computational and Mathematical Methods in Medicine*, 2 (2):129–154, 2000.
- [7] Pervin Anklesaria, Joaquin Teixido, Marikki Laiho, Jacalyn H Pierce, Joel S Greenberger, and Joan Massague. Cell-cell adhesion mediated by binding of membrane-anchored transforming growth factor alpha to epidermal growth factor receptors promotes cell proliferation. *Proceedings of the National Academy of Sciences*, 87(9):3289–3293, 1990.
- [8] RP Araujo and DLS McElwain. A history of the study of solid tumour growth: the contribution of mathematical modelling. *Bulletin of mathematical biology*, 66(5):1039–1091, 2004.
- [9] R.P. Araujo and D.L.S. McElwain. New insights into vascular collapse and growth dynamics in solid tumors. *Journal of Theoretical Biology*, 228(3):335 – 346, 2004. ISSN 0022-5193.
- [10] Peter Armitage and Richard Doll. The age distribution of cancer and a multi-stage theory of carcinogenesis. *British journal of cancer*, 8(1): 1, 1954.
- [11] D Balding and DLS McElwain. A mathematical model of tumour-induced capillary growth. *Journal of theoretical biology*, 114 (1):53–73, 1985.
- [12] Amy L Bauer, Trachette L Jackson, and Yi Jiang. A cell-based model exhibiting branching and anastomosis during tumor-induced angiogenesis. *Biophysical journal*, 92(9):3105–3121, 2007.
- [13] Holly Bednarz, Andrea Shaw, Sophie West, and Divya Radhakrishnan Nair. Evolution of a cancer- lecture notes.

[http://sphweb.bumc.bu.edu/otlt/mph-modules/ph/ph709\\_cancer/PH709\\_Cancer5.html](http://sphweb.bumc.bu.edu/otlt/mph-modules/ph/ph709_cancer/PH709_Cancer5.html). Accessed: June 2017.

- [14] Katie Bentley, Holger Gerhardt, and Paul A Bates. Agent-based simulation of notch-mediated tip cell selection in angiogenic sprout initialisation. *Journal of theoretical biology*, 250(1):25–36, 2008.
- [15] Katie Bentley, Giovanni Mariggi, Holger Gerhardt, and Paul A Bates. Tipping the balance: robustness of tip cell selection, migration and fusion in angiogenesis. *PLoS computational biology*, 5(10), 2009.
- [16] Marcelo Bertalmío, Li-Tien Cheng, Stanley Osher, and Guillermo Sapiro. Variational problems and partial differential equations on implicit surfaces. *Journal of Computational Physics*, 174(2):759–780, 2001.
- [17] Alessandro Bertuzzi and Alberto Gandolfi. Cell kinetics in a tumour cord. *Journal of theoretical biology*, 204(4):587–599, 2000.
- [18] Alessandro Bertuzzi, Antonio Fasano, Alberto Gandolfi, and Dorian Marangi. Cell kinetics in tumour cords studied by a model with variable cell cycle length. *Mathematical biosciences*, 177:103–125, 2002.
- [19] Alessandro Bertuzzi, Alberto D’Onofrio, Antonio Fasano, and Alberto Gandolfi. Regression and regrowth of tumour cords following single-dose anticancer treatment. *Bulletin of mathematical biology*, 65(5):903–931, 2003.
- [20] Neil A Bhowmick, Eric G Neilson, and Harold L Moses. Stromal fibroblasts in cancer initiation and progression. *Nature*, 432(7015):332–337, 2004.

- [21] J Michael Bishop and Robert Allan Weinberg. *Scientific American molecular oncology*. Scientific American, 1996.
- [22] Sonja EM Boas and Roeland MH Merks. Synergy of cell–cell repulsion and vacuolation in a computational model of lumen formation. *Journal of The Royal Society Interface*, 11(92):20131049, 2014.
- [23] Victoria Bolós, Joaquin Grego-Bessa, and José Luis de la Pompa. Notch signaling in development and cancer. *Endocrine reviews*, 28(3): 339–363, 2007.
- [24] Paul Bornstein. Thrombospondins function as regulators of angiogenesis. *Journal of cell communication and signaling*, 3(3-4): 189–200, 2009.
- [25] CJW Breward, HM Byrne, and CE Lewis. The role of cell-cell interactions in a two-phase model for avascular tumour growth. *Journal of Mathematical Biology*, 45(2):125–152, 2002.
- [26] C.J.W. Breward, H.M. Byrne, and C.E. Lewis. A multiphase model describing vascular tumour growth. *Bulletin of Mathematical Biology*, 65:609–640, 2003.
- [27] BA Bryan and PA d’Amore. What tangled webs they weave: Rho-gtpase control of angiogenesis. *Cellular and molecular life sciences*, 64(16):2053–2065, 2007.
- [28] Tracy M Bryan and Thomas R Cech. Telomerase and the maintenance of chromosome ends. *Current opinion in cell biology*, 11(3):318–324, 1999.

- [29] Deborah L Burkhart and Julien Sage. Cellular mechanisms of tumour suppression by the retinoblastoma gene. *Nature Reviews Cancer*, 8(9): 671–682, 2008.
- [30] Alan C Burton. Rate of growth of solid tumours as a problem of diffusion. *Growth*, 30(2):157–176, 1966.
- [31] Federico Bussolino, Alberto Mantovani, and Graziella Persico. Molecular mechanisms of blood vessel formation. *Trends in biochemical sciences*, 22(7):251–254, 1997.
- [32] HM Byrne and MAJ Chaplain. Growth of nonnecrotic tumors in the presence and absence of inhibitors. *Mathematical biosciences*, 130(2): 151–181, 1995.
- [33] HM Byrne and MAJ Chaplain. Necrosis and apoptosis: distinct cell loss mechanisms in a mathematical model of avascular tumour growth. *Computational and Mathematical Methods in Medicine*, 1(3):223–235, 1998.
- [34] HM Byrne, T Alarcon, MR Owen, SD Webb, and PK Maini. Modelling aspects of cancer dynamics: a review. *Philosophical Transactions of the Royal Society of London A: Mathematical, Physical and Engineering Sciences*, 364(1843):1563–1578, 2006.
- [35] G Caginalp. Stefan and hele-shaw type models as asymptotic limits of the phase-field equations. *Physical Review A*, 39(11):5887, 1989.
- [36] John W Cahn and John E Hilliard. Free energy of a nonuniform system. i. interfacial free energy. *The Journal of chemical physics*, 28(2):258–267, 1958.

- [37] Yan Cai, Shixiong Xu, Jie Wu, and Quan Long. Coupled modelling of tumour angiogenesis, tumour growth and blood perfusion. *Journal of Theoretical Biology*, 279(1):90–101, 2011.
- [38] Aurélie Carlier, Liesbet Geris, Katie Bentley, Geert Carmeliet, Peter Carmeliet, and Hans Van Oosterwyck. Mosaic: a multiscale model of osteogenesis and sprouting angiogenesis with lateral inhibition of endothelial cells. *PLoS computational biology*, 8(10), 2012.
- [39] Mark Chaplain and Alexander Anderson. Mathematical modelling of tumour-induced angiogenesis: network growth and structure. In *Angiogenesis in Brain Tumors*, pages 51–75. Springer, 2004.
- [40] Mark AJ Chaplain, Steven R McDougall, and ARA Anderson. Mathematical modeling of tumor-induced angiogenesis. *Annu. Rev. Biomed. Eng.*, 8:233–257, 2006.
- [41] Nikki Cheng, Neil A Bhowmick, Anna Chytil, Agnieszka E Gorksa, Kimberly A Brown, Rebecca Muraoka, Carlos L Arteaga, Eric G Neilson, Simon W Hayward, and Harold L Moses. Loss of  $\text{tgf-}\beta$  type ii receptor in fibroblasts promotes mammary carcinoma growth and invasion through upregulation of  $\text{tgf-}\alpha$ -, msp- and hgf-mediated signaling networks. *Oncogene*, 24(32):5053–5068, 2005.
- [42] Nikki Cheng, Anna Chytil, Yu Shyr, Alison Joly, and Harold L Moses. Transforming growth factor- $\beta$  signaling-deficient fibroblasts enhance hepatocyte growth factor signaling in mammary carcinoma cells to promote scattering and invasion. *Molecular Cancer Research*, 6(10): 1521–1533, 2008.

- [43] Michael Cohen, Marios Georgiou, Nicola L Stevenson, Mark Miodownik, and Buzz Baum. Dynamic filopodia transmit intermittent delta-notch signaling to drive pattern refinement during lateral inhibition. *Developmental cell*, 19(1):78–89, 2010.
- [44] Roie Cohen, Liat Amir-Zilberstein, Micha Hersch, Shiran Woland, Shahar Taiber, Fumio Matsuzaki, Sven Bergmann, Karen B Avraham, and David Sprinzak. Shear forces drive precise patterning of hair cells in the mammalian inner ear. *bioRxiv*, page 707422, 2019.
- [45] Joanne R Collier, Nicholas AM Monk, Philip K Maini, and Julian H Lewis. Pattern formation by lateral inhibition with feedback: a mathematical model of delta-notch intercellular signalling. *Journal of Theoretical Biology*, 183(4):429–446, 1996.
- [46] Joseph B Collins and Herbert Levine. Diffuse interface model of diffusion-limited crystal growth. *Physical Review B*, 31(9):6119, 1985.
- [47] Geoffrey M Cooper, Robert E Hausman, and Robert E Hausman. *The cell: a molecular approach*, volume 10. ASM press Washington, DC, 2000.
- [48] Anusuya Das, Douglas Lauffenburger, Harry Asada, and Roger D Kamm. A hybrid continuum–discrete modelling approach to predict and control angiogenesis: analysis of combinatorial growth factor and matrix effects on vessel-sprouting morphology. *Philosophical Transactions of the Royal Society of London A: Mathematical, Physical and Engineering Sciences*, 368(1921):2937–2960, 2010.
- [49] AS Deakin. Model for initial vascular patterns in melanoma transplants. *Growth*, 40(2):191–201, 1976.

- [50] Luisa A DiPietro. Angiogenesis and scar formation in healing wounds. *Current opinion in rheumatology*, 25(1):87–91, 2013.
- [51] Valentin Djonov, Oliver Baum, and Peter H Burri. Vascular remodeling by intussusceptive angiogenesis. *Cell and tissue research*, 314(1):107–117, 2003.
- [52] Richard Doll and A Bradford Hill. Smoking and carcinoma of the lung. *British medical journal*, 2(4682):739, 1950.
- [53] G Paolo Dotto and Anil K Rustgi. Squamous cell cancers: a unified perspective on biology and genetics. *Cancer cell*, 29(5):622–637, 2016.
- [54] Qiang Du, Chun Liu, Rolf Ryham, and Xiaoqiang Wang. A phase field formulation of the willmore problem. *Nonlinearity*, 18(3):1249, 2005.
- [55] Michael J Duffy, Naoise C Synnott, and John Crown. Mutant p53 as a target for cancer treatment. *European Journal of Cancer*, 83:258–265, 2017.
- [56] Manuel Ehling, Susanne Adams, Rui Benedito, and Ralf H Adams. Notch controls retinal blood vessel maturation and quiescence. *Development*, 140(14):3051–3061, 2013.
- [57] Lee M Ellis and Daniel J Hicklin. Vegf-targeted therapy: mechanisms of anti-tumour activity. *Nature reviews cancer*, 8(8):579–591, 2008.
- [58] David J Eyre. An unconditionally stable one-step scheme for gradient systems. *Unpublished article*, pages 1–15, 1998.
- [59] Ilker Y Eyüpoglu, Nirjhar Hore, Andreas Merkel, Rolf Buslei, Michael Buchfelder, and Nicolai Savaskan. Supra-complete surgery via dual

- intraoperative visualization approach (diva) prolongs patient survival in glioblastoma. *Oncotarget*, 7(18):25755, 2016.
- [60] Paul C Fife. *Dynamics of internal layers and diffusive interfaces*, volume 53. SIAM, 1988.
- [61] George J Fix. Phase field methods for free boundary problems. 1982.
- [62] Judah Folkman. Tumor angiogenesis: therapeutic implications. *New England journal of medicine*, 285(21):1182–1186, 1971.
- [63] Judah Folkman. Role of angiogenesis in tumor growth and metastasis. In *Seminars in oncology*, volume 29, pages 15–18. Elsevier, 2002.
- [64] Judah Folkman, Ezio Merler, Charles Abernathy, and Gretchen Williams. Isolation of a tumor factor responsible for angiogenesis. *Journal of Experimental Medicine*, 133(2):275–288, 1971.
- [65] U Folkman and R Kalluri. Beginning of angiogenesis research. *Holland-frei cancer medicine*, 2003.
- [66] LJCR Foulds. The experimental study of tumor progression: a review. *Cancer research*, 14(5):327–339, 1954.
- [67] Linnea C Franssen, Tommaso Lorenzi, Andrew EF Burgess, and Mark AJ Chaplain. A mathematical framework for modelling the metastatic spread of cancer. *Bulletin of mathematical biology*, 81(6):1965–2010, 2019.
- [68] Sarah Gebb and Troy Stevens. On lung endothelial cell heterogeneity. *Microvascular research*, 68(1):1–12, 2004.

- [69] A Gerisch and MAJ Chaplain. Mathematical modelling of cancer cell invasion of tissue: local and non-local models and the effect of adhesion. *Journal of Theoretical Biology*, 250(4):684–704, 2008.
- [70] VL Ginzburg and LD Landau. *Journal of Experimental and Theoretical Physics (USSR)*, 1064, 1950.
- [71] Hector Gomez and Kristoffer G van der Zee. Computational phase-field modeling. *Encyclopedia of Computational Mechanics Second Edition*, pages 1–35, 2018.
- [72] François Graner and James A Glazier. Simulation of biological cell sorting using a two-dimensional extended potts model. *Physical review letters*, 69(13):2013, 1992.
- [73] HP Greenspan. Models for the growth of a solid tumor by diffusion. *Stud. Appl. Math*, 51(4):317–340, 1972.
- [74] HP Greenspan. On the growth and stability of cell cultures and solid tumors. *Journal of theoretical biology*, 56(1):229–242, 1976.
- [75] Thomas Gridley. Notch signaling in the vasculature. In *Current topics in developmental biology*, volume 92, pages 277–309. Elsevier, 2010.
- [76] Karlfried Groebe and Wolfgang Mueller-Klieser. On the relation between size of necrosis and diameter of tumor spheroids. *International Journal of Radiation Oncology, Biology, Physics*, 34(2):395–401, 1996.
- [77] J Grote. Tissue respiration. In *Human physiology*, pages 598–612. Springer, 1989.

- [78] Morton E Gurtin, Debra Polignone, and Jorge Vinals. Two-phase binary fluids and immiscible fluids described by an order parameter. *Mathematical Models and Methods in Applied Sciences*, 6(06):815–831, 1996.
- [79] Philip Hahnfeldt, Dipak Panigrahy, Judah Folkman, and Lynn Hlatky. Tumor development under angiogenic signaling. *Cancer research*, 59(19):4770–4775, 1999.
- [80] Douglas Hanahan and Robert A Weinberg. The hallmarks of cancer. *Cell*, 100(1):57–70, 2000.
- [81] Douglas Hanahan and Robert A Weinberg. Hallmarks of cancer: the next generation. *Cell*, 144(5):646–674, 2011.
- [82] Heather A Harrington, M Maier, L Naidoo, Nathaniel Whitaker, and Panayotis G Kevrekidis. A hybrid model for tumor-induced angiogenesis in the cornea in the presence of inhibitors. *Mathematical and computer modelling*, 46(3):513–524, 2007.
- [83] Andrea Hawkins-Daarud, Kristoffer G van der Zee, and J Tinsley Oden. Numerical simulation of a thermodynamically consistent four-species tumor growth model. *International journal for numerical methods in biomedical engineering*, 28(1):3–24, 2012.
- [84] Mats Hellström, Li-Kun Phng, Jennifer J Hofmann, Elisabet Wallgard, Leigh Coultas, Per Lindblom, Jackelyn Alva, Ann-Katrin Nilsson, Linda Karlsson, Nicholas Gaiano, et al. Dll4 signalling through notch1 regulates formation of tip cells during angiogenesis. *Nature*, 445(7129):776, 2007.

- [85] Monica Hollstein, David Sidransky, Bert Vogelstein, Curtis C Harris, et al. p53 mutations in human cancers. *Science*, 253(5015):49–53, 1991.
- [86] Trachette L Jackson and Helen M Byrne. A mechanical model of tumor encapsulation and transcapsular spread. *Mathematical biosciences*, 180(1):307–328, 2002.
- [87] Rakesh K Jain. Delivery of molecular and cellular medicine to solid tumors. *Advanced drug delivery reviews*, 64:353–365, 2012.
- [88] RK Jain and J Wei. Dynamics of drug transport in solid tumors-distributed parameter model. *Journal of Bioengineering*, 1(4):313–329, 1977.
- [89] Stephen E Jones. Metastatic breast cancer: the treatment challenge. *Clinical breast cancer*, 8(3):224–233, 2008.
- [90] Melissa R Junttila and Gerard I Evan. p53- a jack of all trades but master of none. *Nature Reviews Cancer*, 9:821, 2009.
- [91] Raghu Kalluri and Michael Zeisberg. Fibroblasts in cancer. *Nature Reviews Cancer*, 6(5):392–401, 2006.
- [92] Johannes Kepler. *On the Six-Cornered Snowflake*. Gottfried Tampach, 1611.
- [93] Alfred G Knudson. Mutation and cancer: statistical study of retinoblastoma. *Proceedings of the National Academy of Sciences*, 68(4):820–823, 1971.

- [94] Ryo Kobayashi. Modeling and numerical simulations of dendritic crystal growth. *Physica D: Nonlinear Phenomena*, 63(3-4):410–423, 1993.
- [95] JS Langer. Models of pattern formation in first-order phase transitions. *Directions in Condensed Matter Physics: Memorial Volume in Honor of Shang-Keng Ma*, pages 165–186, 1986.
- [96] JS Langer and RF Sekerka. Theory of departure from local equilibrium at the interface of a two-phase diffusion couple. *Acta Metallurgica*, 23(10):1225–1237, 1975.
- [97] Grace Ledet and Tarun K Mandal. Nanomedicine: emerging therapeutics for the 21st century. *US pharm*, 37(3):7–11, 2012.
- [98] Howard A Levine, Brian D Sleeman, and Marit Nilsen-Hamilton. A mathematical model for the roles of pericytes and macrophages in the initiation of angiogenesis. i. the role of protease inhibitors in preventing angiogenesis. *Mathematical biosciences*, 168(1):77–115, 2000.
- [99] Howard A Levine, Serdal Pamuk, Brian D Sleeman, and Marit Nilsen-Hamilton. Mathematical modeling of capillary formation and development in tumor angiogenesis: penetration into the stroma. *Bulletin of mathematical biology*, 63(5):801–863, 2001.
- [100] SR Lubkin and T Jackson. Multiphase mechanics of capsule formation in tumors. *Transactions-American Society of Mechanical Engineers Journal of Biomechanical Engineering*, 124(2):237–243, 2002.
- [101] Carolina Mailhos, Ute Modlich, Julian Lewis, Adrian Harris, Roy Bicknell, and David Ish-Horowicz. Delta4, an endothelial specific

- notch ligand expressed at sites of physiological and tumor angiogenesis. *Differentiation*, 69(2-3):135–144, 2001.
- [102] Ahmad Makki. On the viscous allen-cahn and cahn-hilliard systems with willmore regularization. *Applications of Mathematics*, 61(6): 685–725, 2016.
- [103] DLS McElwain and GJ Pettet. Cell migration in multicell spheroids: swimming against the tide. *Bulletin of Mathematical Biology*, 55(3): 655–674, 1993.
- [104] Hiroshi Momiji and Nicholas AM Monk. Oscillatory notch-pathway activity in a delay model of neuronal differentiation. *Physical Review E*, 80(2):021930, 2009.
- [105] Nicholas AM Monk. Restricted-range gradients and travelling fronts in a model of juxtacrine cell relay. *Bulletin of mathematical biology*, 60 (5):901–918, 1998.
- [106] VR Muthukkaruppan, L Kubai, and R Auerbach. Tumor-induced neovascularization in the mouse eye. *Journal of the National Cancer Institute*, 69(3):699–708, 1982.
- [107] JA Nagy, SH Chang, AM Dvorak, and HF Dvorak. Why are tumour blood vessels abnormal and why is it important to know? *British journal of cancer*, 100(6):865, 2009.
- [108] John Nemunaitis, Gary Clayman, Sanjiv S Agarwala, William Hrushesky, James R Wells, Charles Moore, John Hamm, George Yoo, Jose Baselga, Barbara A Murphy, et al. Biomarkers predict p53 gene therapy efficacy in recurrent squamous cell carcinoma of the head and neck. *Clinical cancer research*, 15(24):7719–7725, 2009.

- [109] Paolo A Netti, Laurence T Baxter, Yves Boucher, Richard Skalak, and Rakesh K Jain. Time-dependent behavior of interstitial fluid pressure in solid tumors: implications for drug delivery. *Cancer Research*, 55(22):5451–5458, 1995.
- [110] Kerby C Oberg, Ann Mangelsdorf Soderquist, and Graham Carpenter. Accumulation of epidermal growth factor receptors in retinoic acid-treated fetal rat lung cells is due to enhanced receptor synthesis. *Molecular Endocrinology*, 2(10):959–965, 1988.
- [111] Reuben D O’Dea and John R King. Multiscale analysis of pattern formation via intercellular signalling. *Mathematical biosciences*, 231(2):172–185, 2011.
- [112] Sebastian Oltean and DO Bates. Hallmarks of alternative splicing in cancer. *Oncogene*, 33(46):5311–5318, 2014.
- [113] ME Orme and MAJ Chaplain. A mathematical model of the first steps of tumour-related angiogenesis: capillary sprout formation and secondary branching. *Mathematical Medicine and Biology*, 13(2):73–98, 1996.
- [114] ME Orme and Mark AJ Chaplain. Two-dimensional models of tumour angiogenesis and anti-angiogenesis strategies. *Mathematical Medicine and Biology*, 14(3):189–205, 1997.
- [115] Fermin Otero, Sergio Oller, and Xavier Martinez. Multiscale computational homogenization: review and proposal of a new enhanced-first-order method. *Archives of Computational Methods in Engineering*, 25(2):479–505, 2018.

- [116] Hans G Othmer and LE Scriven. Instability and dynamic pattern in cellular networks. *Journal of theoretical biology*, 32(3):507–537, 1971.
- [117] Markus R Owen and Jonathan A Sherratt. Mathematical modelling of juxtacrine cell signalling. *Mathematical biosciences*, 153(2):125–150, 1998.
- [118] Markus R Owen, Jonathan A Sherratt, and Simon R Myers. How far can a juxtacrine signal travel? *Proceedings of the Royal Society of London B: Biological Sciences*, 266(1419):579–585, 1999.
- [119] Markus R. Owen, Tomás Alarcón, Philip K. Maini, and Helen M. Byrne. Angiogenesis and vascular remodelling in normal and cancerous tissues. *Journal of Mathematical Biology*, 58(4):689, 2008. ISSN 1432-1416.
- [120] Atanasio Pandiella and Joan Massague. Cleavage of the membrane precursor for transforming growth factor alpha is a regulated process. *Proceedings of the National Academy of Sciences*, 88(5):1726–1730, 1991.
- [121] William B Pratt, William D Ensminger, Raymond W Ruddon, and Jonathan Maybaum. *The anticancer drugs*. Oxford University Press, USA, 1994.
- [122] Vito Quaranta, Katarzyna A Rejniak, Philip Gerlee, and Alexander RA Anderson. Invasion emerges from cancer cell adaptation to competitive microenvironments: quantitative predictions from multiscale mathematical models. In *Seminars in Cancer Biology*, volume 18, pages 338–348. Elsevier, 2008.

- [123] Amina A Qutub, Feilim Mac Gabhann, Emmanouil D Karagiannis, Prakash Vempati, and Aleksander S Popel. Multiscale models of angiogenesis. *IEEE Engineering in Medicine and Biology Magazine*, 28(2), 2009.
- [124] Prathibha Ranganathan, Kelly L Weaver, and Anthony J Capobianco. Notch signalling in solid tumours: a little bit of everything but not all the time. *Nature Reviews Cancer*, 11(5):338–351, 2011.
- [125] Andreas Rätz and Axel Voigt. Pde’s on surfaces—a diffuse interface approach. *Communications in Mathematical Sciences*, 4(3):575–590, 2006.
- [126] Tiina Roose, S Jonathan Chapman, and Philip K Maini. Mathematical models of avascular tumor growth. *Siam Review*, 49(2):179–208, 2007.
- [127] Mahdi Sadeghi, Milad Enferadi, Alireza Shirazi, et al. External and internal radiation therapy: past and future directions. *Journal of cancer research and therapeutics*, 6(3):239, 2010.
- [128] Nico Scheer, Anne Groth, Stefan Hans, and José A Campos-Ortega. An instructive function for notch in promoting gliogenesis in the zebrafish retina. *Development*, 128(7):1099–1107, 2001.
- [129] Richard C Schugart, Avner Friedman, Rui Zhao, and Chandan K Sen. Wound angiogenesis as a function of tissue oxygen tension: a mathematical model. *Proceedings of the National Academy of Sciences*, 105(7):2628–2633, 2008.
- [130] Oren Shaya, Udi Binshtok, Micha Hersch, Dmitri Rivkin, Sheila Weinreb, Liat Amir-Zilberstein, Bassma Khamaisi, Olya Oppenheim,

- Ravi A Desai, Richard J Goodyear, et al. Cell-cell contact area affects notch signaling and notch-dependent patterning. *Developmental cell*, 40(5):505–511, 2017.
- [131] Jonathan A Sherratt, Stephen A Gourley, Nicola J Armstrong, and Kevin J Painter. Boundedness of solutions of a non-local reaction–diffusion model for adhesion in cell aggregation and cancer invasion. *European Journal of Applied Mathematics*, 20(1):123–144, 2009.
- [132] Sabrina L Spencer, Ryan A Gerety, Kenneth J Pienta, and Stephanie Forrest. Modeling somatic evolution in tumorigenesis. *PLoS computational biology*, 2(8), 2006.
- [133] J Stefan. On the theory of ice formation, with particular regard to ice formation in the polar sea. *Sitz. Ber. Kais. Akad. Wiss. Wien*, 98: 965–983, 1890.
- [134] Cynthia L Stokes and Douglas A Lauffenburger. Analysis of the roles of microvessel endothelial cell random motility and chemotaxis in angiogenesis. *Journal of theoretical biology*, 152(3):377–403, 1991.
- [135] Cynthia L Stokes, Douglas A Lauffenburger, and Stuart K Williams. Migration of individual microvessel endothelial cells: stochastic model and parameter measurement. *Journal of Cell Science*, 99(2):419–430, 1991.
- [136] A Szabó and A Czirók. The role of cell-cell adhesion in the formation of multicellular sprouts. *Mathematical modelling of natural phenomena*, 5(1):106–122, 2010.

- [137] Naoko Takebe, Dat Nguyen, and Sherry X Yang. Targeting notch signaling pathway in cancer: clinical development advances and challenges. *Pharmacology & therapeutics*, 141(2):140–149, 2014.
- [138] RH Thomlinson and LH Gray. The histological structure of some human lung cancers and the possible implications for radiotherapy. *British journal of cancer*, 9(4):539, 1955.
- [139] Rui DM Travasso, Eugenia Corvera Poiré, Mario Castro, Juan Carlos Rodriguez-Manzanque, and A Hernández-Machado. Tumor angiogenesis and vascular patterning: a mathematical model. *PloS one*, 6(5), 2011.
- [140] A. Turing. The Chemical Basis of Morphogenesis. *Philosophical Transactions of the Royal Society of London. Series B, Biological Sciences*, 237:37–72, 1952.
- [141] Naveen S Vasudev and Andrew R Reynolds. Anti-angiogenic therapy for cancer: current progress, unresolved questions and future directions. *Angiogenesis*, 17(3):471–494, 2014.
- [142] Siren R Veflingstad, Erik Plahte, and Nicholas AM Monk. Effect of time delay on pattern formation: Competition between homogenisation and patterning. *Physica D: Nonlinear Phenomena*, 207(3-4):254–271, 2005.
- [143] Guillermo Vilanova. *Mathematical modeling and numerical simulation of tumor angiogenesis*. PhD thesis, Universidade da Coruna, 2015.
- [144] Guillermo Vilanova, Ignasi Colominas, and Hector Gomez. Coupling of discrete random walks and continuous modeling for

- three-dimensional tumor-induced angiogenesis. *Computational Mechanics*, 53(3):449–464, 2014.
- [145] Guillermo Vilanova, Ignasi Colominas, and Hector Gomez. Computational modeling of tumor-induced angiogenesis. *Archives of Computational Methods in Engineering*, pages 1–32, 2017. ISSN 1886-1784.
- [146] Charles L Vogel, Melody A Cobleigh, Debu Tripathy, John C Gutheil, Lyndsay N Harris, Louis Fehrenbacher, Dennis J Slamon, Maureen Murphy, William F Novotny, Michael Burchmore, et al. Efficacy and safety of trastuzumab as a single agent in first-line treatment of her2-overexpressing metastatic breast cancer. *Journal of Clinical Oncology*, 20(3):719–726, 2002.
- [147] Michael M Wang. Notch signaling and notch signaling modifiers. *The international journal of biochemistry & cell biology*, 43(11):1550–1562, 2011.
- [148] Christopher M Waters, Kerby C Oberg, Graham Carpenter, and Knowles A Overholser. Rate constants for binding, dissociation, and internalization of egf: Effect of receptor occupancy and ligand concentration. *Biochemistry*, 29(14):3563–3569, 1990.
- [149] Anne Waugh and Allison Grant. *Ross & Wilson Anatomy and physiology in health and illness*. Elsevier Health Sciences, 2006.
- [150] HJ Wearing, MR Owen, and JA Sherratt. Mathematical modelling of juxtacrine patterning. *Bulletin of Mathematical Biology*, 62(2): 293–320, 2000.

- [151] Steven D. Webb and Markus R. Owen. Oscillations and patterns in spatially discrete models for developmental intercellular signalling. *Journal of Mathematical Biology*, 48(4):444–476, 2004. ISSN 1432-1416.
- [152] Steven D Webb and Markus R Owen. Intra-membrane ligand diffusion and cell shape modulate juxtacrine patterning. *Journal of theoretical biology*, 230(1):99–117, 2004.
- [153] TE Wheldon and J Kirk. Mathematical derivation of optimal treatment schedules for the radiotherapy of human tumours. fractionated irradiation of exponentially growing tumours. *The British journal of radiology*, 49(581):441–449, 1976.
- [154] TE Wheldon, J Kirk, and JS Orr. Optimal radiotherapy of tumour cells following exponential-quadratic survival curves and exponential repopulation kinetics. *The British journal of radiology*, 50(597):681–682, 1977.
- [155] Cassin Kimmel Williams, Ji-Liang Li, Matilde Murga, Adrian L Harris, and Giovanna Tosato. Up-regulation of the notch ligand delta-like 4 inhibits vegf-induced endothelial cell function. *Blood*, 107(3):931–939, 2006.
- [156] IARC World Health Organization. *IARC monographs on the evaluation of carcinogenic risks to humans, Volume 55: Solar and Ultraviolet Radiation*, volume 55. World Health Organization, 1992.
- [157] IARC World Health Organization. *IARC monographs on the evaluation of carcinogenic risks to humans, Volume 83: Tobacco*

*Smoke and Involuntary Smoking*, volume 83. World Health Organization, 2004.

- [158] Jie Wu, Quan Long, Shixiong Xu, Anwar R Padhani, and Yuping Jiang. Simulation of 3d solid tumour angiogenesis including arteriole, capillary and venule. *Angiogenesis*, 5(4):1–23, 2008.
- [159] Jiangping Xu, Guillermo Vilanova, and Hector Gomez. A mathematical model coupling tumor growth and angiogenesis. *PloS one*, 11(2), 2016.
- [160] Xun Yuan, Hua Wu, Hanxiao Xu, Huihua Xiong, Qian Chu, Shiyong Yu, Gen Sheng Wu, and Kongming Wu. Notch signaling: an emerging therapeutic target for cancer treatment. *Cancer letters*, 369(1):20–27, 2015.
- [161] Iratxe Zuazo-Gaztelu and Oriol Casanovas. Unraveling the role of angiogenesis in cancer ecosystems. *Frontiers in oncology*, 8:248, 2018.